

Copyright

by

Shobha Sundar Ram

2009

The Dissertation Committee for Shobha Sundar Ram Certifies that this is the approved version of the following dissertation:

Radar Simulation of Human Activities in Non Line-of-Sight Environments

Committee:

Hao Ling, Supervisor

Dean Neikirk

J. K. Aggarwal

Edward Powers

Okan Arıkan

**Radar Simulation of Human Activities in Non Line-of-Sight
Environments**

by

Shobha Sundar Ram, B.E., M.S

Dissertation

Presented to the Faculty of the Graduate School of

The University of Texas at Austin

in Partial Fulfillment

of the Requirements

for the Degree of

Doctor of Philosophy

The University of Texas at Austin

May 2009

To my wonderful family.

Acknowledgements

It gives me great pleasure to thank all those who have helped me during the course of my graduate studies. First, I would like to express my deepest gratitude to my supervisor, Dr. Hao Ling. His expert guidance, immense enthusiasm for research and constant encouragement over the last five years have been invaluable. I am most grateful to Dr. J. K. Aggarwal, Dr. Okan Arikan, Dr. Dean Neikirk and Dr. Edward Powers for serving on my dissertation committee and offering valuable technical insights and suggestions that enhanced my understanding of many subjects. I most sincerely thank Dr. Arikan, Sony Computer Entertainment America, CMU Graphics Lab Motion Capture Database and ACCAD Motion Capture Lab for the computer animation data of human motions. I also thank Dr. Dana Ballard and Rahul Iyer from the University of Texas Virtual Reality Lab of the Dept. of Computer Science for enabling me to collect motion captured data. My appreciation extends to Dr. Adrian Lin, Dr. Youngwook Kim, Yang Li and Craig Christianson for their research contributions that enabled this work.

I gratefully acknowledge the Dept. of Electrical and Computer Engineering and the Dept of General Engineering for giving me opportunities to serve as a teaching assistant. Further, I would like to thank the Office of Graduate Studies for their financial support through the University Continuing Fellowship program.

Finally, I would like to thank my family and friends to whom I am most indebted for their unconditional love and support.

SHOBHA SUNDAR RAM

The University of Texas at Austin

May 2009

Radar Simulation of Human Activities in Non Line-of-Sight Environments

Publication No. _____

Shobha Sundar Ram, Ph.D.

The University of Texas at Austin, 2009

Supervisor: Hao Ling

The capability to detect, track and monitor human activities behind building walls and other non-line-of-sight environments is an important component of security and surveillance operations. Over the years, both ultrawideband and Doppler based radar techniques have been researched and developed for tracking humans behind walls. In particular, Doppler radars capture some interesting features of the human radar returns called microDopplers that arise from the dynamic movements of the different body parts. All the current research efforts have focused on building hardware sensors with very specific capabilities. This dissertation focuses on developing a physics based Doppler radar simulator to generate the dynamic signatures of complex human motions in non-line-of-sight environments. The simulation model incorporates dynamic human motion, electromagnetic scattering mechanisms, channel propagation effects and radar sensor parameters. Detailed, feature-by-feature analyses of the resulting radar signatures are carried out to enhance our fundamental understanding of human sensing using radar.

First, a methodology for simulating the radar returns from complex human motions in free space is presented. For this purpose, computer animation data from motion capture technologies are exploited to describe the human movements. Next, a fast, simple, primitive-based electromagnetic model is used to simulate the human body. The microDopplers of several human motions such as walking, running, crawling and jumping are generated by integrating the animation models of humans with the electromagnetic model of the human body.

Next, a methodology for generating the microDoppler radar signatures of humans moving behind walls is presented. This involves combining wall propagation functions derived from the finite-difference time-domain (FDTD) simulation with the free space radar simulations of humans. The resulting hybrid simulator of the human and wall is used to investigate the effects of both homogeneous and inhomogeneous walls on human microDopplers. The results are further corroborated by basic point-scatterer analysis of different wall effects. The wall studies are followed by an analysis of the effects of flat grounds on human radar signatures. The ground effect is modeled using the method of images and a ground reflection coefficient.

A suitable Doppler radar testbed is developed in the laboratory for simulation validation. Measured data of different human activities are collected in both line-of-sight and through-wall environments and the resulting microDoppler signatures are compared with the simulation results. The human microDopplers are best observed in the joint time-frequency space. Hence, suitable joint time-frequency transforms are investigated for improving the display and the readability of both simulated and measured spectrograms.

Finally, two new Doppler radar paradigms are considered. First, a scenario is considered where multiple, spatially distributed Doppler radars are used to measure the microDopplers of a moving human from different viewing angles. The possibility of

using these microDoppler data for estimating the positions of different point scatterers on the human body is investigated. Second, a scenario is considered where multiple Doppler radars are collocated in a two-dimensional (2-D) array configuration. The possibility of generating frontal images of human movements using joint Doppler and 2-D spatial beamforming is considered. The performance of this concept is compared with that of conventional 2-D array processing without Doppler processing.

Table of Contents

List of Figures	xiii
1. Introduction.....	1
1.1. Radar Systems for Sensing Humans Behind Walls	2
1.2. Motivation.....	6
1.3. Scientific Objective and Approach.....	7
1.4. Organization.....	10
2. Doppler Radar Testbed	13
2.1. Introduction.....	13
2.2. Radar Theory and Simulation	14
2.3. Monte Carlo Simulation.....	16
2.4. DOA Estimation.....	18
2.5. Measurement Results	22
2.6. Conclusion	29
3. Joint Time-Frequency Transform	30
3.1. Introduction.....	30
3.2. Derivation of the Reassigned Joint Time-Frequency Transform.....	31
3.3. MicroDoppler from Human Gait:	33
3.4. Conclusion	40
RADAR SIMULATION MODEL	41
4. Radar Simulation of Humans.....	41
4.1. Introduction.....	41
4.2. Methodology	43
4.3. Verification of Simulation Methodology With Joint Collection of Mocap and Radar Measurement Data.....	48
4.4. Simulation Results	51
4.5. MicroDoppler Signatures of Anomalous Human Gait	66
4.6. Conclusion	72

5. Simulation of Wall Effects on Human Signatures	73
5.1. Introduction.....	73
5.2. FDTD Simulations of Different Walls.....	74
5.3. Hybrid Model of Human and Wall Simulations.....	79
5.4. MicroDopplers From a Human Walking Behind a Wall.....	80
5.5. Quantitative Analysis of Wall Effects	85
5.6. Further Investigations	91
5.7. High Range-Resolution Profile of a Human Walking Behind a Wall.....	95
5.8. Conclusion	98
6. Simulation of Floor Effects on Human Signatures	100
6.1. Introduction.....	100
6.2. Methodology	101
6.3. Results.....	103
6.4. Conclusion	111
EXPLOITATION OF THE RADAR SIMULATION MODEL	112
7: Distributed Doppler Sensors	112
7.1. Introduction.....	112
7.2. Methodology	113
7.3. Results.....	117
7.4. Conclusion	120
8: Doppler Sensor Array	122
8.1. Introduction.....	122
8.2. Methodology	123
8.3. Results.....	127
8.4. Conclusion	137
9. Conclusions.....	138
9.1. Contributions.....	138
9.2. Future Work	140
References.....	143

Vita 149

List of Figures

Fig.2.1. Joint Doppler and spatial beamforming radar architecture	15
Fig.2.2. (a) Detection of targets in the Doppler versus DOA plot, (b) Monte Carlo simulation results for probability of successfully resolving multiple targets with an antenna array	17
Fig.2.3. Simulation results when ratio of strength of targets is 20dB for (a) Spatial beamforming, (b) CLEAN and (c) RELAX techniques.	21
Fig.2.4. Photo of 2.4 GHz microstrip receiving array	22
Fig.2.5. Three loudspeaker targets in indoor LOS resolved in the Doppler–DOA space, in decibel scale: (a) Experimental set up. (b) Beamforming result, (c) CLEAN result and (d) RELAX result.	23
Fig.2.6. Three human subjects in indoor LOS resolved in the Doppler–DOA space: (a) Measurement setup, (b) beamforming result, (c) CLEAN result and (d) RELAX result.	25
Fig.2.7. Two human subjects in a through-wall scenario resolved in the Doppler space: (a) Measurement setup and (b) CLEAN result.	26
Fig.2.8. Two human subjects in a through-wall scenario resolved in the DOA space: (a) Measurement set up, (b) CLEAN result for a single time instant, (c) Time integrated CLEAN results.....	28
Fig.2.9. Two loudspeaker targets in a through-wall scenario resolved in Doppler in decibel scale: (a) Experimental set up and (b) CLEAN result.....	29
Fig.3.1. Spectrogram of a signal comprising a click, a ramp and white Gaussian noise. (a) STFT (b) Reassigned transform.	33
Fig.3.2(a) Simulation model of human walking at 1.4 m/s towards a Doppler radar.....	35
Fig.3.3. Spectrogram of human gait obtained by processing measured data from a 2.4GHz Doppler radar: (c) STFT. (d) Reassigned transform.	36
Fig.3.4. (a) Case 1: walking human subject, (b) Reassigned spectrogram of case 1	40
Fig.4.1. Animation model of walking human.	44
Fig.4.2. (a) Generation of infrared motion capture data and Doppler radar data of a moving human object. Doppler spectrogram of human motions at 2.4 GHz generated from (b) motion capture data and (c) measurement data.	51
Fig.4.3.(a) Animation model of human walking motion from Sony Computer Entertainment America. Doppler spectrogram of human walking motion at 2.4 GHz generated from (b) simulation data, (c) measurement data.....	55
Fig.4.4.(a) Animation model of human running motion from Sony Computer Entertainment America. Doppler spectrogram of human running motion at 2.4 GHz generated from (b) simulation data, (c) measurement data.....	56
Fig.4.5.(a) Animation model of human crawling motion from CMU Graphics Lab Motion Capture Database. Doppler spectrogram of human crawling motion at 2.4 GHz generated from (b) simulation data, (c) measurement data.	57

Fig.4.6.(a) Animation model of human walk-jump-walk motion from ACCAD Motion Capture Lab. Doppler spectrogram of human walk-jump-walk motion at 2.4GHz generated from (b) simulation data, c) measurement data.....	58
Fig.4.7. (a) Animation model of human walking motion across the radar's field of view. (b) Doppler spectrogram of walking motion at 2.4GHz carrier frequency.....	59
Fig.4.8. Simulated Doppler spectrogram of walking motion at 12GHz	60
Fig.4.9.Simulated Doppler signatures of human motions over a one-minute duration. ...	61
Fig.4.10.(a) Computer animated galloping horse. Doppler spectrogram at 2.4GHz of the motion of: (b) galloping horse, (c) horse's forelegs, (d) horse's rear legs, (e) horse's torso and head and (f) horse's tail.....	63
Fig.4.11. (a) Computer animated walking dog. Doppler spectrogram at 8 GHz of the motion of: (b) walking dog, (c) dog's forelegs, (d) dog's rear legs, (e) dog's tail.	65
Fig.4.12.Doppler spectrogram of a dog motion transition from.....	66
Fig.4.13. Simulated spectrogram at 12GHz of (a) regular human gait, $\chi_r(t,f)$. (b) human walking without swinging the arms, $\chi_{a1}(t,f)$, (c) human walking while carrying a 1.1m metal stick in the left arm, $\chi_{a2}(t,f)$. (d) Computer animation data of the human carrying the stick used to simulate Fig.4.13(c). (e) $\chi_r(t,f) - \chi_{a1}(t,f)$ shows the missing microDoppler features in Fig.4.13(b) due to human arm motions. (f) $\chi_{a2}(t,f) - \chi_r(t,f)$ shows the additional microDoppler feature in Fig.4.13(c) due to the metal stick.....	68
Fig.4.14. Measured spectrogram at 2.4GHz of (a) regular human walking gait, $\chi_r(t,f)$, (b) human walking while carrying a heavy tool box in the left hand, $\chi_{a1}(t,f)$, (c) human walking with a long metal pole in the left hand, $\chi_{a2}(t,f)$. (d) $\chi_r(t,f) - \chi_{a1}(t,f)$ shows the missing microDoppler features in Fig.4.13(b) due to motions of the left arm and leg. (e) $\chi_{a2}(t,f) - \chi_r(t,f)$ shows the additional microDoppler feature in Fig.4.13 (c) from the metal pole. (f) $\chi_r(t,f) - \chi_{a2}(t,f)$ shows the missing microDoppler features in Fig.4.13(c) due possibly to shadowing by the metal pole.	71
Fig.5.1. Models of 3 different types of walls for FDTD simulations: (a) homogeneous wall, (b) reinforced concrete wall and (c) cinderblock wall.	75
Fig.5.2. Results from FDTD simulations: Magnitude response at 2.4GHz for (a) free space, (b) homogeneous concrete wall, (c) reinforced concrete wall and (d) cinderblock wall.....	76
Fig.5.3. Results from FDTD simulations: Phase response at 2.4GHz for (a) free space, (b) homogeneous concrete wall, (c) reinforced concrete wall and (d) cinderblock wall.	77
Fig.5.4. Results of simulations of human and wall: Reassigned Doppler spectrogram of walking human at 2.4GHz for (a) free space, (b) homogeneous wall, (c) reinforced concrete wall and (d) cinderblock wall.....	81
Fig.5.5. Doppler spectrogram generated from measurement data collected using the Doppler radar testbed at 2.4GHz for (a) indoor line of sight, (b) through exterior 15" brick wall and (c) 12" cinderblock wall.....	85
Fig.5.6. Derivation of effect of wall refraction on the Doppler of a point scatterer (a) Simulation set up (b) $\cos \theta$	87

Fig.5.7. Doppler map for radial path motion of point scatterer at 2.4GHz for (a) free space, (b) homogeneous wall, (c) reinforced concrete wall and (d) cinderblock wall.	89
Fig.5.8. Doppler map for tangential path motion of point scatterer at 2.4GHz for (e) free space, (f) homogeneous wall, (g) reinforced concrete wall and (h) cinderblock wall.....	90
Fig.5.9. Results of simulations of human and wall: Doppler spectrogram of walking human (<i>human is oblique wrt radar</i>) at 2.4GHz for (a) free space and (b) homogeneous concrete wall, (c) reinforced concrete wall and (d) cinderblock wall.....	92
Fig.5.10. Results of simulations of human between 2 cinderblock walls at 2.4GHz: (a) magnitude response and (b) phase response. Doppler spectrogram of human between two (c) homogeneous walls, (d) reinforced concrete walls and (e) cinderblock walls.....	95
Fig.5.11. Results of simulations of human and wall: Range profile of walking human obtained from UWB waveform of 2GHz (1.4 – 3.4 GHz) for (a) free space, (b) homogeneous wall, (c) reinforced concrete wall and (d) cinderblock wall.....	96
Fig.6.1. Simulation methodology.....	103
Fig.6.2. High range-resolution signature of human walking towards a radar 1m high, (Inset figures are of the right foot), (a) without floor, (b) smooth floor with $\epsilon_r=5$ and (c) PEC floor.	104
Fig.6.3. Doppler spectrogram of human walking towards a radar 1m high at 2.4 GHz, (Inset figures are of the right foot), (a) without floor, (b) smooth floor with $\epsilon_r=5$ and (c) PEC floor.	105
Fig.6.4. High range-resolution signature of right human foot when human is walking towards a radar 20m high, (a) without floor, (b) smooth floor with $\epsilon_r=5$ and (c) PEC floor.	107
Fig.6.5. Doppler spectrogram of right human foot when radar is 20m at 2.4GHz, (a) without floor, (b) smooth floor with $\epsilon_r=5$ and (c) PEC floor.....	108
Fig.6.6. High range-resolution signature of human crawling towards a radar 1m high, (a) without floor, (b) smooth floor with $\epsilon_r=5$ and (c) PEC floor.....	109
Fig.6.7. Doppler spectrogram of human crawling towards a radar 1m high, (a) without floor, (b) smooth floor with $\epsilon_r=5$ and (c) PEC floor.	110
Fig.7.1. Distributed Doppler sensors	114
Fig.7.2. Doppler spectrogram of walking human generated for 7.2GHz from sensor ...	115
Fig.7.3. Extracted features from the Doppler spectrogram in Fig.7.2.	115
Fig.7.4. (a) Truth values of v_x (m/s) of 5 human body parts, (b) estimated values of v_x (m/s). (c) Truth values of v_y (m/s) and (d) estimated values of v_y (m/s).	118
Fig.7.5. True and estimated positions of (a) torso, (b) left arm, (c) right arm, (d) left leg and (e) right leg.....	120
Fig.8.1. Methodology.....	125

Fig.8.2. 5 ideal point scatterers, (a) True frontal image, Images generated from (b) 4 X 4 array processing, (c) 4 x 4 array processing and Doppler processing at $f_c = 2.4$ GHz, (d) 4 x 4 array processing and Doppler processing at $f_c = 7.5$ GHz.	130
Fig.8.3. 5 point scatterers on human body (torso, two hands and two feet), (a) True frontal image. Images generated from (b) 4 x 4 array processing, (c) 4 x 4 array processing and Doppler processing at $f_c = 7.5$ GHz, (1-D peak detection projection) (d) 4 x 4 array processing and Doppler processing at $f_c = 7.5$ GHz (3-D peak detection projection). ..	132
Fig.8.4. Complete human body (28 point scatters), (a) True frontal image. Images generated from (b) 4 X 4 array processing, (c) 10 x 10 array processing and (d) 20 x 20 array processing.	134
Fig.8.5. Complete human body (28 point scatters): Images generated from Doppler processing with $f_c = 2.4$ GHz and (a) 4 x 4 array processing, (b) 10 x 10 array processing and (c) 20 x 20 array processing.	135
Fig.8.6. Complete human body (28 point scatters): Images generated from Doppler processing with $f_c = 7.5$ GHz and (a) 4 x 4 array processing, (c) 10 x 10 array processing and (c) 20 x 20 array processing.	136

1. Introduction

Detection, tracking and monitoring human activities in non-line-of-sight environments are important aspects of law enforcement such as hostage rescue, security and surveillance operations as well as search and rescue missions. Detailed situational information such as the number of people present in an urban area, their location and the type of activities they are engaged in can be of critical importance that aid in decision making. For this purpose, different types of sensors have been researched including optical, infrared, ultrasound, X ray and radio frequency (RF) sensors [1]-[4]. Each offers some unique advantages. While optical and infrared sensors have excellent resolution which is useful for imaging targets, they cannot be used in through-wall environments since they have poor wall penetration. Also, these sensors cannot operate 24/7 and under difficult weather conditions. Ultrasound signals marginally penetrate walls and are useful for detecting motion. However, the maximum achievable range from such sensors is quite limited. X ray sensors have both wall penetration and high resolution capacities. On the other hand, the sensors are expensive and often have safety concerns. Some of the unique advantages offered by an RF sensor are the abilities of operating 24-hour, under all weather conditions and in through-wall environments. Also, inexpensive radar systems capable of detecting and locating moving humans behind walls can be developed from off-the-shelf RF components. As a result, there is an abundance of RF sensor research and development for through-wall human sensing.

1.1. RADAR SYSTEMS FOR SENSING HUMANS BEHIND WALLS

The attenuation of an electromagnetic signal through walls increases rapidly as a function of frequency [5]-[7]. Therefore, the RF technologies that are currently being researched for sensing humans behind walls typically operate anywhere between UHF and X-bands to obtain good wall penetration [8]-[29]. These sensors can be broadly grouped into two categories. The first type of sensors utilizes ultrawideband (UWB) techniques to obtain good down-range resolutions. The second category utilizes Doppler processing to sense moving targets. Some of the UWB and Doppler based sensors that have been developed for sensing humans behind walls are described below.

First, we consider through-wall radar using UWB techniques. It is well known that waveforms with wide bandwidth, β , are useful for achieving a high range-resolution Δr , as described by the equation:

$$\Delta r = \frac{c}{2\beta} \quad (1.1)$$

where c is the speed of light. Different types of waveforms have been used to achieve wide bandwidth. For instance, Time Domain Corporation's Radar Vision and Soldier Vision radars [8]-[10] transmit extremely short duration pulses and compute the range of a target based on the time delay of the reflected echo from the target. Further, the pulses are pseudo-randomly coded so that the transmitted signal resembles noise to ensure operational covertness. Other waveforms such as stepped frequency [11]-[13] and linear frequency modulated continuous wave (FMCW) [14] have also been researched for achieving high bandwidth and correspondingly high down-range resolution.

Theoretically, the cross-range resolution is determined by the product of the range and the beamwidth θ_B (in radians) of the radar which is inversely proportional to the dimension D , of the antenna aperture:

$$\Delta x = r\theta_B \approx r \frac{\lambda_c}{D} \quad (1.3)$$

λ_c is the wavelength of the system. Therefore, systems such as Radar Vision obtain the bearing information of targets using an array of transmitter and receiver elements [8]-[10]. Alternately, large antenna apertures have also been generated synthetically. For example, Eureka Aerospace's ImpulseSAR [15],[16] combines impulse techniques with synthetic aperture to generate two-dimensional (2-D), i.e., range versus cross-range, images of a scene. The ability for generating complete three-dimensional (3-D) volumetric images of a scene have also been reported by Cambridge Consultant's Prism200 [17] and Camero's Xaver800 [18] radars. These radars combine the ranging capabilities of UWB technologies with 2-D bearing information that can be obtained from 2-D array processing. However, UWB radars do have some limitations. First, wideband systems are intrinsically susceptible to noise and very high transmit power is required. Consequently, the cost and complexity of these systems are usually quite high. Second, the operations of UWB sensors at certain frequency bands may require a license from the Federal Communications Commission (FCC). Also, building wall effects such as multipath, transmission delay, diffraction considerably distort the high range-resolution signatures of targets behind walls [30]. Hence, additional signal processing is

often required to deconvolve wall effects from the received signals. This can be quite challenging when the wall characteristics are not known.

Doppler based radar systems offer an alternate approach to UWB for tracking humans behind walls. It is well known that a Doppler shift, f_D , is introduced in the scattered signal from a moving target:

$$f_D = \frac{2f_c}{c} v_r \quad (1.3)$$

which is proportional to the carrier frequency of the signal, f_c , and the radial velocity, v_r , of the target with respect to the radar. For human movement detection and tracking, Doppler sensing is a natural choice since stationary indoor clutters can be suppressed to highlight human movements. Further, since Doppler radar architectures are quite simple, low-cost, low-power Doppler sensors can be readily implemented using off-the-shelf components. It is, however, not possible to detect and track stationary humans using the Doppler approach. Moreover, non-human movers and the radar operator are potential sources of false alarm.

An early example of a Doppler based system is the zero-dimensional (0-D) motion detector radar developed by Frazier [5]. This radar transmits a low power CW signal from a single transmitter unit. The presence of moving targets is detected by using a CW phase detector at the receiver to sense the Doppler shift in the scattered signal. Later, Grenkar and Geisheimer from Georgia Tech Research Institute (GTRI) developed a prototype of an X-band (10.525 GHz) 0-D Doppler radar called the Radar Flashlight to detect even very slight body movements such as respiratory motions of humans behind

walls [19],[20]. Both these radars were primarily intended for detecting the presence of intruders. Information such as the number of moving targets, the type and location are not available. Recently, a low-complexity CW radar concept that performs Doppler based location tracking of multiple movers was investigated by Lin at University of Texas at Austin [21],[22]. Lin's radar combines the Doppler discrimination offered by human movements with 2-D bearing information that can be collected using three antenna elements using the principles of interferometry. Further, ranging capability was achieved by the incorporation of one additional frequency tone. Thus, full 3-D tracking of multiple targets is achieved using a radar architecture with a single transmitting antenna, four receivers and three receiver array elements provided the targets have distinct Dopplers.

Another important advantage of a Doppler radar is that it is capable of capturing a unique feature of human movements called microDoppler. MicroDopplers of humans were first reported by Geisheimer from GTRI in 2000 [31]. Contrary to rigid targets commonly encountered in other radar applications, a human is a complex non-rigid body under movement. Hence the radar returns are characterized by time-varying Doppler features that are best observed as spectrograms in the joint time-frequency space [32],[33]. The Doppler spectrogram is characterized by different microDoppler tracks due to the torso return as well as those arising from the swinging arms and legs. These features were found to be quite distinct from the microDopplers of mechanical vibration, rotation and translation motions of rigid bodies [34],[35]. Since it was first reported, significant research efforts have been devoted to utilizing a moving body's microDoppler signature for recognition and classification [35]-[39]. All the classifiers that have been

developed so far have been trained by measured data collected in controlled environments. The data could be influenced by the parameters of the measurement system and environment. Hence it is not yet known whether human microDopplers are sufficiently reliable features for target recognition and classification across a broad spectrum of environments. Detailed studies are required to determine the relationships between the microDoppler features of different human motions and the sensor parameters as well as propagation channels.

1.2. MOTIVATION

Most of the research efforts in RF sensing of humans up to this point have primarily focused on developing radar hardware for very mission-specific goals. As a result of this system-specific approach, the theoretical limits of RF sensing of humans have not been identified. In order to determine these limits, it is necessary to fundamentally examine the how human movements are manifested in radar sensor data. In turn, this knowledge will enable the radar community to optimize sensor designs for different applications. It is believed that a physics-based radar simulator of the scatterings from different human motions, for diverse sensor parameters, and under various propagation environments will help address this deficiency in the knowledge base.

A complete end-to-end radar simulator of humans will allow us to perform detailed feature-by-feature analysis of human radar signatures. This will enable us to pinpoint cause-and-effect of different sensor parameters as well as propagation channel characteristics on human radar signatures. Ultimately, the simulator will enhance our

fundamental knowledge of the different phenomena inherent in the RF sensing of humans. A sophisticated simulator will serve as a key enabler for investigating the “art-of-the-possible” for human sensing in different scenarios. This in turn will minimize the cost, time and effort involved in designing radar hardware with maximum information gathering capabilities.

In the past, electromagnetic simulators that modeled conventional air and ground targets have proven to be indispensable for researching and ultimately developing sophisticated radar target recognition systems. It is hoped that a radar simulator of humans in indoor environments will enable us to generate training databases that could lead to the same outcome.

1.3. SCIENTIFIC OBJECTIVE AND APPROACH

The objectives of my dissertation are:

- (1) To develop a physics-based simulator of the scattering mechanisms associated with different human motions as a function of radar sensor parameters such as frequency, bandwidth, dwell time etc.
- (2) To incorporate commonly occurring propagation channels such as building walls and grounds into the radar simulation model of humans.
- (3) To validate the results from the simulator with measurement data collection using a Doppler radar developed in the laboratory.
- (4) To exploit the radar simulator to investigate some new radar sensor paradigms for imaging humans.

The following approach is followed to meet the objectives.

1.3.1 Radar Simulation of Humans

Previously, van Dorp simulated the radar returns of the human walking motion by using a simple electromagnetic primitive based model for the human body [33]. However, van Dorp's work was limited to the simple motion of a human walking at a constant velocity described by Thalmann [40]. The Thalmann model is a simple three-parameter model that cannot be extended to other motions. On the other hand, motion capture is a well-established technology that has been used by animation industries to provide detailed descriptions of almost any complex human motion such as crawling, running and jumping. Hence, we accomplish the first objective of the dissertation, by simulating the radar returns from humans by combining computer animation data that describe complex human motions with the primitive based electromagnetic model of the human body. Different body parts are modeled as basic primitives such as ellipsoids and spheres and the total scattering from the human is obtained from the sum of the returns from all the body parts. This technique is adopted instead of more rigorous computational electromagnetic techniques since it can be easily combined with dynamic human motion models to capture most of the essential scattering physics [41],[42].

1.3.2 Radar Simulation of Channel Propagation Effects

In order to accomplish the second objective, an approach is developed to simulate the frequency transfer function of propagation environments such as building walls and incorporate the propagation effect into the human radar simulation model. The wave

propagation through the wall is simulated using the finite-difference time-domain technique (FDTD) [43]. FDTD is chosen since it is a full-wave electromagnetic approach. It can accurately model the physics of even complex inhomogeneous walls such as cinderblock walls, which approximate techniques such as high-frequency ray tracing fail to model accurately [44]-[47].

Similarly, a simulation approach is developed using the method of images and a ground reflection coefficient to study the effect of a flat ground on the radar signatures of human motions.

1.3.3 Validation of Human Radar Signatures

The results from the radar simulation model are validated by comparing them with human radar signatures generated from measurement data collected using a Doppler radar testbed developed in the laboratory. This testbed is modified from the prototype of a radar developed earlier by Lin in 2006 [22]. Data of different human motions are collected in both line-of-sight environments and in different through-wall scenarios and compared.

Next, suitable joint time-frequency transforms are investigated for improving the display and feature-by-feature analysis of radar microDoppler signatures. In particular, two different joint time-frequency transforms are considered. The first is the traditional short-time Fourier transform (STFT) and the second is the reassigned transform [48]-[51] which has been extensively used by the acoustic community [49],[50]. They are

applied on both simulated and measured human gait data and the resulting microDoppler features are studied.

1.3.4 Exploitation of the Radar Simulation Model

Next, the radar simulation model is exploited to investigate new Doppler radar paradigms for generating visual animations of humans. Two different scenarios are considered. First, multiple Doppler radars are assumed to be spatially distributed along the perimeter of an area within which the human moves. Previous research efforts have demonstrated that it is possible to estimate the position and velocity of a moving target based on Doppler measurements by multiple spatially distributed sensors [52],[53]. The possibility of exploiting this principle to extract the time-varying position coordinates of different point scatterers on the human (such as torso, arms and legs) from the microDoppler data obtained from multiple sensors is investigated.

In the second scenario, the possibility of generating a frontal image of a human using a 2-D Doppler sensor array is examined. 3-D beamforming using joint Doppler and 2-D array processing is first implemented on the time-domain array data. Human radar returns are mapped into a 3-D Doppler-azimuth-elevation space. Next, suitable algorithms are applied to project the results from the 3-D space into the 2-D azimuth-elevation space to generate a frontal image of a human.

1.4. ORGANIZATION

The dissertation is organized in the following manner. We begin by describing some of the background materials in Chapters 2 and 3. Chapter 2 describes a multi-

element Doppler radar testbed developed for simulation validation. This radar is used to collect human measurement data in both indoor line-of-sight and through-wall scenarios. Since the radar uses a limited sized array, the beamforming results are plagued with high sidelobe levels. Hence, some algorithms for improving the performance of the limited sized array are also investigated.

Chapter 3 discusses two joint time-frequency transforms, the traditional short-time Fourier transform (STFT) and the reassigned transform [48]-[51]. A detailed description of the reassigned transform is presented. Then both the transforms are tested on both simulated and measured human gait data and their performances are compared.

The development of human signature simulation is presented in Chapters 4 to 6. Chapter 4 describes the methodology used to combine computer animation data with the primitive based electromagnetic prediction technique to generate the Doppler spectrograms of different complex human motions. The simulated radar signatures are validated with radar signatures generated from measured data. The effects of sensor frequency and viewing angle are investigated. The methodology is further extended to model radar returns from different animal motions described by computer animation data.

The methodology for hybridizing primitive based modeling of humans and FDTD simulations of walls to generate the radar signatures of humans behind walls is presented in Chapter 5. The simulation methodology enables the investigation of the effect of complex walls on human radar signatures. The simulation results are validated with measured data collected in line-of-sight and through-wall scenarios using the Doppler radar testbed. The findings are further supplemented with an analytical study of the effect

of wall refraction and multipath introduced by wall inhomogeneity on the Dopplers of a point target moving behind walls.

Chapter 6 investigates the effects of ground on the radar signatures of human motions. The simulation methodology based on the method of images is described. The simulated signatures of different human motions are presented as functions of ground reflectivity, radar elevation and type of motions.

The simulation model is used to investigate two different Doppler radar paradigms to image humans in Chapters 7 and 8. First, the concept of using multiple spatially distributed Doppler sensors for generating an image of a moving human is investigated in Chapter 7. Next, the possibility of generating frontal images of a walking human using joint Doppler and 2-D array processing is examined in Chapter 8.

A detailed conclusion and future avenues of research are presented in Chapter 9.

2. Doppler Radar Testbed

We begin this dissertation with a description of the Doppler radar testbed that will be used later for measurement data collection. This Doppler radar was previously developed by Lin for tracking humans. The first generation radar was a 2.4GHz, two-element Doppler and direction-of-arrival (DDOA) radar. In this chapter, my work upgrades this radar to a 4-element array and combines it with software beamforming to track multiple humans.

2.1. INTRODUCTION

The low-complexity continuous wave (CW) radar of two elements reported by Lin in [22] used Doppler discrimination to track multiple movers. The azimuth direction-of-arrival (DOA) of the targets is estimated using just two antenna elements spaced in the horizontal direction. More explicitly, if the time signals received at the two antenna elements are $x_1(t)$ and $x_2(t)$, then after Doppler processing the signals become $X_1(f)$ and $X_2(f)$, respectively. If the targets of interest generate different Doppler frequencies f_i due to the difference in their velocities with respect to the radar transceiver, then the DOA θ_i of target i with respect to the array boresight is derived from the phase difference of the scattered signal at the two elements as shown in:

$$\theta_i = \sin^{-1} \left[\frac{\angle X_1(f_i) - \angle X_2(f_i)}{(2\pi d / \lambda_c)} \right] \quad (2.1)$$

Here, d is the spacing between the elements. The wavelength of the radar is λ_c . This concept was also extended for two-dimensional azimuth-elevation tracking and three-

dimensional range-azimuth-elevation tracking [21]. However when the Doppler separation among the multiple targets is poor, the DOA error was found to increase significantly. To overcome this limitation, we investigate the performance improvement by using a multiple element array. Doppler processing is implemented in conjunction with spatial beamforming in software to resolve multiple targets in the Doppler and DOA space. Monte Carlo simulations are carried out to assess the performance gain of a multi-element system. To further overcome the broad beamwidth and high sidelobes in a limited size array, two different DOA estimation algorithms are implemented. They are the CLEAN algorithm [54], and the RELAX algorithm [55]. The performance of the different algorithms is studied by simulation and experimentally verified by using a 4-element receiver array. Measurements are conducted under line-of-sight and through-wall scenarios for audio loudspeakers and human targets.

2.2. RADAR THEORY AND SIMULATION

Fig.2.1 shows the basic radar architecture under consideration. A CW signal is radiated from a transmitter and a moving target introduces a Doppler shift on the scattered signal. The radar receiver consists of a multi-element antenna array, with each element connected to a separate receiver channel where the signal is amplified, downconverted and digitized before it is fed to a computer for further signal processing.

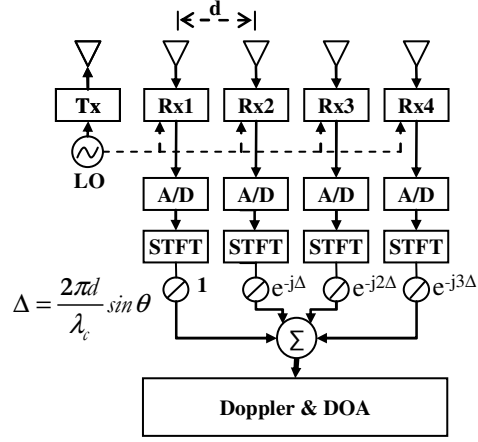


Fig.2.1. Joint Doppler and spatial beamforming radar architecture

Doppler and spatial beamforming are performed on the received signals according to equation (2.2):

$$\chi(t, f, \theta) = \frac{1}{N} \sum_{n=1}^N \int \left\{ x_n(t') h(t'-t) e^{-j2\pi f t'} dt' \right\} e^{-j(n-1) \frac{2\pi d}{\lambda_c} \sin \theta} \quad (2.2)$$

The short-time Fourier transform (STFT) is first applied to the time domain signal, $x_n(t)$, of receiver element n to capture the instantaneous Doppler, f , of the targets. $h(t)$ is the time window used in the STFT operation. Spatial beamforming is next performed by introducing a phase shift that is proportional to the sine of the beam steering angle θ from the boresight, to the signals at each of the receiver elements followed by summation of the phase shifted signals. These two steps help resolve the target returns along the Doppler and DOA dimensions for each time instant, t . Here, N is the total number of elements in the antenna array.

2.3. MONTE CARLO SIMULATION

Monte Carlo simulations are next performed to gauge the performance of the joint Doppler-beamforming algorithm towards the successful tracking of multiple targets. The following assumptions are made for the simulation. For each realization, a given number of targets are randomly placed inside a sectorial region of space bounded in range from 1 to 10m and DOA from -45° to $+45^\circ$. Each target is randomly assigned a velocity of magnitude in the range of 0 to 2.5m/s and direction in the range of 0° to 360° . This yields Doppler values in the range of -40Hz to +40Hz for an RF wavelength of 12.5cm. The ability of the radar to resolve a single target's returns is assumed to be constrained in the DOA dimension by the beamwidth of the linear array, which for an antenna aperture of size D is $50^\circ/(D/\lambda_c)$. In the Doppler dimension, the ambiguity is mainly caused by the microDoppler components from the arms and legs of the human movement. A 40Hz Doppler spread is introduced to simulate the microDoppler spread for each target. With these two assumptions, each target is resolvable up to the rectangular ambiguity region in the DOA vs. Doppler space as shown in Fig.2.2a.

For multiple targets, the chance of overlap between the targets' ambiguity regions is increased. When the ambiguity regions of any two targets overlap by more than 50%, the realization is considered to be irresolvable by the radar. This simulation is performed for 500,000 realizations and the results are tallied.

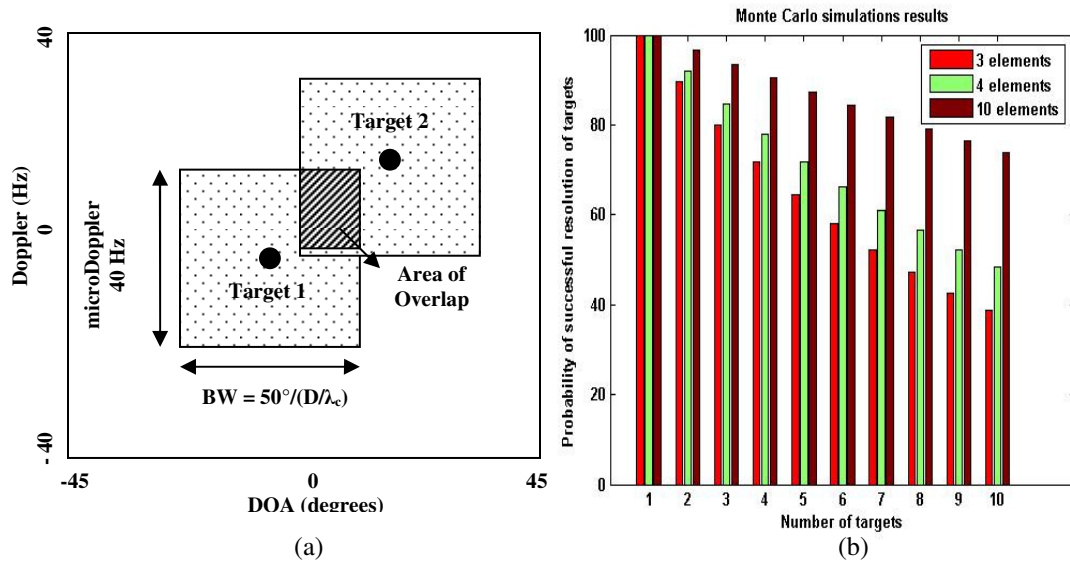


Fig.2.2. (a) Detection of targets in the Doppler versus DOA plot, (b) Monte Carlo simulation results for probability of successfully resolving multiple targets with an antenna array.

Fig.2.2b shows the probability of successfully resolving multiple targets versus the number of targets. Each color represents a different assumed number of array elements, and therefore a different size antenna aperture. As expected, as the number of targets is increased, the probability of successfully resolving the targets drops. Using more array elements improves the performance, especially in the case of a large number of targets, since a narrower beamwidth improves the DOA resolution. This is done at the expense of increased system cost and complexity. We see that with 4 elements, there is a 78% probability of successfully resolving 4 targets.

2.4. DOA ESTIMATION

If multiple targets are not well resolved in the Doppler domain, their successful DOA determination becomes quite difficult using a small size array, especially when the target strengths are very different. This is understood from the following simulation performed in a two target scenario where the targets are of the same Doppler. Hence the detection of the two targets is entirely determined by spatial beamforming. The simulation is conducted for a four-element antenna array and the ratio of the strength of the two targets is set to 20dB. The angular position of the strong target is varied from -45° to $+45^\circ$ while that of the weak target is varied from $+45^\circ$ to -45° as indicated by the dashed lines in Fig.2.3a. For each pair of simulated angular positions of the targets, the main lobe and sidelobe patterns arising from the two targets are computed by spatial beamforming. The DOA of the targets are estimated to be at the peaks of the beamformer pattern and their strengths are represented by the colored intensity as indicated in Fig.2.3a. It is observed that the DOA of the strong target is detected correctly at every possible DOA position of the targets. The weaker target however is not detected at all because it is buried beneath the sidelobes of the strong target. This result is unsatisfactory. In order to improve the tracking of weak targets in the presence of strong targets, two different algorithms are implemented, namely, CLEAN and RELAX, and their performances are evaluated using the same simulation set up.

2.4.1. Clean Algorithm

The CLEAN algorithm is a well-known technique to extract weaker features in the presence of strong features, given that the feature response function is known [54]. Here the algorithm is applied to extract the DOA of multiple targets. For each Doppler bin and at each time instant, the algorithm first identifies the strength, a_I , and DOA, θ_I , of the strongest target from the spatial beamforming pattern, χ :

$$|a_I|^2 = \max_{\theta} \left| \frac{1}{N} \sum_{n=1}^N x_n e^{-j(n-1) \frac{2\pi d}{\lambda_c} \sin \theta} \right|^2 \quad (2.3)$$

Once the DOA of the strongest target is found, its main lobe and sidelobe features are removed from the spatial beamforming pattern as follows:

$$\chi_{residual|_I} = \chi - \frac{1}{N} \sum_{n=1}^N a_I e^{-j(n-1) \frac{2\pi d}{\lambda} (\sin \theta - \sin \theta_I)} \quad (2.4)$$

Since the strongest target is removed together with its sidelobe contribution, the weaker target becomes better revealed in the residual pattern, $\chi_{residual|_I}$. The next strongest target and its DOA are then determined and removed from the residual signal. This procedure is continued in successive steps until the till the residual energy, $|\chi|_{residual|_M}^2$, falls below the noise floor. This algorithm is simulated for the two target scenario described earlier and the results are presented in Fig.2.3b. It is observed that the weak target is detected in the presence of a stronger target as long as their angular separation exceeds the beamwidth of the array. The algorithm clearly performs better than the ordinary beamforming technique towards detecting multiple targets. However there does appear to

be false targets near the strong target due to the influence of the weaker target on the strong target.

2.4.2. Relax Algorithm

It is known that the DOA estimation using CLEAN is inherently biased due to the sidelobe interference between the targets. This error can be further minimized by introducing the RELAX procedure at each CLEAN step. The RELAX algorithm is an enhanced version of CLEAN that relieves the error propagation tendencies in CLEAN [55]. It introduces a relaxation step that iteratively identifies target parameters (strength and DOA) until the energy of the residual pattern at each CLEAN step converges. Relaxation occurs in the CLEAN algorithm once the second target has been found. At that stage, the second target's contribution is extracted from the original signal. The goal is to more accurately extract the first and strongest target a second time, without the mutual interference effects of the second target. Assuming that M (greater than 1) targets have been detected in a particular CLEAN step, RELAX re-extracts the strength and DOA, (a_p, θ_p) , of each target, p , after removing the other targets' ($m = 1: M, m \neq p$) contributions in the beamformer output:

$$|a_p|^2 = \max_{\theta_p} \left| \chi - \frac{1}{N} \sum_{n=1}^N \sum_{m \neq p} a_m e^{-j(n-1) \frac{2\pi d}{\lambda} (\sin\theta - \sin\theta_m)} \right|^2 \quad (2.5)$$

The re-extraction of target parameters is iterated until the residual energy at that step,

$|\chi|_{residual}^2|_M$, computed using

$$|\chi^2_{residual}|_M = \left| \chi - \frac{1}{N} \sum_{n=1}^N \sum_{m=1}^M a_m e^{-j(n-1) \frac{2\pi d}{\lambda} (\sin \theta - \sin \theta_m)} \right|^2 \quad (2.6)$$

converges. This procedure is repeated for each CLEAN step. The relaxation process described above, individually adjusts the values of all known targets in the absence of the contribution of the others.

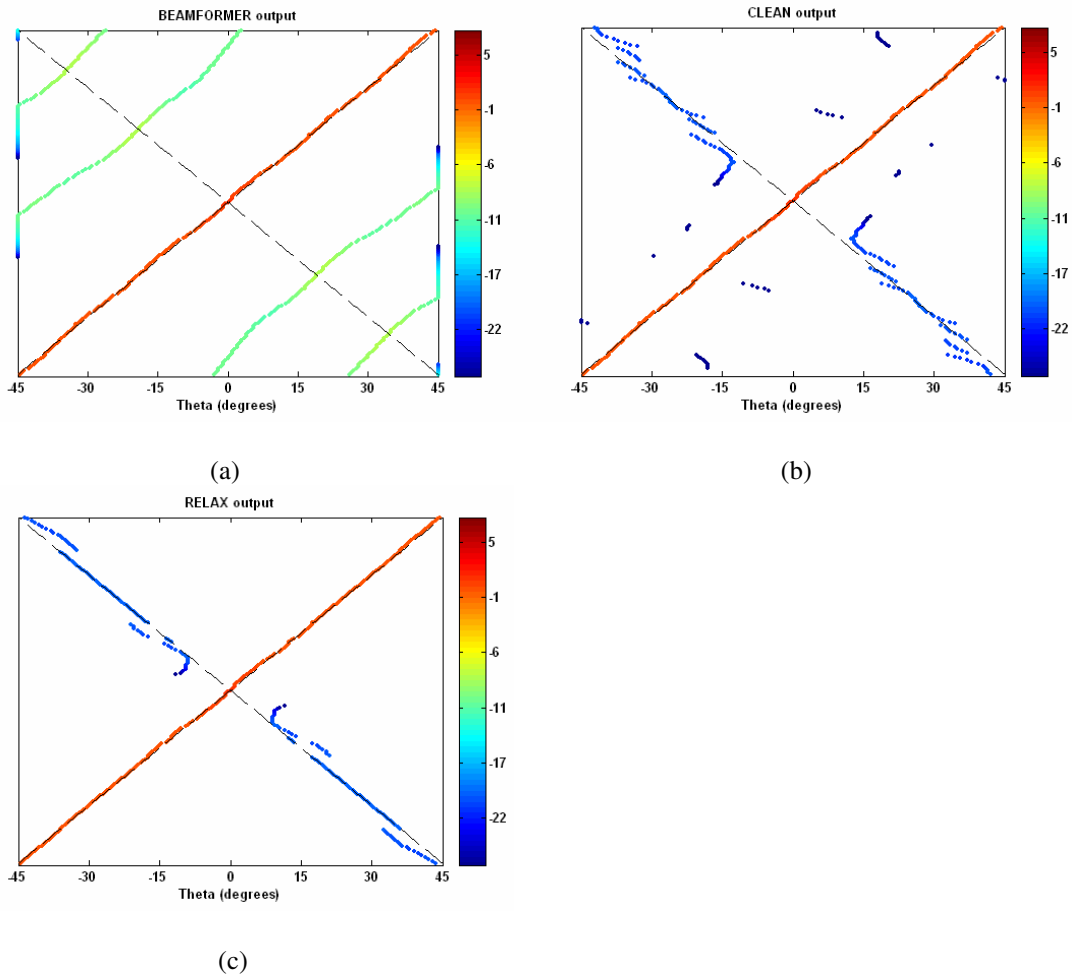


Fig.2.3. Simulation results when ratio of strength of targets is 20dB for (a) Spatial beamforming, (b) CLEAN and (c) RELAX techniques.

While this inner relaxation loop makes the algorithm computationally more expensive than ordinary beamforming and CLEAN, it allows the accurate determination of the number of targets. The results obtained when this algorithm is implemented for the two target scenario described earlier are presented in Fig.2.3c. It is observed that angular position and the strength of the two targets are detected with better precision. The number of erroneous detections or false targets is much smaller than the earlier cases. Additionally, successful detection is possible even when their angular separation is within the beamwidth of the antenna array. Thus RELAX enhances the performance of the CLEAN algorithm at the price of increased computation time.

2.5. MEASUREMENT RESULTS

Lin's radar testbed is upgraded in order to allow us test the concepts described earlier. The testbed consists of a continuous-wave transmitter operating at a frequency of 2.4 GHz and four receiving microstrip patch antennas fabricated on a 1.6 mm FR-4 substrate.

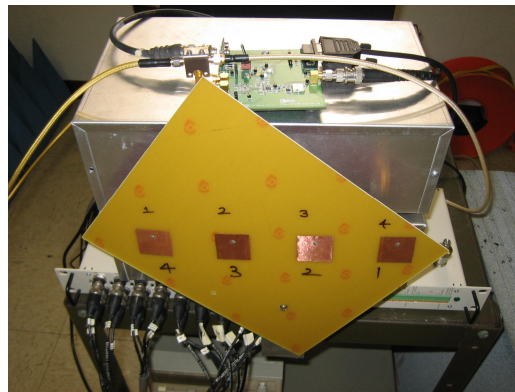


Fig.2.4. Photo of 2.4 GHz microstrip receiving array

The antennas are separated by $0.56\lambda_c$, to provide the maximum resolution while avoiding any grating lobes within the range -45° to 45° . Off-the-shelf quadrature receiver

boards (Analog Devices AD8347) are used to downconvert the received signals, which are then digitized for software processing. A photo of the receiving array is shown in Fig.2.4.

2.5.1. Indoor Line-of-Sight

First, measurements are conducted in indoor line-of-sight (LOS) conditions. Audio loudspeakers are used as steady test targets.

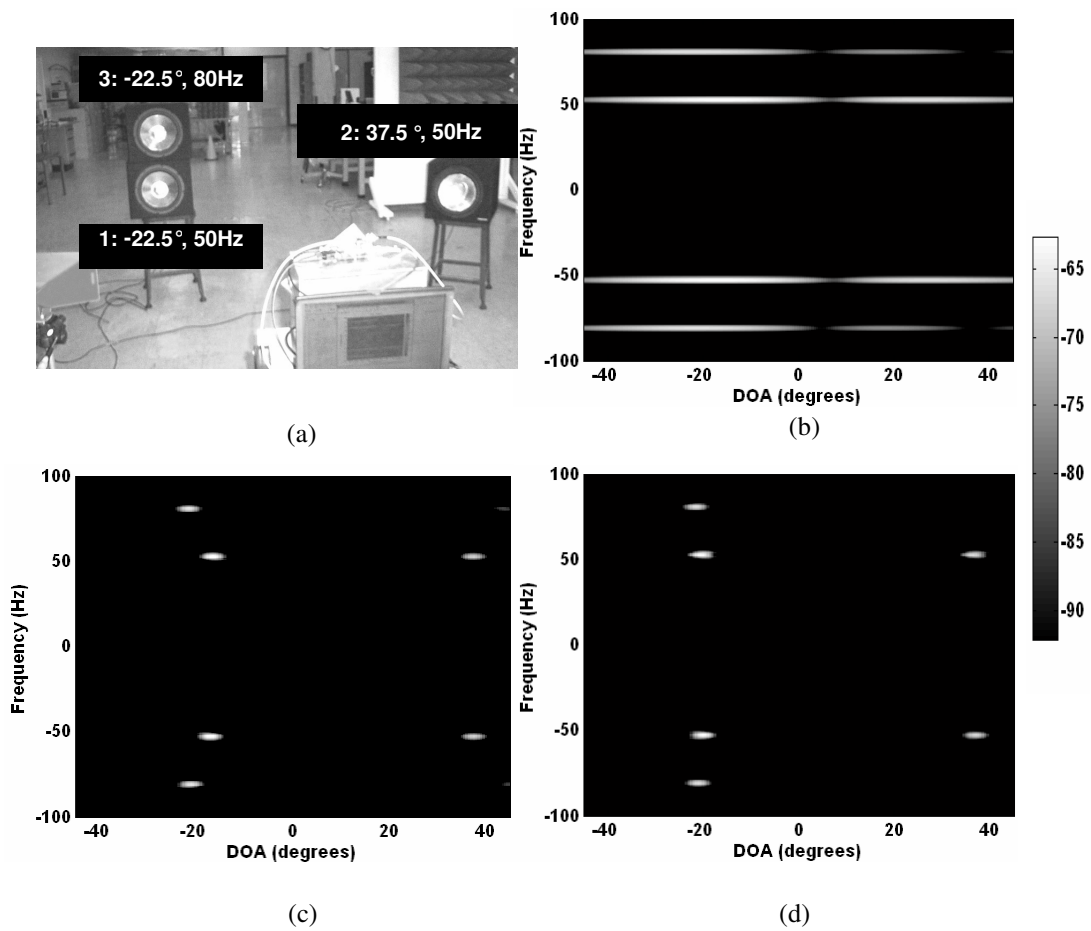


Fig.2.5. Three loudspeaker targets in indoor LOS resolved in the Doppler–DOA space, in decibel scale: (a) Experimental set up. (b) Beamforming result, (c) CLEAN result and (d) RELAX result.

The two-element DDOA radar reported in [22] is not capable of resolving targets of identical Doppler. To demonstrate that the current radar is capable of resolving targets of identical Doppler along the DOA axis, the following measurement is made with three loudspeakers as shown in Fig.2.5a. Speakers 1 and 2 are driven at the same audio frequency of 50Hz but have different DOAs while speaker 3 is driven at a different audio frequency, 80Hz, but has the same DOA as speaker 1. After Doppler processing and spatial beamforming are performed, the three targets are resolved in the Doppler-DOA space as shown in Fig.2.5b. However, the result is plagued by poor resolution and high sidelobes in the DOA dimension. Next, the CLEAN algorithm is tried on the same data. The discrete estimates of the DOA positions are obtained from the CLEAN algorithm. For display purpose, the extracted DOAs are convolved with a Gaussian point spread function of 5° beamwidth and displayed in Fig.2.5c. The CLEAN algorithm leads to improved results over standard beamforming, but a small yet noticeable error exists in the DOA estimate of speaker 1 due to the effect of speaker 2 at the same Doppler. The RELAX algorithm is next applied and the result is shown in Fig.2.5d. It is observed that the DOAs of the targets are estimated with greater accuracy. The computational time, however, is increased by a factor of four when compared to CLEAN. Measurements are next performed under the same indoor environment for three human subjects walking at a leisure pace. Subjects 1 and 3 approach the radar and have positive Dopplers, while subject 2 walks away from the radar and has a negative Doppler as shown in Fig.2.6a. Fig.2.6b through Fig.2.6d show respectively the beamforming, CLEAN and RELAX results for one captured time instant. In these figures it is observed that additional micro-

Doppler components populate the Doppler spectrum due to the arm and leg motions of each subject.

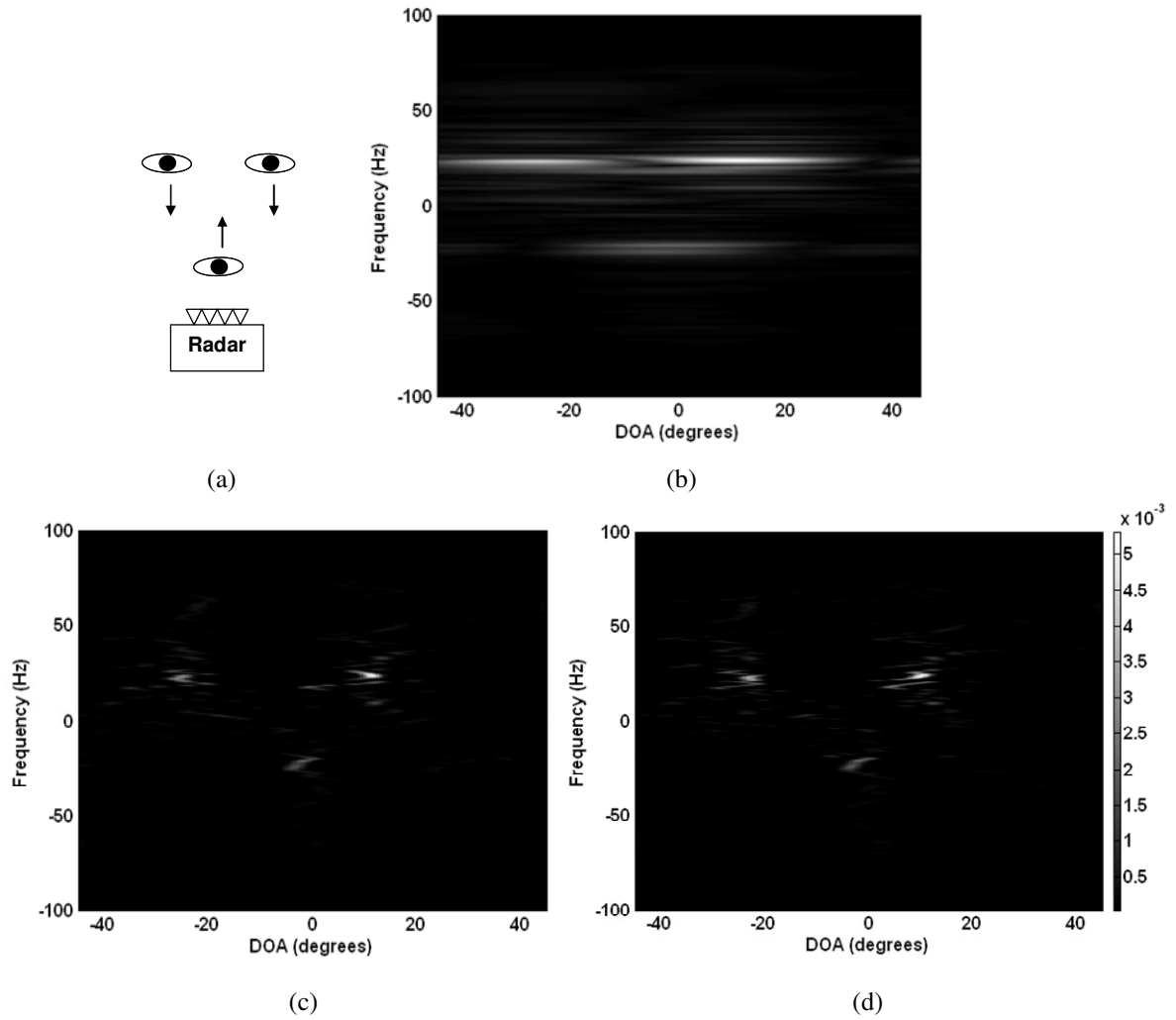


Fig.2.6. Three human subjects in indoor LOS resolved in the Doppler–DOA space: (a) Measurement setup, (b) beamforming result, (c) CLEAN result and (d) RELAX result.

In spite of the Doppler overlap, the targets can be resolved in the Doppler-DOA space. The CLEAN results again show much better target separation than standard beamforming. The RELAX results, however, do not show any significant improvement

over the CLEAN results. Hence in subsequent processed data, only the CLEAN results are shown.

2.5.2. Through-Wall

Next, measurements are conducted in a through-wall setup with two human subjects

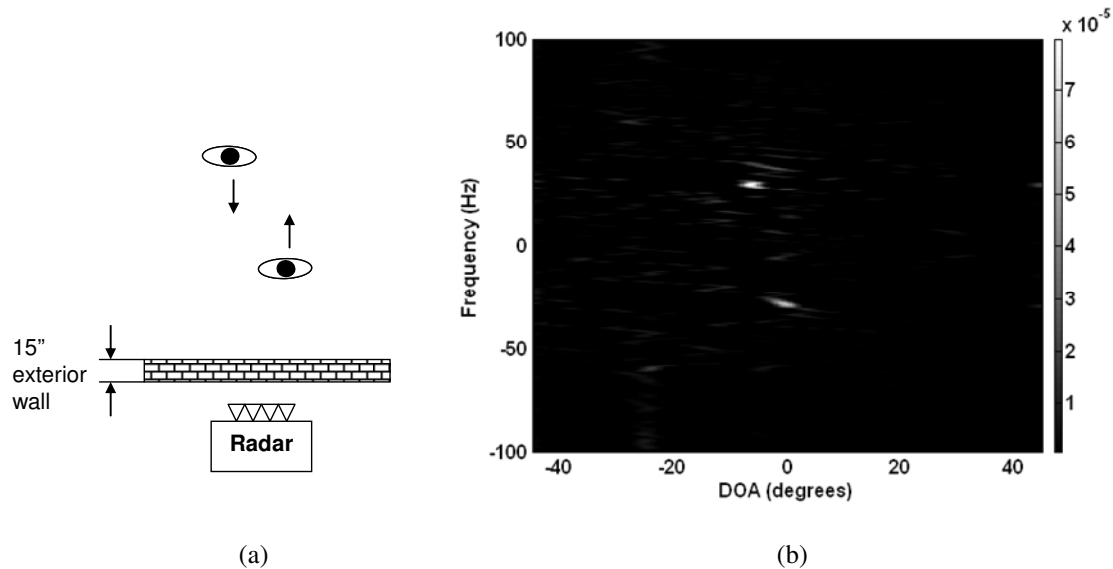


Fig.2.7. Two human subjects in a through-wall scenario resolved in the Doppler space: (a) Measurement setup and (b) CLEAN result.

separated from the radar by an exterior brick wall of 15” thickness. The distance between the radar and the wall is 3’. The transmit power used in the measurements is 15dBm. Fig.2.7 and Fig.2.8 show the results from the CLEAN algorithm for two measurement cases. In the first case, two human subjects at distances of 5’ and 15’ from the wall walk in opposite directions with respect to the radar as shown in Fig.2.7a. Fig.2.7b shows the CLEAN result for a single time instant. Although there is significant attenuation caused by the wall, it is observed that subjects with nearly identical DOAs can be well resolved

using Doppler processing. In the second case, the two subjects, separated from each other in bearing, walk together at the same pace first away from the radar from 5' to 15' and then turn around and move toward the radar, as shown in Fig.2.8a. Fig.2.8b shows the CLEAN result for a single time instant when the subjects approach the radar. It is seen that while the subjects have similar Dopplers, they can be well resolved in the DOA domain. Fig.2.8c shows the time-integrated Doppler-DOA map of the two subjects over the entire collection duration. Two clear tracks that are well resolved in the DOA space can be observed.

Finally, Doppler-shifted multipath signals can sometimes be observed using the 4-element array. In the setup, through-wall measurements are conducted with two loudspeakers separated from the radar by the same 15'' exterior brick wall as above. The two speakers are driven at different audio frequencies (50Hz and 80Hz) but placed at the same DOA (10°) as shown in Fig.2.9a. The results of the measurements are shown in Fig.2.9b where the two targets are well resolved in the Doppler space. However, a third ghost target is observed at Doppler of 50Hz and a DOA position of -12° . This is most likely caused by multipath through the window. While wall phenomenology can in general be very complex, this case shows that spatial beamforming can be used to resolve environmental multipaths that would have been problematic for a two-element array.

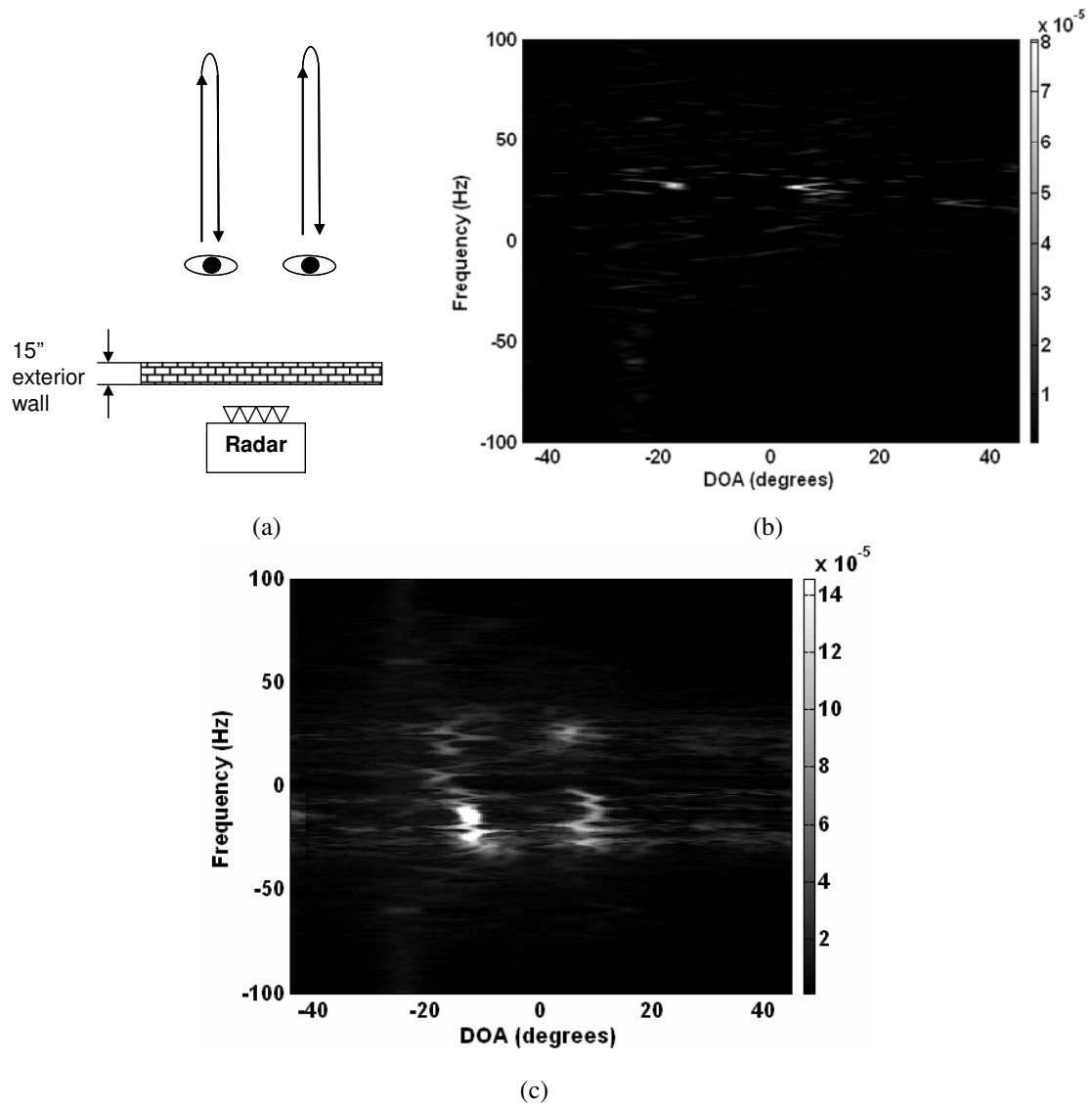


Fig.2.8. Two human subjects in a through-wall scenario resolved in the DOA space: (a) Measurement set up, (b) CLEAN result for a single time instant, (c) Time integrated CLEAN results.

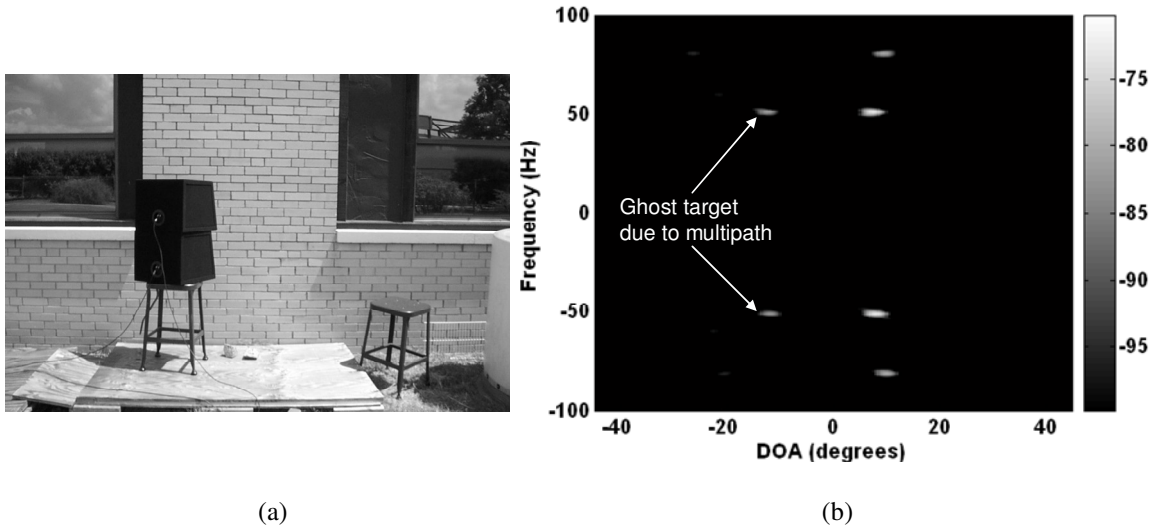


Fig.2.9. Two loudspeaker targets in a through-wall scenario resolved in Doppler in decibel scale: (a) Experimental set up and (b) CLEAN result.

2.6. CONCLUSION

Using the principles of Doppler processing and spatial beamforming, the performance of a radar for tracking multiple humans can be improved by using additional receiver elements. The resolution of the target along the DOA axis is limited by the beamwidth of the antenna array and the sidelobes give the appearance of false targets. To overcome these limitations, two algorithms, CLEAN and RELAX are investigated for use in conjunction with software beamforming. It was found that the CLEAN algorithm performed satisfactorily for multiple targets without excessive computational cost. These concepts are demonstrated by conducting measurements on different targets in line-of-sight and through wall scenarios. This Doppler radar is used to collect measured data to validate the results generated from the radar simulator developed in the subsequent chapters.

3. Joint Time-Frequency Transform

In this chapter, the joint time-frequency transforms used to process and display the time-varying microDoppler information are described. In particular, the reassigned joint time-frequency transform is investigated in addition to the traditional short-time Fourier transform. These transforms are applied to both simulated and measured human data throughout the rest of the dissertation.

3.1. INTRODUCTION

The swinging arms and legs of human movement give rise to interesting features termed microDopplers which are quite unique and have been studied through the use of joint time-frequency representations [30]-[33]. The most common joint time-frequency representation is generated by the application of the short-time Fourier transform (STFT) on the time domain radar signal. The resulting spectrogram is characterized by time-varying Doppler tracks due to the torso returns, along with weaker microDoppler features arising from the swinging arms and legs. However, a well-known limitation of the STFT is that it is not possible to obtain optimal precision or localization of the signal energy in the spectrogram. If the time extent of the window function used in the STFT is σ , the “thickness” of the signal feature in the spectrogram is σ in the time domain and $1/\sigma$ in the frequency domain. This issue becomes a limiting factor for discriminating the microDoppler features when the radar operating frequency is lowered to enhance the penetration of electromagnetic waves for through-wall applications. As a result of the

lower operating frequency, the Doppler sensitivity is reduced and it becomes increasingly difficult to discern the various microDoppler components in the spectrogram. One interesting question is whether the Doppler sensitivity problem at a low operating frequency can be overcome through the use of joint time-frequency representations other than the STFT. In this chapter, the reassigned joint time-frequency transform is investigated for the analysis of radar microDopplers from human gait.

3.2. DERIVATION OF THE REASSIGNED JOINT TIME-FREQUENCY TRANSFORM

The reassigned spectrogram (also called the time-corrected instantaneous frequency spectrogram) was first developed by Koderer et al. [48], and has subsequently been adopted in the acoustics community [49]-[50]. The derivatives of the phase of the traditional STFT spectrogram are used to derive the instantaneous time, t_{ins} , and instantaneous frequency, f_{ins} , of the signal. Each point in the STFT spectrogram is then *reassigned* to the coordinate positions (t_{ins}, f_{ins}) . This causes the signal energy to be localized in the spectrogram to thin lines of high precision and can lead to significantly improved readability of the traditional spectrogram. There are various implementations of the reassigned transform. The analytical method for computing the reassigned spectrogram proposed in [51] is summarized here. Given a signal $x(t)$, its standard STFT, $\chi(t, f)$, using a Gaussian window is given by:

$$\chi(t, f) = \int x(t') e^{-\frac{(t-t')^2}{2\sigma^2}} e^{+j2\pi f(t-t')} dt' = |\chi| e^{j\varphi} \quad (3.1)$$

Also needed is the spectrogram, $\eta(t,f)$, due to a time-product form of the Gaussian window:

$$\eta(t,f) = \frac{1}{\sigma} \int (t'-t)x(t') e^{-\frac{(t-t')^2}{2\sigma^2}} e^{+j2\pi f(t-t')} dt' \quad (3.2)$$

Then, the instantaneous frequency and the instantaneous time can be computed from χ and η as follows:

$$f_{ins} = \frac{1}{2\pi} \frac{\partial \varphi}{\partial t} = f + \frac{1}{2\pi\sigma} \text{Im} \left\{ \frac{\eta}{\chi} \right\} \quad (3.3)$$

$$t_{ins} = t - \frac{1}{2\pi} \frac{\partial \varphi}{\partial f} = t + \sigma \text{Re} \left\{ \frac{\eta}{\chi} \right\} \quad (3.4)$$

To form the reassigned spectrogram, a two-dimensional grid is created on the (t_{ins}, f_{ins}) plane. Each point in the STFT spectrogram is then reassigned to the coordinate positions (t_{ins}, f_{ins}) and appropriately weighted to ensure that energy is conserved during the transformation. This results in the reassigned distribution in the $t_{ins} - f_{ins}$ plane.

The reassigned transform is generated for a test signal comprising the sum of three signals: a click ($\delta(t-t_o)$), a ramp (e^{jat^2}) and white Gaussian noise. The STFT spectrogram of the signal is shown in Fig.3.1a. As expected, the thickness of the signal along the time and frequency axes is defined by the time window (0.1 s) and its inverse (10Hz). The reassigned transform is then applied to the signal, and the reassigned spectrogram is presented in Fig.3.1b. The click and the ramp in the reassigned spectrogram have nearly infinitesimal thickness, being limited mainly by the plotting pixel size of the image and not by σ . The white noise likewise transforms to thin veins

[51]. It is important to point out that the reassigned transform can resolve two signals only if they are farther apart than σ in the time domain and $1/\sigma$ in the frequency domain, i.e., outside the Fourier uncertainty bounds. Indeed, some slight distortions can be observed at the crossing point between the click and the ramp.

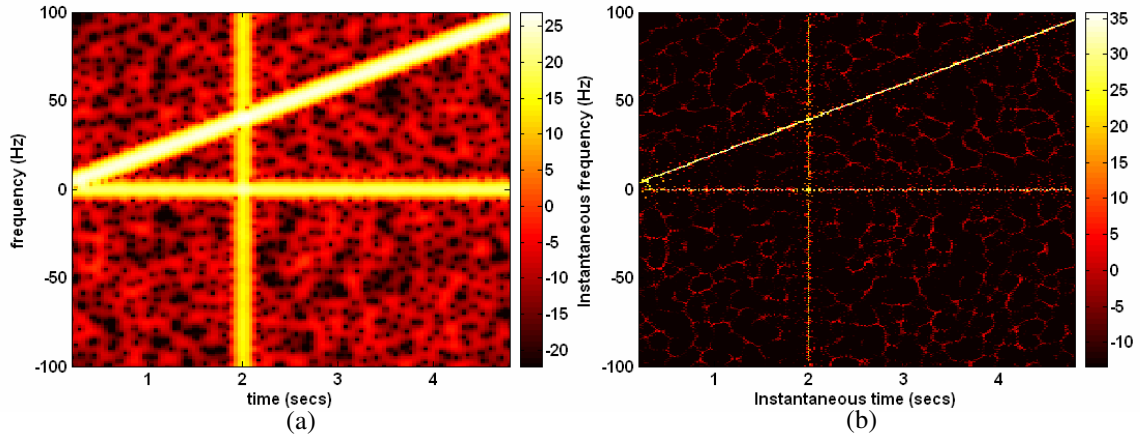


Fig.3.1. Spectrogram of a signal comprising a click, a ramp and white Gaussian noise. (a) STFT (b) Reassigned transform.

3.3. MICRODOPPLER FROM HUMAN GAIT:

3.3.1. Simulation Data

Next, the human microDoppler gait data is studied using simulation. The human body is modeled as a target with 12 body parts as shown in Fig.3.2a. The Thalmann model [40] is used to describe the human gait or the kinematics of the 12 body parts (i.e. the position of each body part versus time), as a function of the velocity of the human. Here, a human subject is assumed to approach a Doppler radar of 24GHz head-on at a velocity of 1.3m/s along a straight line path. The time-varying radar cross-section (RCS) of the human target is then obtained by the complex sum of the RCS of the individual

body parts modeled as perfectly conducting spheres, cylinders and ellipsoids. The radar return is obtained using the radar range equation. The STFT of the radar return from the simulated human gait data is presented in Fig.3.2b. A time window width σ of 0.25s is used in the STFT. Distinct time-varying Doppler tracks due to the motions of each of the parts of the body (labeled as **2 - 12**) are resolved in the spectrogram. The head which is mostly still does not give rise to significantly different Doppler from the torso. The strongest returns are from the torso (**2**) and the highest Doppler frequency arises from the motion of the feet (**7, 12**) followed by the lower legs (**6, 11**). It is clearly seen that the motion of the right arm (**3, 4**) accompanies the motion of the left leg and foot (**5, 6, 7**) and vice versa. The superior Doppler sensitivity results from the high carrier frequency chosen for the simulation. However, signal attenuation through walls at such a high frequency is very severe and a much lower frequency is needed for wall penetration.

Fig.3.2c shows the Doppler spectrogram that is generated when a carrier frequency of 2.4 GHz is used in the simulation. Again, a Gaussian time window of 0.25s is used. The strongest Doppler return is due to the torso where the center of gravity is located. The front and back swings of the arms and legs cause positive and negative Doppler spread with respect to the torso return. It is possible to discern the microDoppler tracks due to some body parts such as the torso (**2**) and the feet (**7, 12**). However, by and large, the different tracks appear vague and indistinct. It is now difficult to discern the various micro-Doppler components in the spectrogram. Hence there is a tradeoff between Doppler sensitivity and signal penetration through walls.

Fig.3.2d shows the reassigned spectrogram of the same data. It is observed that the precision of the signals in the spectrogram have been greatly improved which makes the reassigned spectrogram more readable compared to the STFT spectrogram.

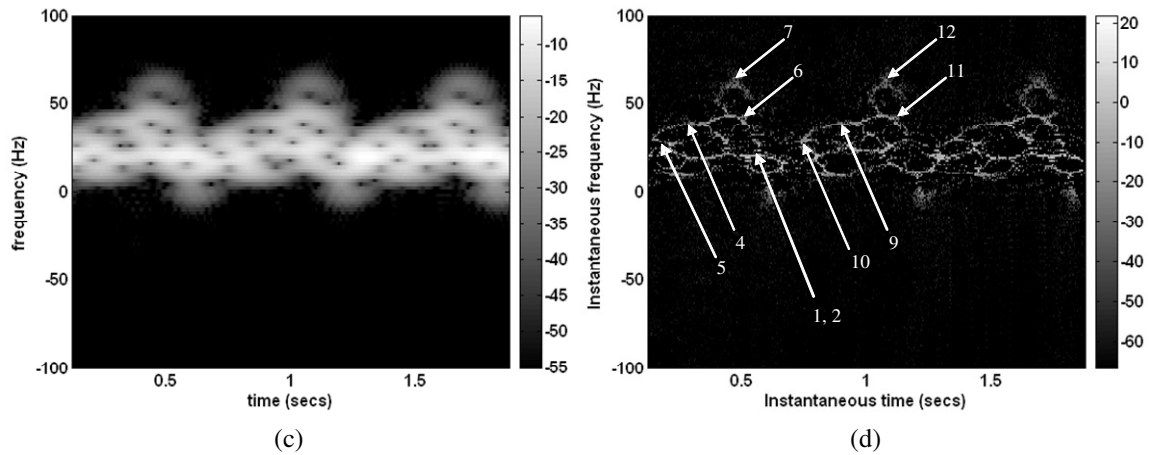
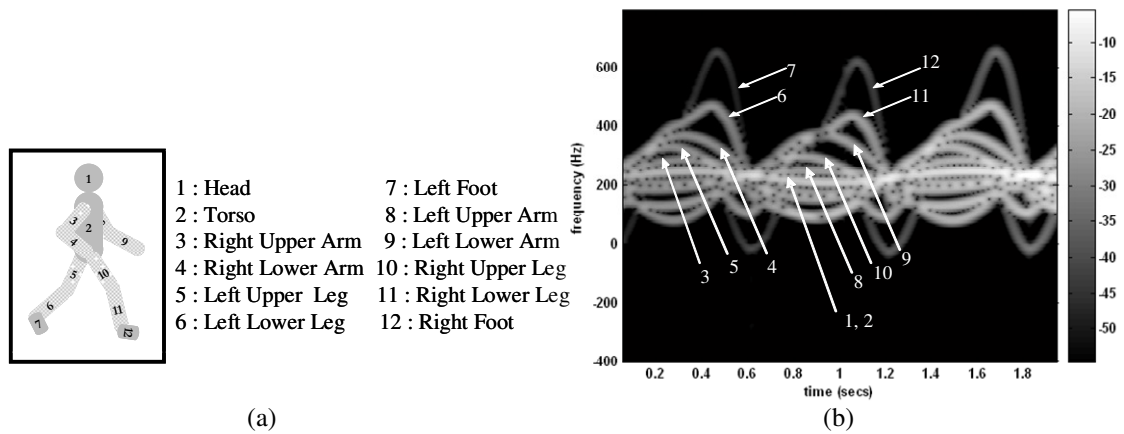


Fig.3.2(a) Simulation model of human walking at 1.4 m/s towards a Doppler radar. STFT of simulated returns for a carrier frequency of (b) 24 GHz, (c) 2.4 GHz. (d) Reassigned JTF of simulated returns for a carrier frequency of 2.4 GHz.

It is now possible to discern up to 9 distinct microDoppler tracks (labeled as **2, 4, 5, 6, 7, 9, 10, 11** and **12**). The weaker returns due to the upper arms (**3, 8**) however cannot be

distinguished from the stronger torso return (2). This is because the microDoppler features of the upper arms fall within the Fourier uncertainty bounds of the torso Doppler.

3.3.2. Measurement Data

Next, actual measurements are conducted using the 2.4 GHz Doppler radar discussed in Chapter 2. A human subject approaches the radar at the steady speed of approximately 1.4m/s. Fig.3.3a and Fig.3.3b show respectively the STFT spectrogram and the reassigned spectrogram. Again, the reassigned spectrogram shows better precision and thus improved readability for identifying the various Doppler tracks. Distinct microDoppler features from the feet, lower legs, lower arms, upper legs and torso are identified.

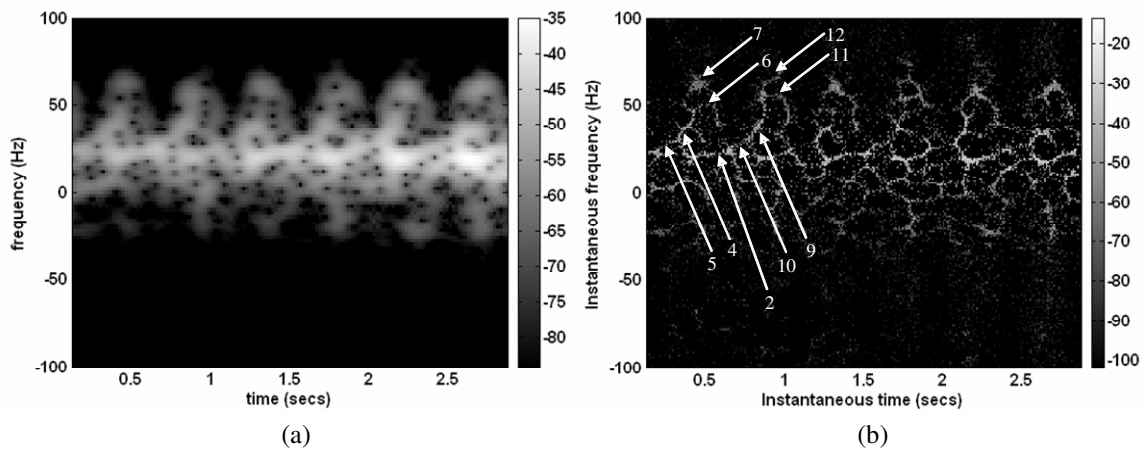


Fig.3.3. Spectrogram of human gait obtained by processing measured data from a 2.4GHz Doppler radar: (c) STFT. (d) Reassigned transform.

By comparing Fig.3.2d (simulated) and Fig.3.3b (measured), it is observed that they differ somewhat in the detailed Doppler tracks. A possible factor that may contribute to this difference is that the simulated motions are derived from the Thalmann model which

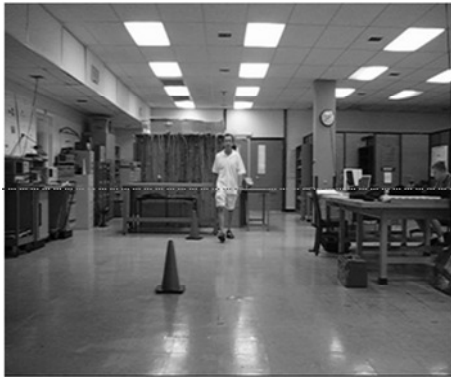
describes the motion of only 12 human body parts. Also, the model is an “averaged” kinematic model. In the subsequent chapters, computer animation data derived from motion capture technology are used to model human motions more accurately.

3.3.3. Analyses of Deviated Walking Motions

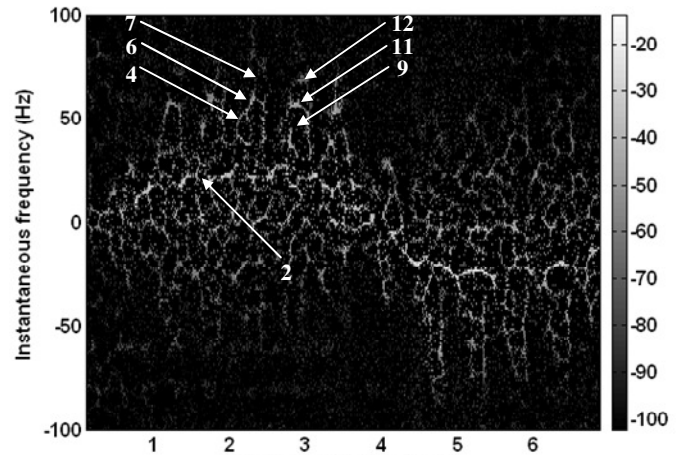
The unique characteristics of the micro-Doppler features make the human Doppler spectrograms potentially useful for identifying and classifying different types of movements [35]-[39]. This is illustrated by examining the spectrograms of some deviated walking motion data collected using the Doppler radar testbed. In the first measurement, the human subject walks toward the radar head-on from a distance of 10m (Fig.3.4a) and then turns around at 4m and walks away from the radar. The reassigned transform is applied to the radar data and the resulting spectrogram is shown in Fig.3.4b. It is observed that the Doppler track of the torso (**2**) is first positive, then negative during the 7s data collection. Some of the micro-Doppler features can be identified in the spectrogram such as the feet (**7, 12**), lower legs (**6, 11**) and lower arms (**4, 9**).

Next the subject repeats the same motions while carrying a metal corner reflector in his right hand (Fig.3.4c). The reassigned Doppler spectrogram of the data is generated and presented in Fig.3.4d. It is observed that the Doppler spectrogram in Fig.3.4d is almost identical to that in Fig.3.4b, except that the micro-Doppler feature from the right hand (**4**) has been enhanced. In the next measurement, the subject walks the same path while carrying a heavy box using both hands as shown in Fig.3.4e. This action causes the subject’s walking pattern to change considerably and is reflected in the reassigned

spectrogram shown in Fig.3.4f. The Doppler features of the right leg and foot are altered since that leg moves slower than the other one. The Dopplers of both arms are also changed, though more subtly. In the last measurement, the subject repeats the same path while using a long metal pole in his right hand, like a walking stick, as shown in Fig.3.4g. In the reassigned spectrogram of the motion shown in Fig.3.4h, a high Doppler component is observed slightly ahead of the Dopplers due to the right leg, caused by the motion of the pole. It is clear from these measurements that deviated walking patterns give rise to noticeable variations in the reassigned spectrograms.



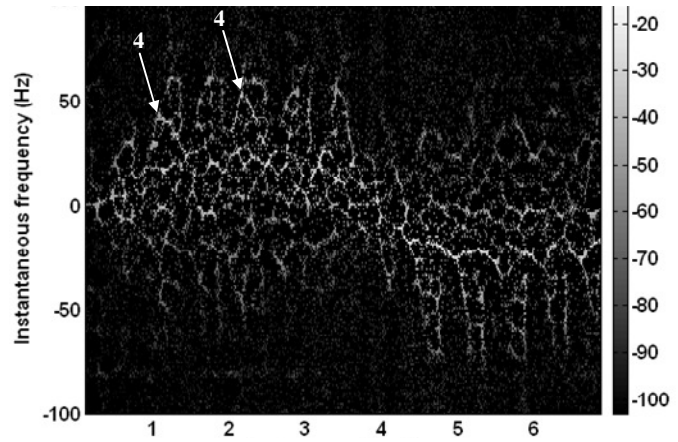
(a)



(b)



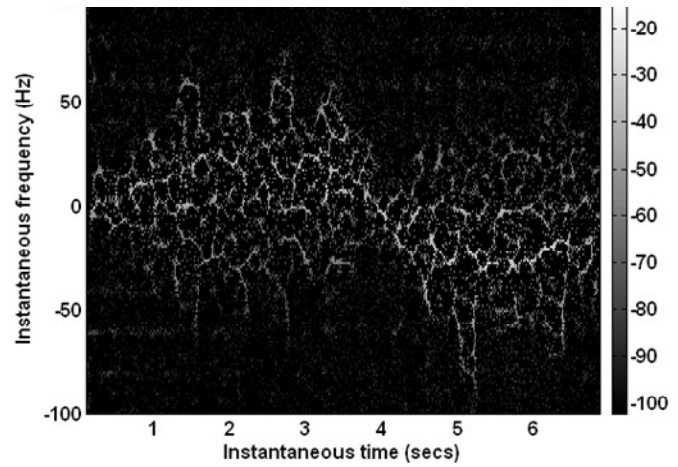
(c)



(d)



(e)



(f)

Fig. 3.4. Caption follows

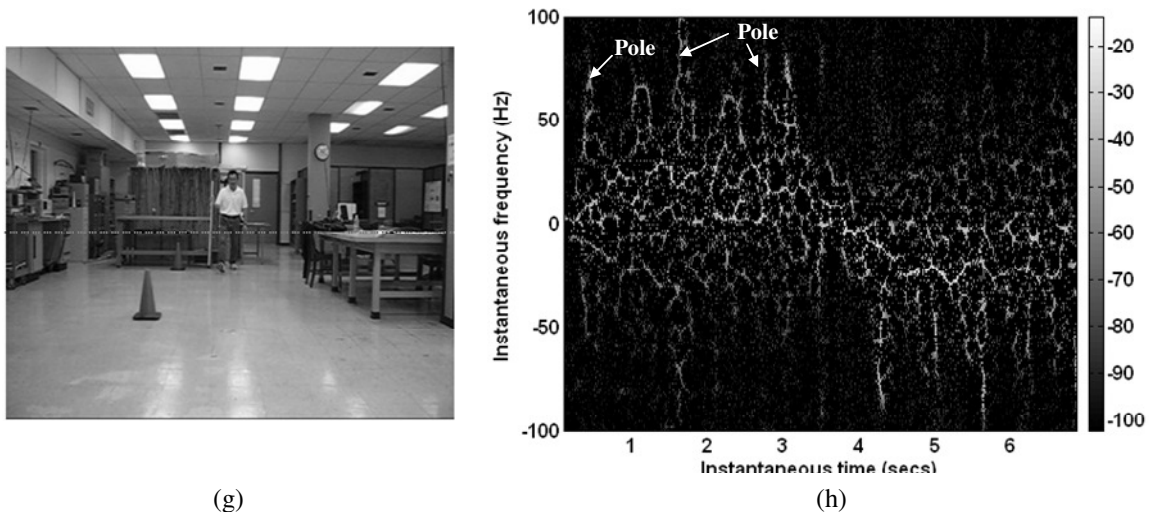


Fig.3.4. (a) Case 1: walking human subject, (b) Reassigned spectrogram of case 1
(c) Case 2: walking human subject holding a light horn reflector in the right hand,
(d) Reassigned spectrogram of case 2
(e) Case 3: walking human subject holding a heavy metal box on his right with both
hands, (f) Reassigned spectrogram of case 3
(g) Case 4: walking human subject holding a pole in the right hand,
(h) Reassigned spectrogram of case 4.

3.4. CONCLUSION

The reassigned joint time-frequency transform was applied to the Doppler spectrogram of a walking human. The results were compared with the standard spectrogram. It was demonstrated that this transform enabled the discernment of distinct microDoppler features that arise from the motions of specific parts of the body. This transform will be used in the subsequent chapters to do detailed analysis of microDopplers to better understand the inherent phenomenology in RF sensing of humans.

RADAR SIMULATION MODEL

4. Radar Simulation of Humans

The main focus of this dissertation is to develop a radar simulator for complex human motions for applications in the RF sensing of humans. The simulator will incorporate Doppler based scattering mechanisms of a human mover, the through-wall propagation effects and the sensor physics. In this chapter, the methodology for generating the Doppler spectrograms of different complex human motions is presented.

4.1. INTRODUCTION

To date, the radar returns from the simple motion of a human walking at constant velocity has been simulated by van Dorp [33] using the Thalmann model [40]. The Thalmann model is a three-parameter model that completely describes the dynamics of different body parts as a function of time. However, this model is limited to the walking motion and cannot be used to simulate more complex motions such as running, crawling etc. On the other hand, MOCAP technologies have been used extensively by animation industries, for generating a detailed description of almost any complex human motion. Hence, in this dissertation, we develop an approach that exploits animation data available from MOCAP with electromagnetic models of the human body to simulate human radar returns.

There has been some research undertaken to characterize the radar signatures of humans using computational electromagnetic techniques such as the finite-difference time-domain (FDTD) technique [41] and high-frequency ray tracing [42]. FDTD is a full-

wave electromagnetic solver that yields highly accurate radar signatures of a still human. Xpatch, based on the shooting and bouncing ray technique, was also found to be satisfactory in generating human signatures. However, neither of these techniques is well suited for generating the radar signatures of dynamic human motions. These techniques require detailed computer models of humans over multiple poses and are computationally very expensive to carry out. Simpler models have also been developed to simulate the constant velocity walking motion of a human [30], [33]. In [30], infrared motion capture data of the different limbs were combined with a point scatterer model to generate the Doppler spectrogram. In [33], van Dorp proposed a simple primitive based prediction technique to model constant velocity human gait described by the Thalmann model [40]. The different parts of the human body are modeled as primitive shapes such as ellipsoids and spheres whose radar cross sections (RCS) are well characterized. By using the time-varying phase centers of the different body parts of a walking human, one can readily compute the total RCS of the human at different time instances for different human poses. Though the primitive based technique does not model shadowing and multiple interactions between the different body parts, it is computationally fast and reasonably accurate. Hence, the approach in this dissertation is to integrate the electromagnetic model based on the primitive based prediction technique with the MOCAP data to model the returns from complex human motions

The chapter is organized as follows. First, the technique for simulating the human radar signatures from MOCAP data is presented. Then MOCAP data and radar measurement data of a moving human subject are simultaneously generated in the

laboratory using the Doppler radar testbed described in Chapter 2. The results from the radar simulation model generated from the MOCAP data are compared with the measured data. Next, the microDoppler signatures of some common human motions such as walking, running, crawling, jumping etc are generated using the computer animation data that are available from the video gaming and animation movie industries. Different formats of animation data files are available. Here BioVision's BVH data format and Acclaim's ASF/AMC data format are used to simulate different human motions. Additional simulation data are presented to show patterns over a long time duration and the effect of frequency and viewing angle. Also, the detailed microDoppler analysis of some animal motions such as a galloping horse and trotting dog are presented. Finally, the microDoppler signatures of some anomalies in the human gait patterns are examined, such as walking while holding an object. This is carried out by comparing the anomalous gait signatures with that from normal gait.

4.2. METHODOLOGY

In this section, the methodology used to simulate Doppler radar returns using computer animation data is presented. In the first step, the three-dimensional position of each bone of the human body is obtained at each time instant from input animation files. In the next step, the time-domain returns of the human mover are generated by computing the radar cross-section (RCS) of the human at each time instant using a primitive based predictor.

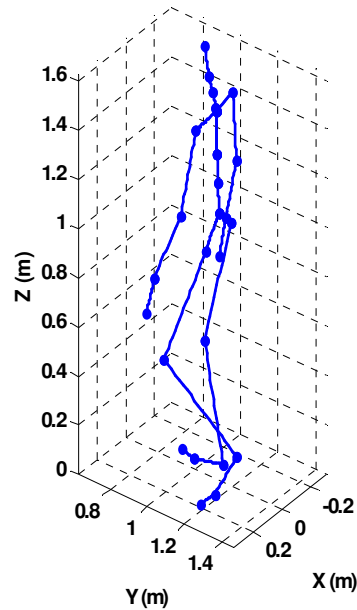


Fig.4.1. Animation model of walking human.

There are several standard formats for computer animation files, such as BVH, ASF/AMC, etc which share a common format. The files are usually divided into two parts. The first part specifies the initial pose of the human. This section is under the header 'skeleton' in the BVH data files and is a separate file with the file extension '.asf' in the ASF/AMC data format. A hierarchical distribution of the bones in the human body is described in this part as shown in Fig.4.1. Each bone is connected to a parent bone through a joint. Bones that are not connected to child bones are terminated with end-effectors instead of joints. The relative length and orientation of each bone are specified by the vector defined between the three-dimensional positions of the two joints (or end-effector) connected to them. The center of gravity of the human lies at the hip (root) joint.

The root joint is subject to 6 degrees of freedom (DOF) with respect to the initial pose. This includes translation of the position vector of the root along the X , Y and Z axes as well as Euler rotation angles (α, β, γ) about the X , Y and Z axes respectively. All the other joints are subject to 3 DOF which are the Euler rotation angles. The changes in the DOF data of the joints over time give rise to animation motion of the human. These changes are specified for each frame of the animation under the header 'motion' in BVH data files and in a separate file with the file extension '.amc' in the ASF/AMC data files.

The global three-dimensional position vector of each bone is derived using the matrix operations discussed in [56]. First, a local transformation matrix (\mathbf{M}_{bone}) is created for each bone from the local translation (\mathbf{T}) and rotation information of that bone. For any bone, the translation information is the offset of the bone from its parent which is specified in the skeleton section. For the root joint, the translation data is obtained from the motion section of the data file. Based on the DOF data specified for each joint by the motion section, a rotation matrix (\mathbf{R}) is computed by multiplying 3 separate rotation matrices ($\mathbf{R}_x, \mathbf{R}_y, \mathbf{R}_z$), one for each axis of rotation:

$$\mathbf{R} = \mathbf{R}_x \mathbf{R}_y \mathbf{R}_z \quad (4.1)$$

The order of multiplication of the three rotation matrices $\mathbf{R}_x, \mathbf{R}_y$ and \mathbf{R}_z is specified in the data files. The position of each bone is obtained from the transformation matrix (\mathbf{M}) computed by concatenating the local transformation matrix of the bone with the local transformation of its parent, then its grandparent, and so on:

$$\mathbf{M} = \mathbf{M}_{bone} \mathbf{M}_{parent} \mathbf{M}_{grandparent} \dots \quad (4.2)$$

In order to compute the RCS of the human, the primitive based model is used. An electric field incident on the moving human in free space is given by:

$$E_i(r) = \frac{A}{r} e^{-j \frac{2\pi f_c}{c} r} \quad (4.3)$$

where f_c is the transmitter frequency, A is a constant related to the gain of the antenna, and r is the distance from the transmitter to the human. If there are no interactions between the different human body parts and a monostatic radar configuration is assumed, the scattered field from the human, $E_s(t)$, can be generated by the complex sum of the RCS, σ_b , of all N body parts as follows:

$$E_s(t) = \frac{A}{\sqrt{4\pi}} \sum_{b=1}^N \sqrt{\sigma_b(t)} \frac{e^{-j \frac{2\pi f_c}{c} 2r_b(t)}}{r_b^2(t)} \quad (4.4)$$

In the above sum, the distance from the phase center of each part to the radar $r_b(t)$ is used to account for the different phase delays from the body parts. The human head is modeled as a sphere and the rest of the body parts associated with the other bones in the skeleton structure as ellipsoids, whose RCS is given in closed form by [57]:

$$\sqrt{\sigma_b(t)} = \Gamma \left[\frac{\frac{1}{4} \pi R_e^4 H_e^2}{(R_e^2 \sin^2 \theta_e(t) + \frac{1}{4} H_e^2 \cos^2 \theta_e(t))^2} \right]^{1/2} \quad (4.5)$$

Here R_e and H_e correspond to the radius and length of the ellipsoid with a circular cross-section and θ_e is the angle between the incident wave and the length axis of the ellipsoid. The phase center location, $r_b(t)$, of an ellipsoid for a monostatic radar can be fairly well

approximated by the point on the surface of the ellipsoid nearest to the radar. Since the human is not perfectly metallic, the relative permittivity of human flesh is incorporated into the calculation of the approximate value of the Fresnel reflection coefficient, Γ , of the wave reflected by the primitive. For Γ , the Fresnel reflection coefficient at normal incidence [58] is used:

$$\Gamma = \frac{\sqrt{\frac{j\omega_c \mu_o}{\sigma + j\omega_c \epsilon_o \epsilon_r}} - \sqrt{\frac{\mu_o}{\epsilon_o}}}{\sqrt{\frac{j\omega_c \mu_o}{\sigma + j\omega_c \epsilon_o \epsilon_r}} + \sqrt{\frac{\mu_o}{\epsilon_o}}} \quad (4.6)$$

Here, μ_o and ϵ_o are the permeability and permittivity of free space. The conductivity σ , and the dielectric constant ϵ_r , of human body tissue are approximately 2 and 80 respectively [59]. As a result of combining equation (4.5) and the motion information in the animation data, we can readily simulate the time-varying radar returns from the human in free space. Note that shadowing and multiple interactions between the different parts are not incorporated in this model.

Once the return signal is simulated, the Doppler spectrogram, $\chi(t,f)$ of the motion from the short-time Fourier transform of $x(t)$ according to equation (3.1). It is important to note that the animation data is provided at a fixed frame rate usually ranging from 60 frames per second to 240 frames per second. The data need to be interpolated to provide sufficient Doppler bandwidth to avoid aliasing effects. This is particularly important at higher radar operating frequencies, since the Doppler bandwidth is directly proportional to the radar frequency. The interpolation is implemented by introducing spline

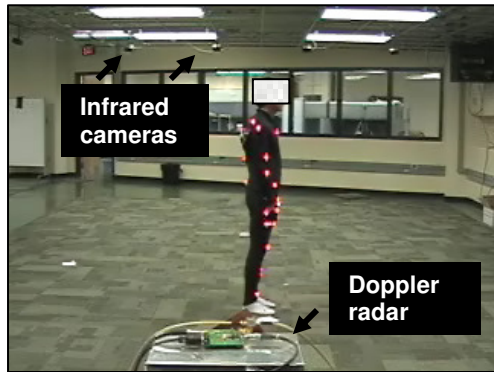
interpolation to the rotational angle and translational position data obtained from the animation files. However, the resultant interpolated data do not always correctly model the kinematics of rotating objects. A better way to interpolate the data, called the spherical linear interpolation (SLERP), has been widely adopted in the animation community [60]. It is based on describing the translation and Euler rotations of every joint using a four-coordinate system called a quaternion. Linear interpolation of data is carried out along the surface of the quaternion unit sphere. In this dissertation, this latter approach is used to interpolate the animation data.

4.3. VERIFICATION OF SIMULATION METHODOLOGY WITH JOINT COLLECTION OF MOCAP AND RADAR MEASUREMENT DATA

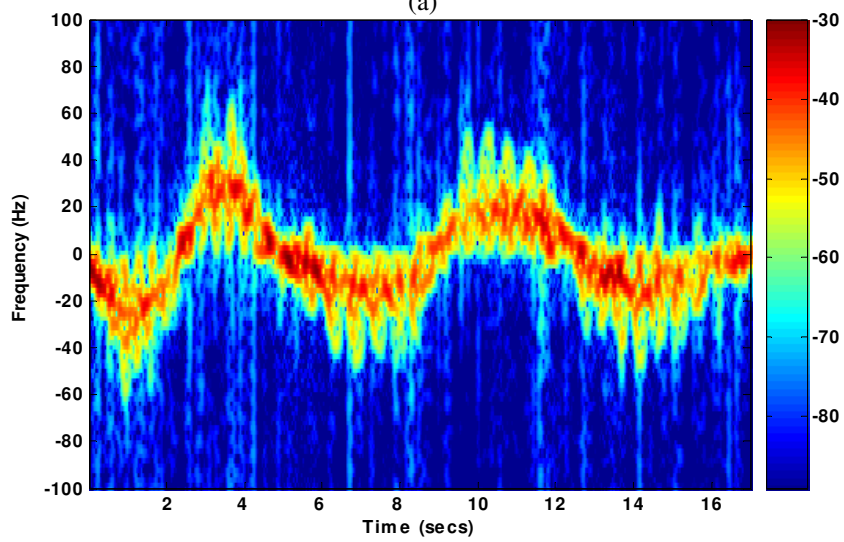
In this section, the simulation methodology described in the previous section is validated in the following manner. Motion captured data and radar measurement data of a moving human subject are simultaneously collected using the MOCAP system at the University of Texas Virtual Reality Laboratory and the Doppler radar testbed described in Chapter 2. Using the techniques described above, the Doppler radar spectrograms of the human motions are simulated from the MOCAP data and are validated with the spectrograms generated from actual radar measured data.

The MOCAP system consists of 16 infrared cameras that are used to locate the three-dimensional positions of 48 sensors attached at different joints on the human subject as shown in Fig.4.2a. Simultaneously, Doppler radar data are collected using the 2.4GHz Doppler radar testbed. As the human subject moves, the Doppler shifted radar

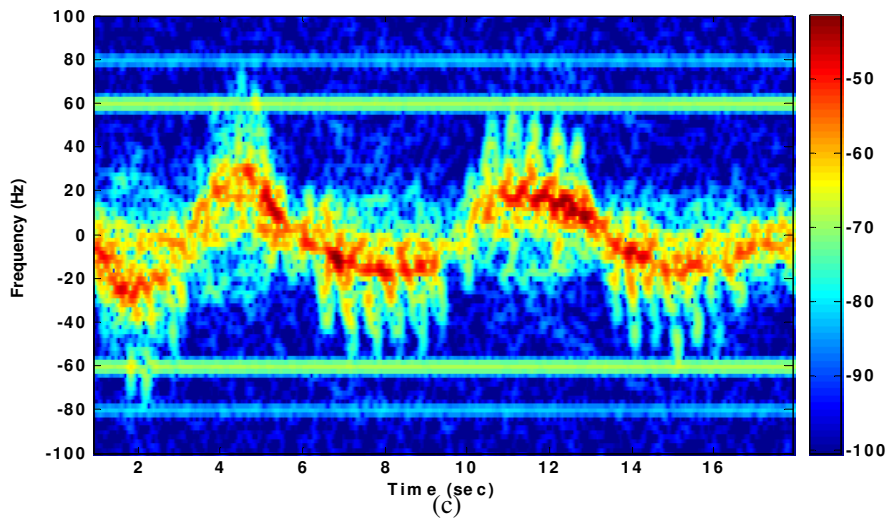
returns are collected and processed by STFT to generate the Doppler spectrogram of the human subject as shown in Fig.4.2b. Over the 18 seconds collection interval, the subject undergoes a variety of movements. The Doppler of the human is positive with the subject moving towards the radar and negative with the subject moving away from the radar. The motions of the arms and legs modulate the received signal and result in the microDoppler features that are observed in the Doppler spectrogram. The largest microDopplers come from the feet and legs. Fig.4.2c shows the resulting spectrogram from the simulated data. It is observed that the Doppler features in the spectrograms generated from measured and simulated data look very similar. This is particularly discernible in the fine Doppler features arising from the motions of the human subject's legs (for example: 6 – 10s in the Doppler spectrograms). However, there are some differences in the two spectrograms. In Fig.4.2b, some radio frequency interference at $\pm 60\text{Hz}$ and $\pm 80\text{Hz}$ are observed due to the collection environment inside an office. Secondly, the simulation model appears to over estimate the RCS of the limbs in Fig.4.2c. Also some of the highest Dopplers in Fig.4.2b do not appear in Fig.4.2c due to the fact that infrared sensors were not placed on the feet of the human subject during motion capture. Hence the 3D position data of the feet were not captured. Despite these differences, it appears that the primitive based model of humans is reasonably accurate in capturing the key radar features of a human.



(a)



(b)



(c)

Fig.4.2. Caption follows.

Fig.4.2. (a) Generation of infrared motion capture data and Doppler radar data of a moving human object. Doppler spectrogram of human motions at 2.4 GHz generated from (b) motion capture data and (c) measurement data.

4.4. SIMULATION RESULTS

4.4.1. Motion Diversity

Using the techniques discussed above, the microDoppler signatures of some common human motions are simulated and examined in this section. The animation motions are further replicated in the laboratory by a human subject and measurement data are collected using the Doppler radar testbed. The simulated and measured spectrograms are compared.

a. Walking

First, human walking motion data from Sony Computer Entertainment America are considered. The animation data specify the motion of 28 bones in the human body at a frame rate of 120 frames per second. This data is interpolated to a sampling frequency of 200Hz. The radar is assumed to be placed at the 3-D coordinate position (-5, 1, 0) m as shown in Fig.4.3a. The carrier frequency is set at 2.4GHz. The animated human walks towards the radar for 4s and then turns around and walks away from the radar. The time-domain radar returns are computed and the Doppler spectrogram is generated and shown in Fig.4.3b. The strongest Doppler return is from the torso, which is positive when the mover approaches the radar and negative when the mover moves away from the radar. The motion of the feet and lower legs give rise to the highest Doppler returns. The

motion shows periodicity that corresponds to the uniform stride motion of the human. This motion is replicated by a human subject before the Doppler radar testbed. Fig.4.3c shows the spectrogram resulting from the measured data. It is observed that the spectrogram shows good correspondence to the spectrogram generated by the simulated walking pattern shown in Fig.4.3b. The Doppler components from the torso and the lower legs and feet are easily discerned.

b. Running

The procedure is next repeated for running motion. In this case, the human runs around a circular path as shown in Fig.4.4a. The Doppler spectrogram of this motion is shown in Fig.4.4b. It is observed that the Doppler return of the torso is much higher than the torso Doppler while walking due to the increased speed of the body motion. The microDoppler spread is also much higher arising from the motions of the different limbs. In particular, it is now possible to observe both the front and back swing of the lower legs and feet. At the 3.5s time instant, the Doppler track shows a steep change from the positive to negative Dopplers. This corresponds to the position of closest approach to the radar as shown in Fig.4.4a. Next, the measurement is made for running motion over a circular track and the resulting spectrogram is shown in Fig.4.4c. Again, the result is similar to the simulation results shown in Fig.4.4c. Considerably high Dopplers from the torso and the lower legs are observed. Also the backswing from the legs and feet are more persistent. The DC line in the spectrogram comes from the residual clutter after the low pass filter in the radar.

c. Crawling

Next, the human crawling motion is simulated using ASF/AMC data obtained from the CMU Graphics Lab Motion Capture Database shown in Fig.4.5a. The radar is assumed to be situated at the coordinate position (5, 1, 0) m. The Doppler spectrogram of the motion, (shown in Fig.4.5b) shows considerable deviation from the spectrograms obtained from the walking and running motions. First, the torso Doppler is much lower (nearly zero) in this case. Also, the microDoppler arising from the legs are lowered and are now comparable with the microDoppler from the arms. From a detailed analysis of the simulated spectrogram, it is possible to infer that the microDoppler of the left / right arm is slightly ahead of the microDoppler of the right / left leg. Next, measurements are performed for the crawling motion of the human subject. The Doppler spectrogram is shown in Fig.4.5c which shows good agreement with the simulated spectrogram shown in Fig.4.5b. The spectrogram shows considerable deviations in the microDoppler features when compared to the spectrogram of a regular walking pattern in Fig.4.5b.

d. Walk-Jump-Walk

Fig.4.6a shows an animated human that walks at a fairly uniform speed and then jumps forward using both legs and then resumes walking towards the radar. This data is obtained from ACCAD Motion Capture Lab from Ohio State University. The microDoppler signature of this motion is presented in Fig.4.6b. In the first three seconds, the microDoppler pattern shows the uniform human walking signature. The motions of the right and left limbs alternate. In each stride, the highest Doppler arises from the

motion of the legs. There is a noticeable variation in the Doppler pattern when the human jumps forward. The Dopplers from this motion are much higher. Also, the time between the motions of the right and left legs differ from the steady transition time during the uniform walking motion. Once the human has landed from the jump, the regular walking motion is resumed which is clearly reflected in the Doppler spectrogram in the final second. Next, this animation motion is replicated by a human subject in the laboratory. The spectrogram generated from the measured data is presented in Fig.4.6c. From the figure, it is apparent that there is general similarity in the measured and simulated spectrograms. The steady stride motion is observed from 0 to 3s which is followed by the jump motion, after which the walking motion is resumed.

The key differences observed in the measured and simulated spectrograms are caused by the difficulty in replicating the exact animation motion during measurement data collection. In addition, the negative Dopplers that are observed in the measured spectrograms arise from the IQ imbalance in the quadrature receiver of the Doppler radar.

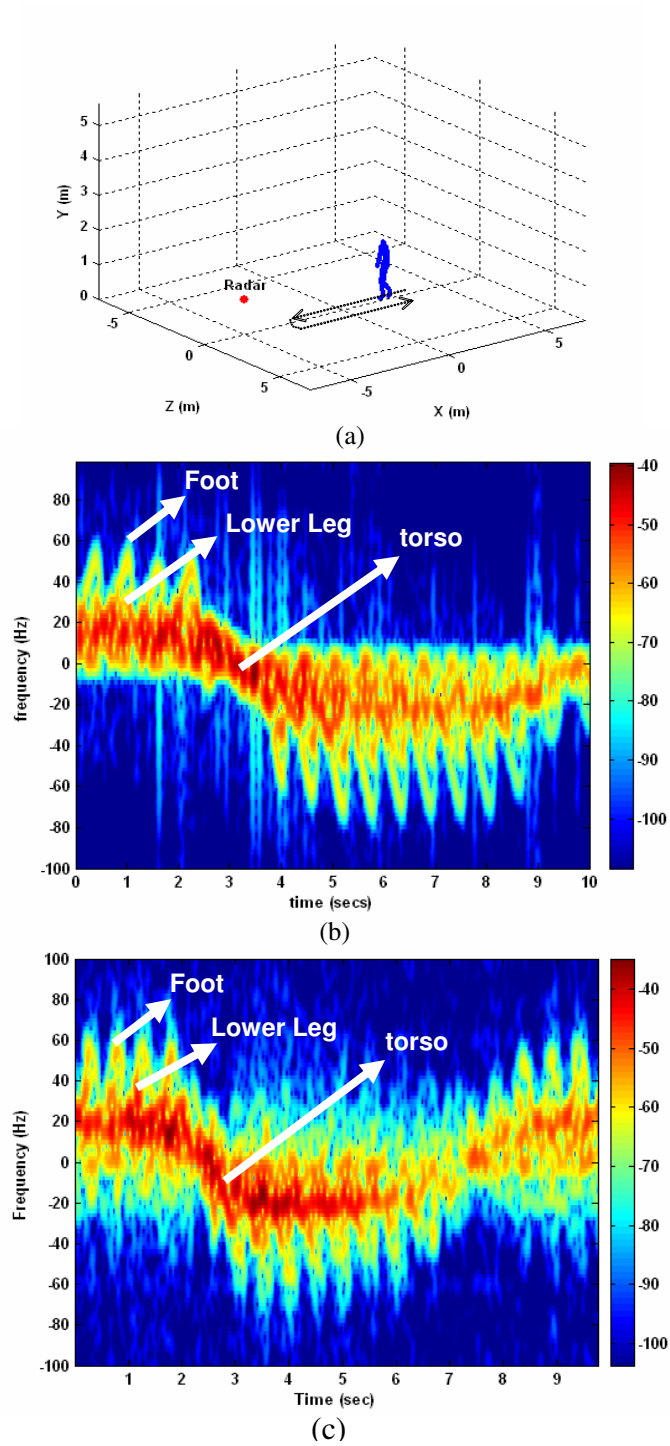


Fig.4.3.(a) Animation model of human walking motion from Sony Computer Entertainment America. Doppler spectrogram of human walking motion at 2.4 GHz generated from (b) simulation data, (c) measurement data.

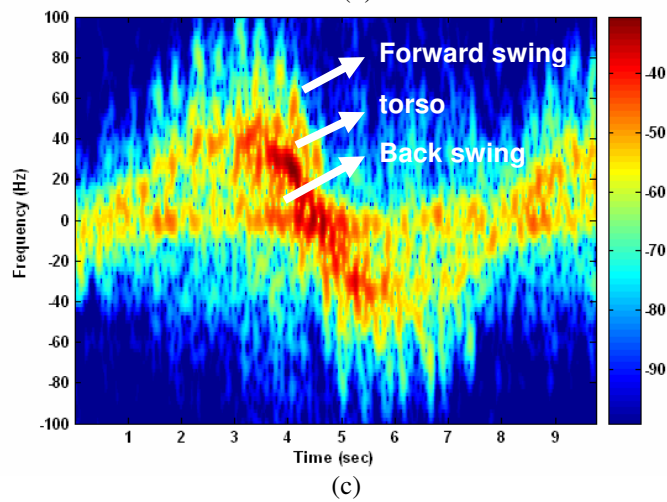
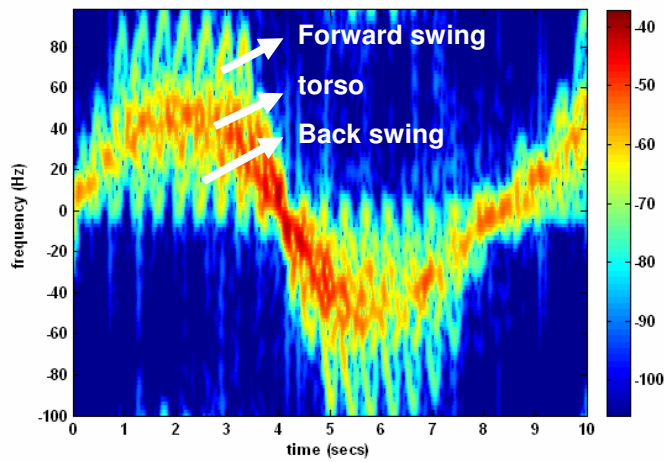
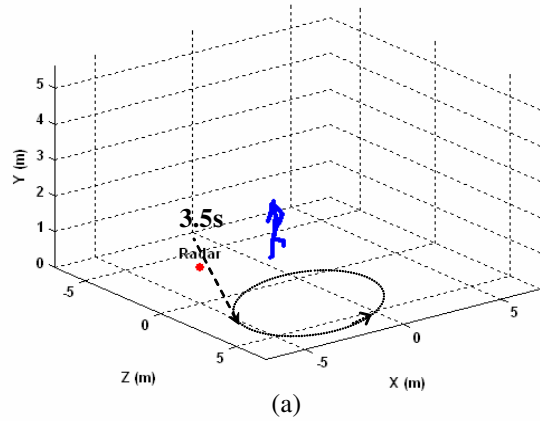


Fig.4.4.(a) Animation model of human running motion from Sony Computer Entertainment America. Doppler spectrogram of human running motion at 2.4 GHz generated from (b) simulation data, (c) measurement data.

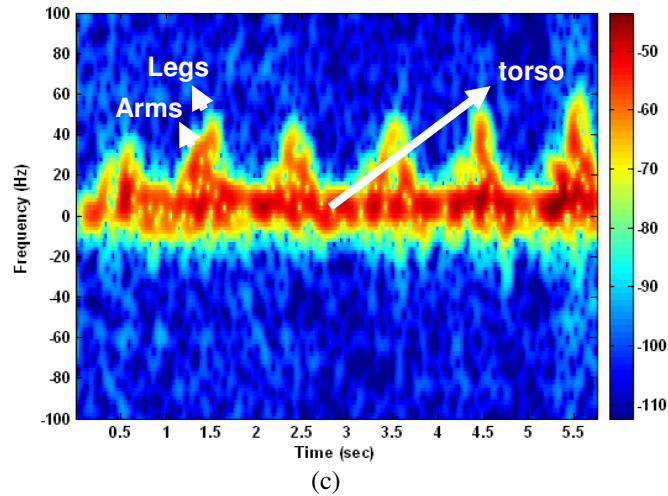
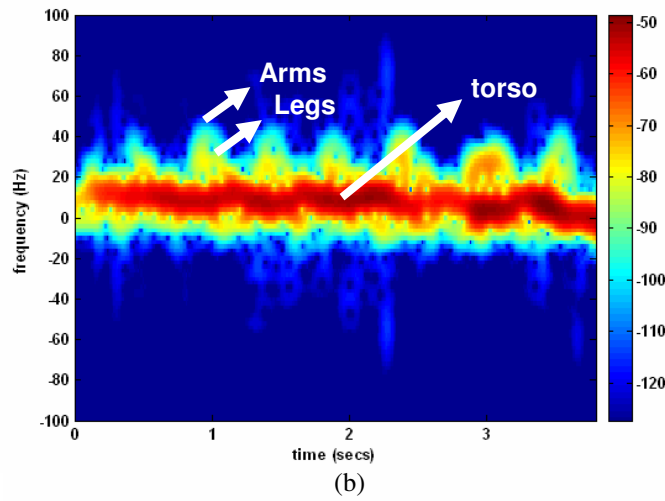
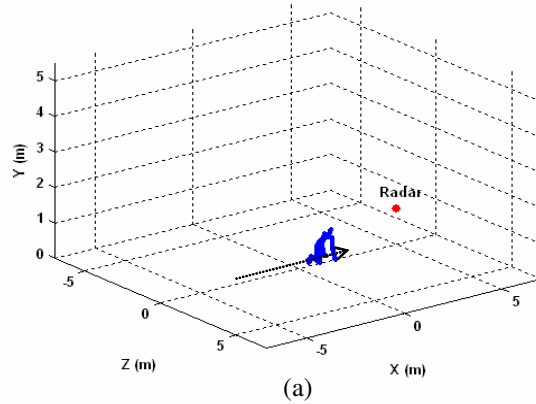
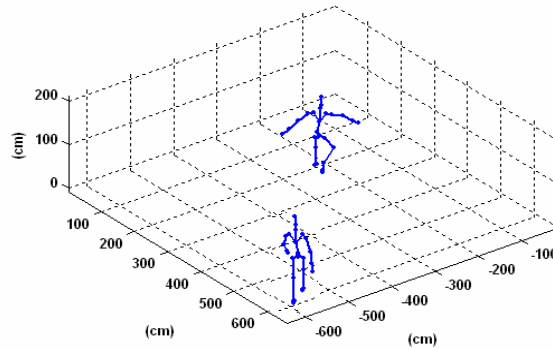
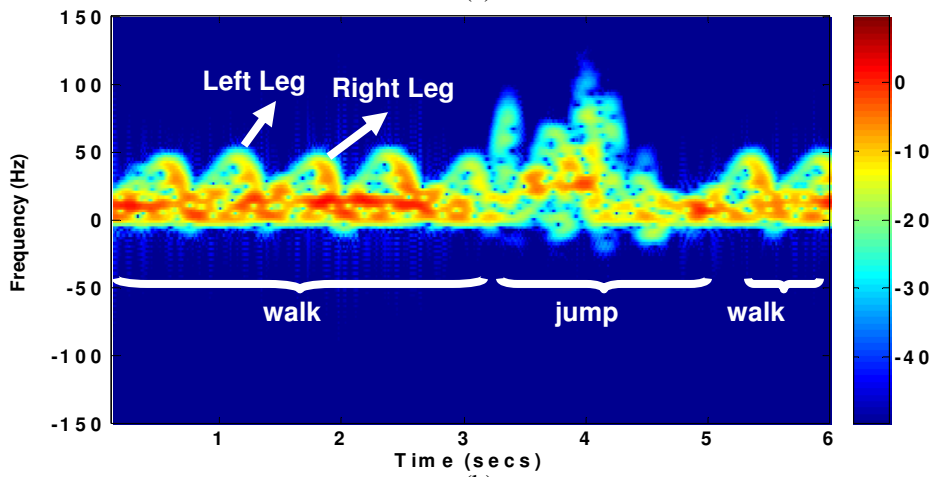


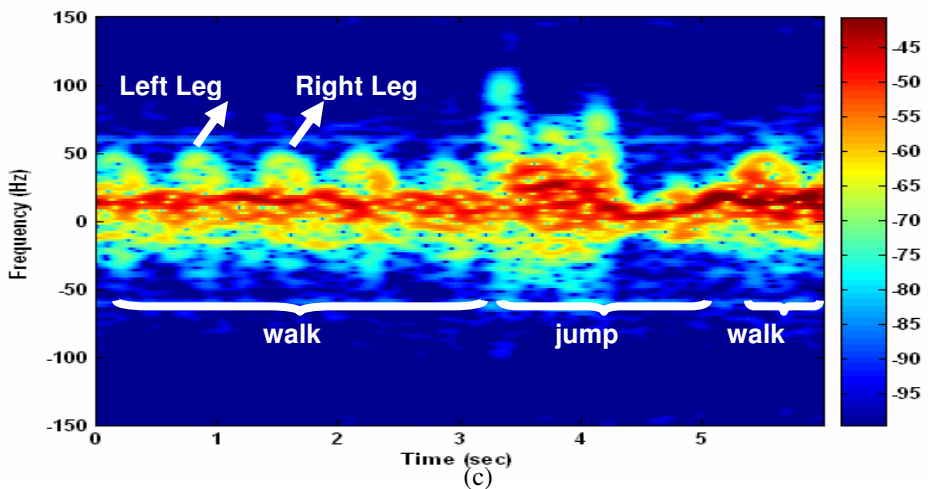
Fig.4.5.(a) Animation model of human crawling motion from CMU Graphics Lab Motion Capture Database. Doppler spectrogram of human crawling motion at 2.4 GHz generated from (b) simulation data, (c) measurement data.



(a)



(b)



(c)

Fig.4.6.(a) Animation model of human walk-jump-walk motion from ACCAD Motion Capture Lab. Doppler spectrogram of human walk-jump-walk motion at 2.4GHz generated from (b) simulation data, (c) measurement data.

4.4.2. Effect of Viewing Angle

The Doppler spectrogram of the human motion is also dependent on the orientation of the mover with respect to the radar. To illustrate this effect, the simulation of the radar returns from the walking motion are repeated for a different position of the radar sensor at (0, 1, 5) m as shown in Fig.4.7a. The resulting Doppler spectrogram is shown in Fig.4.7b. It is observed that the microDoppler returns are much lower in this case due to the low radial components of the velocity vectors. Thus, the effect of transceiver location on the microDoppler signature can be easily studied using the radar simulator. A concept that exploits the multi-view microDoppler information through a network of spatially diverse Doppler sensors for estimating the position and velocity of different point scatterers on the human will be investigated in Chapter 7.

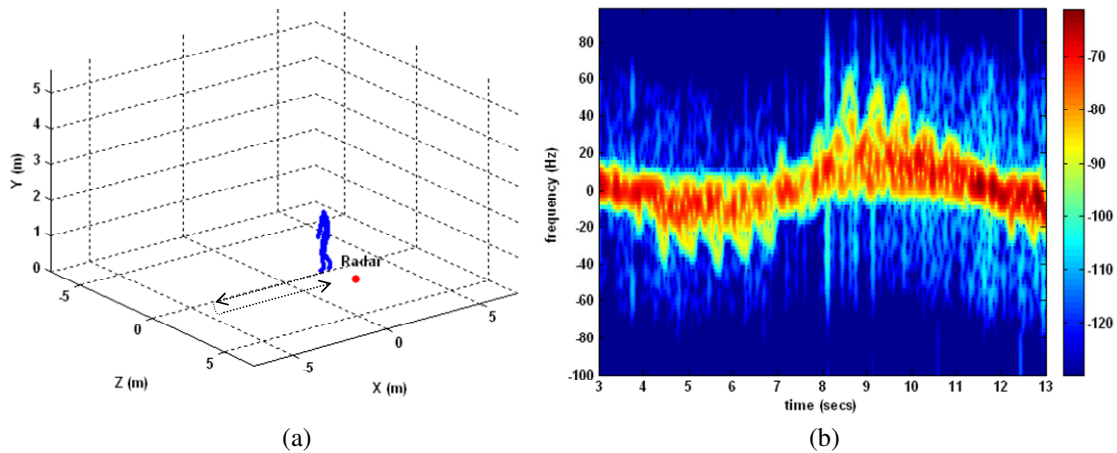


Fig.4.7. (a) Animation model of human walking motion across the radar's field of view. (b) Doppler spectrogram of walking motion at 2.4GHz carrier frequency.

4.4.3. Effect of Carrier Frequency

The simulator can also be used to generate the radar returns of the humans for different carrier frequencies. The simulation of the radar returns from the walking motion is repeated at 12 GHz and a 600Hz sampling frequency. The resulting spectrogram is shown in Fig.4.8. Only a short span (3 seconds) of the spectrogram is shown in the figure. It is observed that due to the higher Doppler sensitivity at 12 GHz, it is possible to discern distinct microDoppler tracks of the different body parts such as the torso, lower arms, lower legs and feet. This spectrogram contrasts with the result at 2.4 GHz shown in Fig.4.3b. The high frequency Doppler radar is thus useful for performing detailed analysis of the human gait.

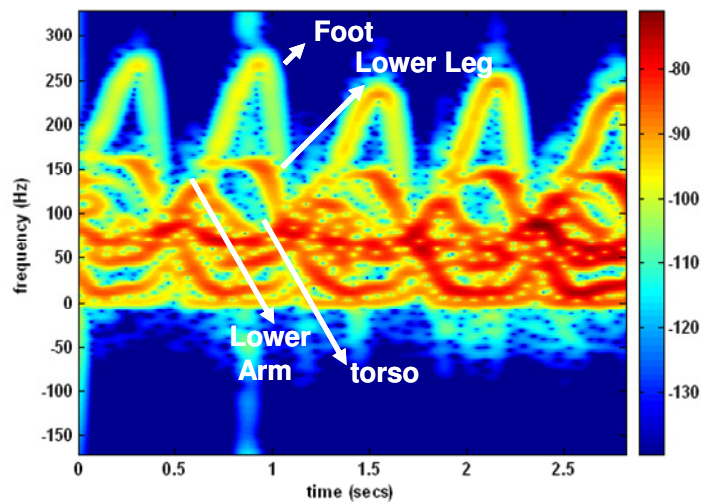


Fig.4.8. Simulated Doppler spectrogram of walking motion at 12GHz

4.4.4. Long Duration Data

The results from Section 4.4.1 indicate that the microDoppler signatures of human motions may be useful for identifying different types of motions. Fig.4.9 shows the

simulated Doppler spectrogram from a one-minute duration BVH file. The specific time intervals from different motions such as accelerated walking, running and slowing down to a halt are marked in the spectrogram. Such data may be analyzed to study motion patterns for use in human activity monitoring over long durations.

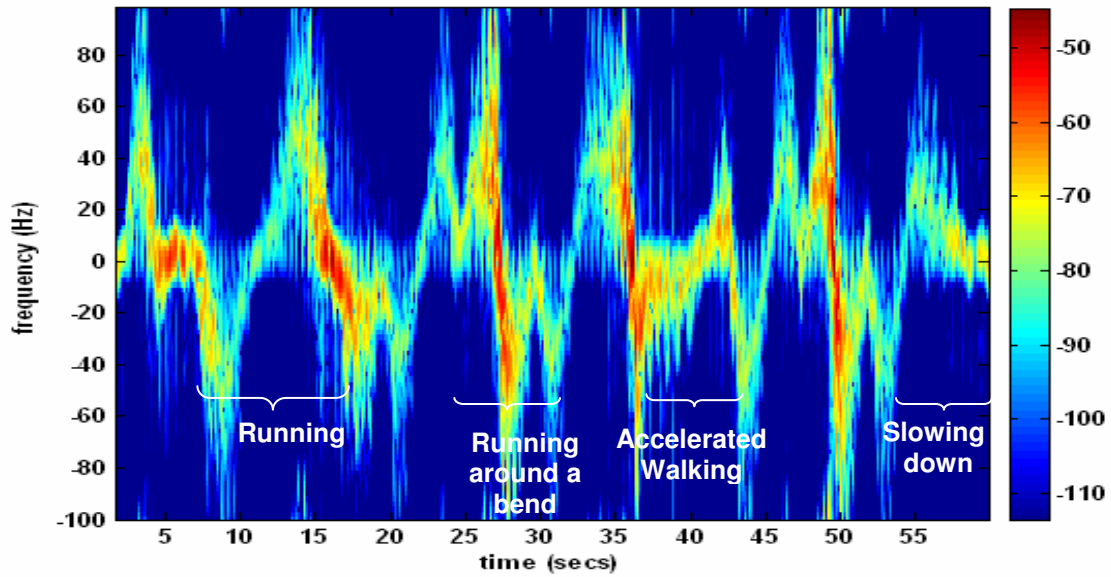


Fig.4.9.Simulated Doppler signatures of human motions over a one-minute duration.

4.4.5. Animal MicroDopplers

The human microDoppler features can be exploited for security monitoring applications such as perimeter control and through-wall tracking. However, one of the key issues is the capability to distinguish humans from other moving bodies particularly animals. It has been reported that the microDoppler signature of a dog differs considerably from that of a walking human [35]. The difference mainly arises due to the difference between the animal quadruped motion and the human biped motion. However,

a detailed analysis of the animal microDoppler has not been carried out. The difficulties lie in procuring animal microDoppler data from radar measurements. However, the radar simulation model described in this section can be easily extended to animals provided animation data of animal motions are available. In this section, the microDoppler spectrograms of a galloping horse and different dog motions such as trotting, running etc are generated from computer animation data and examined.

a. Galloping Horse

First, the simulation procedure is carried out for the animated galloping horse motion obtained from Forge Studios Ltd. The horse gallops at 30mph towards the radar. The data specify the motions of 29 bones in the body of a horse as shown in Fig.4.10a. The horse microDopplers are simulated at a carrier frequency of 2.4GHz, a sampling frequency of 1200 Hz and a dwell time of 0.05s. The resulting spectrogram is shown in Fig.4.10b. Due to the high speed of the horse motion, the Dopplers are much higher than the human walking motion. The RCS of the horse is also significantly higher due to its large size. Also, the Doppler spectrogram of a galloping horse is considerably different from the regular walking motion of a human in Fig.4.3b since the horse's quadruped motion differs significantly from the human biped motion. In order to enhance our understanding of the microDoppler spectrogram of the horse, the different body parts of the horse are studied in isolation in Fig.4.10c through Fig.4.10f. From Fig.4.10c and Fig.4.10d, it is observed that in the galloping motion, the forelegs and rear legs alternate

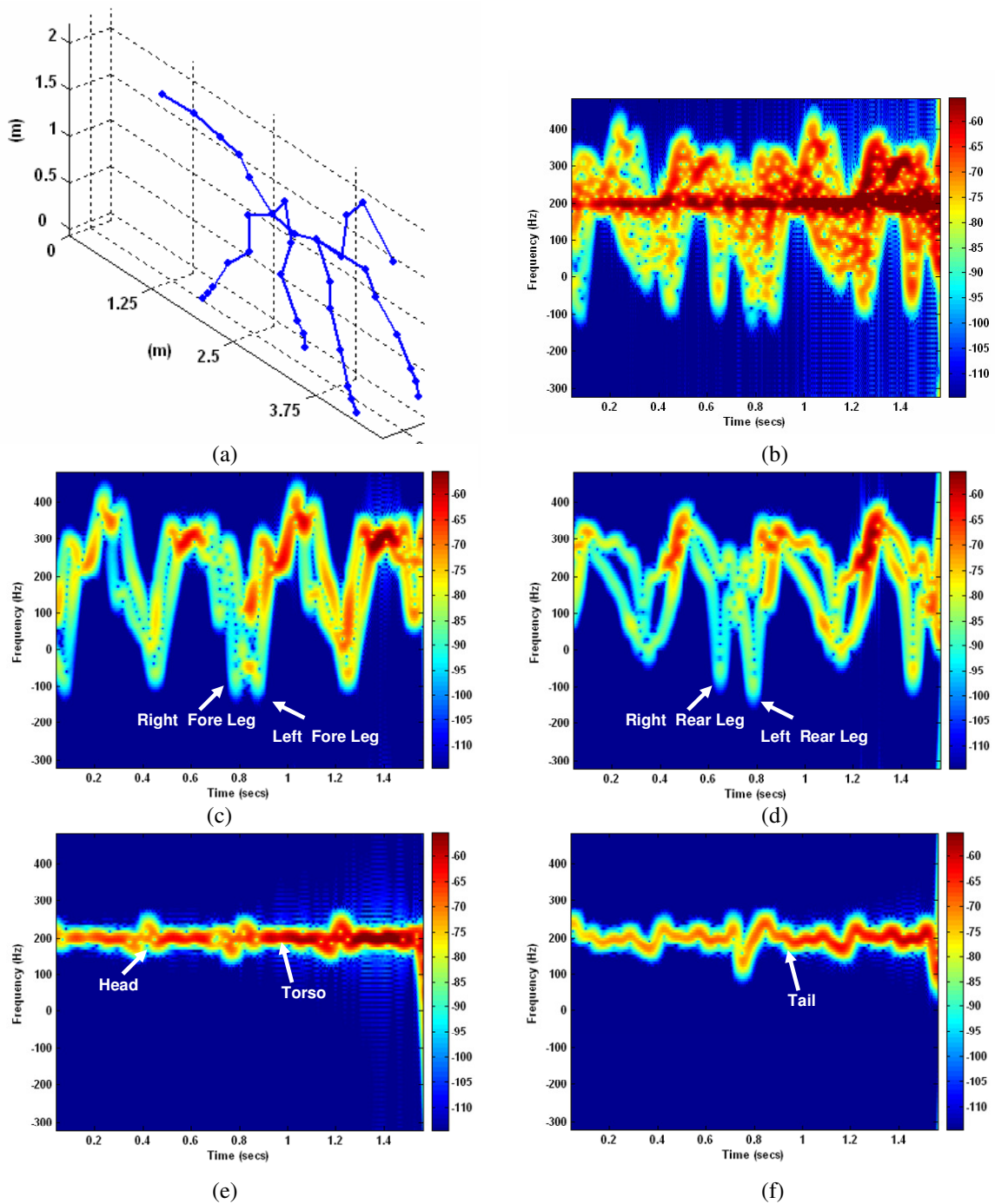


Fig.4.10.(a) Computer animated galloping horse. Doppler spectrogram at 2.4GHz of the motion of: (b) galloping horse, (c) horse's forelegs, (d) horse's rear legs, (e) horse's torso and head and (f) horse's tail.

with each other. Also, the Dopplers of the right legs slightly precede the left legs. The Dopplers from the torso and the head are strong but they show only slight bobbing variation. An additional microDoppler from the tail is also observed.

b. Dog

Next the microDopplers from the motions of a dog are examined. The animation data are obtained from Credo Interactive and shown in Fig.4.11a. The data however do not describe the translation motion of the dog i.e the root joint remains fixed in space. The walking motion of the dog is much slower than the motions of the man and horse. Hence the microDopplers are generated at a carrier frequency of 8 Ghz to obtain improved Doppler resolution in the spectrogram shown in Fig.4.11b. The RCS of the dog is weaker due to its small size compared to the man and horse. The Doppler from the torso is zero since the translation motion of dog was suppressed in the data. In Fig.4.11c and Fig.4.11d, the microDopplers of the forelimbs and rear limbs are shown. It is clearly seen that the Dopplers from the right and left limbs alternate with each other. Also, the microDopplers from the forelimbs appear to be higher than the rear limbs.

Next computer animation data of the motion of the dog transitioning from a run to walk to halt are considered. The corresponding spectrogram is shown in Fig.4.12. The microDopplers over the first 0.5s interval corresponds to the run. Subsequently, from 0.5s to 1s, the microDopplers correspond to walk and finally the dog slows down to a halt and the Dopplers reduce to zero. It is observed that as the motion becomes slower, the Dopplers decrease. Also during the 'run' motion, the

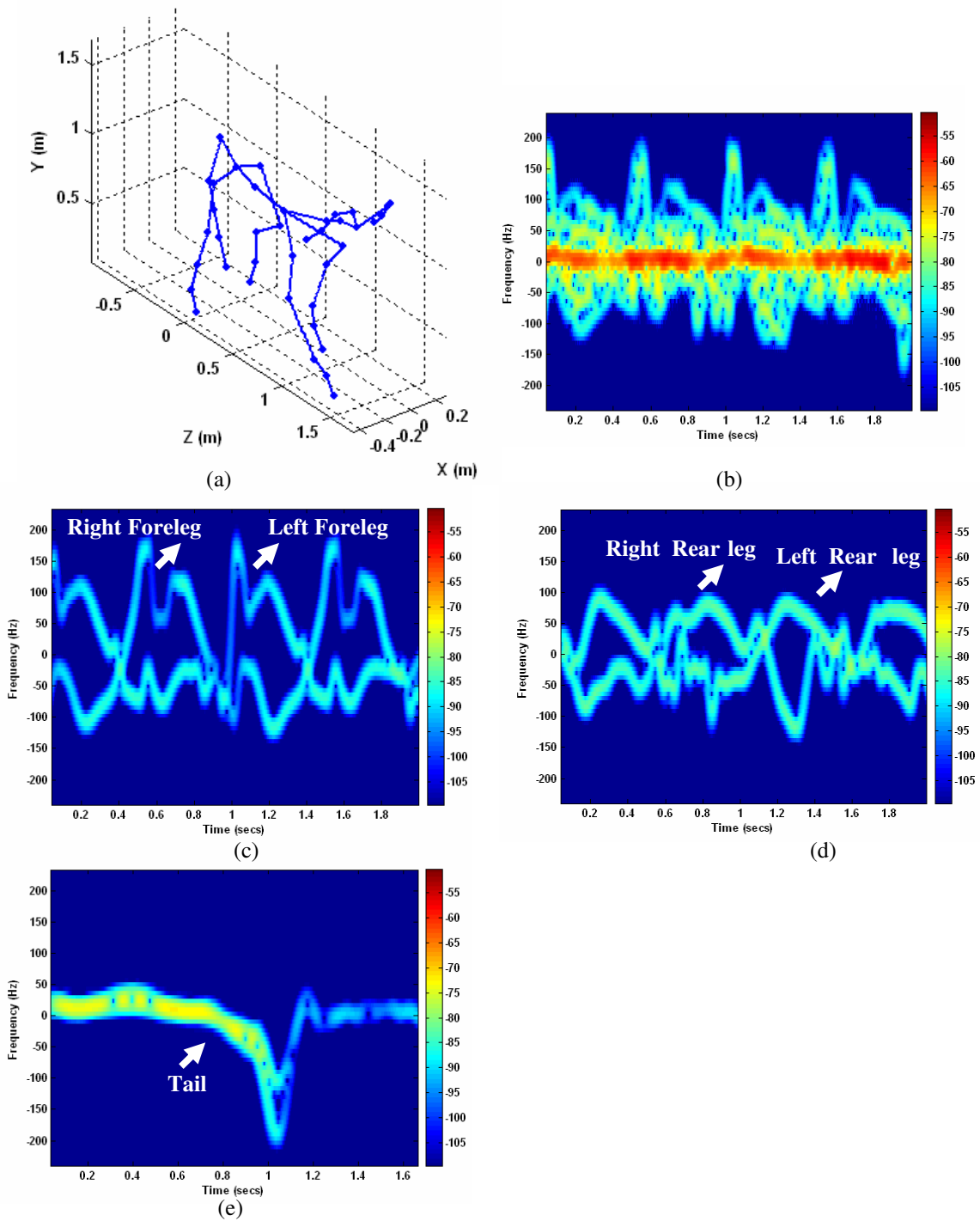


Fig.4.11. (a) Computer animated walking dog. Doppler spectrogram at 8 GHz of the motion of: (b) walking dog, (c) dog's forelegs, (d) dog's rear legs, (e) dog's tail.

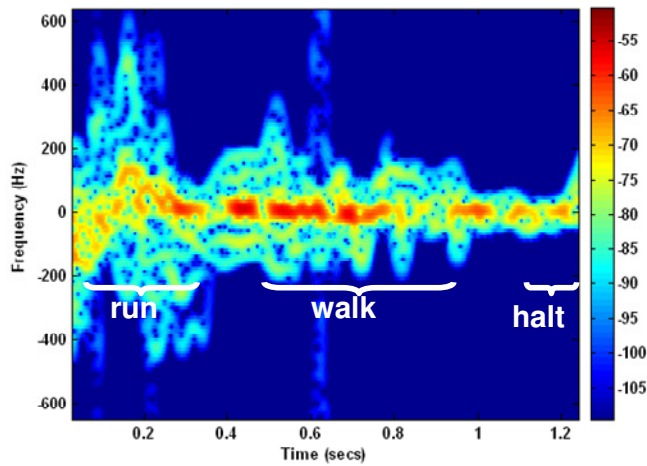


Fig.4.12.Doppler spectrogram of a dog motion transition from “run to walk to halt” generated for 8GHz

the forelimbs and rear limbs of the dog alternate with each other. Thus, quadruped animal spectrograms show distinct microDoppler spectrograms while “walking” (when the right and left limbs alternate with each other similar to human walking motion) and while “running” (when the forelimbs and rear limbs alternate with each other).

The Doppler spectrograms of different animal motions thus show significantly variant microDoppler features and RCS. These spectrograms might potentially be useful as training data for target identification and classification.

4.5. MICRODOPPLER SIGNATURES OF ANOMALOUS HUMAN GAIT

4.5.1. Simulated Spectrograms of Regular and Anomalous Human Gait Patterns

First, the Doppler spectrogram of a normal human gait pattern is simulated using animation data obtained from ACCAD Motion Capture Lab from Ohio State University.

The human walks from (-7,1,7)m to (-3,1,3)m over a duration of 3s and the radar is assumed to be located at (0,1,0)m. The Doppler returns are simulated for a carrier frequency of 12GHz and processed with STFT with a dwell time of 0.1s. The resulting spectrogram, $\chi_r(t,f)$, is shown in Fig.4.13a. Here, the returns from the torso (at 120Hz) and the legs (highest Dopplers) and arms (second highest Dopplers) are observed. Fig.4.13b, shows the Doppler spectrogram, $\chi_{a1}(t,f)$, of a human walking without swinging his arms. All the microDoppler features observed in Fig.4.13a are again observed in this figure except for the microDoppler from the arms. Fig.4.13c, shows the Doppler spectrogram, $\chi_{a2}(t,f)$, of a man carrying a 1.1m long stick in his left hand (Fig.4.13d). The stick is modeled as a metal cylinder, whose RCS is again well characterized [61].

A simple way to deduce the presence of anomalies in the human gait is to compare the spectrograms of the anomalous human gaits $\chi_{a1,2}(t,f)$ with the regular human gait, $\chi_r(t,f)$, spectrogram. This is carried out by generating two types of difference maps: (1): $\chi_r(t,f) - \chi_{a1}(t,f)$ and (2): $\chi_{a2}(t,f) - \chi_r(t,f)$. The first map is generated by subtracting the spectrogram in Fig.4.13b from Fig.4.13a in the decibel scale. The resulting spectrogram in Fig.4.13e indicates that the microDoppler features corresponding to the movements of the arms are absent in $\chi_{a1}(t,f)$. The second map, Fig.4.13f, is generated by subtracting the spectrogram in Fig.4.13a from Fig.4.13c. It shows the additional microDoppler feature present in $\chi_{a2}(t,f)$, which arises from the motion of the metal stick. Thus microDoppler features arising from anomalies in the human gait are identified in the Doppler spectrograms. Next, this concept is verified using measurement data.

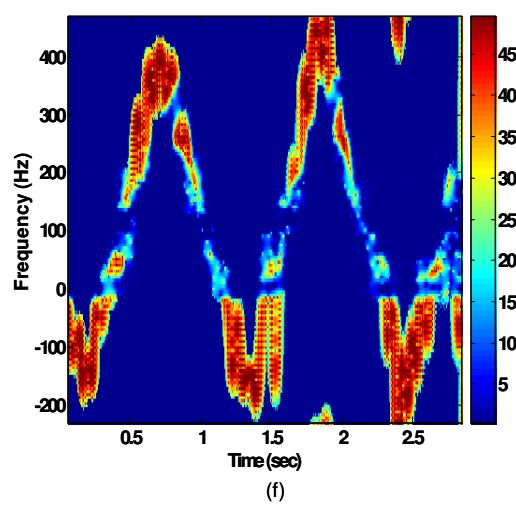
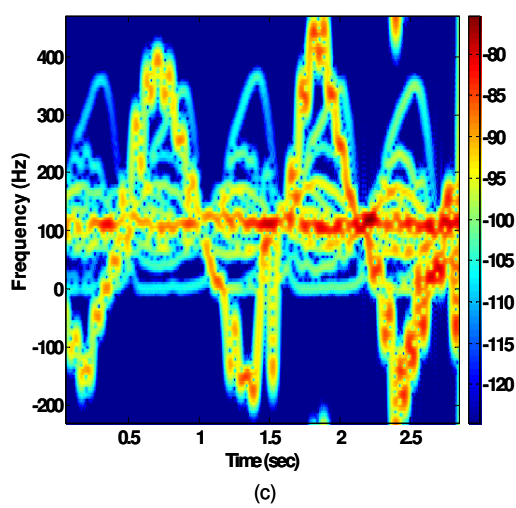
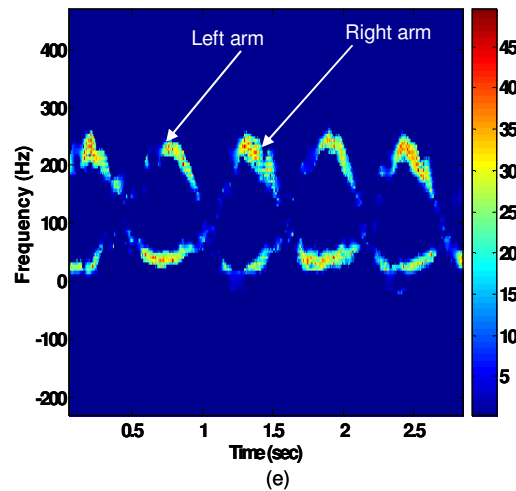
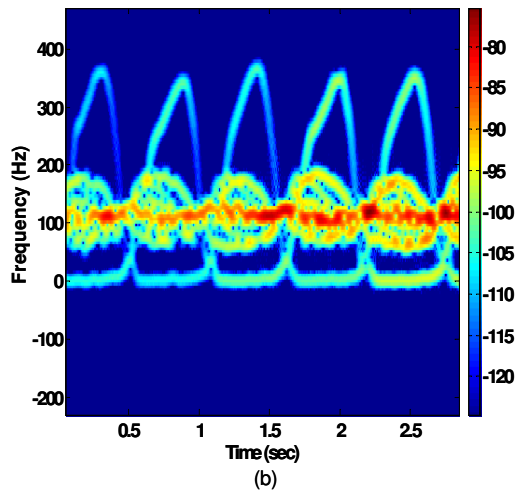
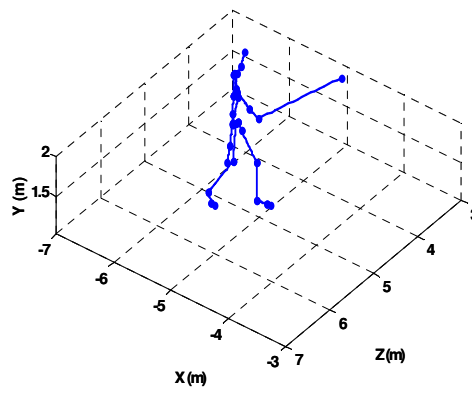
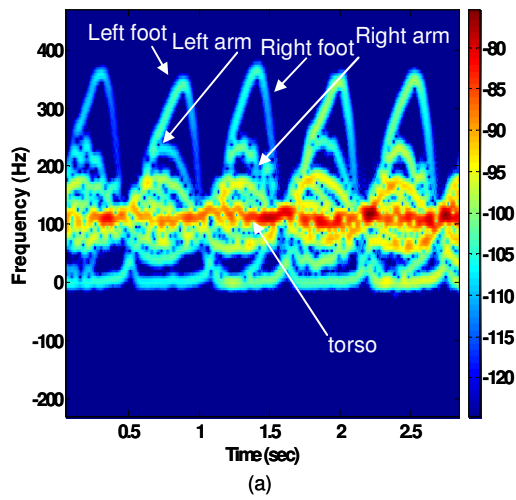


Fig.4.13. Caption follows.

Fig.4.13. Simulated spectrogram at 12GHz of (a) regular human gait, $\chi_r(t,f)$. (b) human walking without swinging the arms, $\chi_{a1}(t,f)$, (c) human walking while carrying a 1.1m metal stick in the left arm, $\chi_{a2}(t,f)$. (d) Computer animation data of the human carrying the stick used to simulate **Fig.4.13**(c). (e) $\chi_r(t,f) - \chi_{a1}(t,f)$ shows the missing microDoppler features in **Fig.4.13**(b) due to human arm motions. (f) $\chi_{a2}(t,f) - \chi_r(t,f)$ shows the additional microDoppler feature in **Fig.4.13**(c) due to the metal stick.

4.5.2. Measured Spectrograms of Regular and Anomalous Human Gait Patterns

In Chapter 3, Section 3.3.4, the reassigned spectrograms of some deviated human gait generated from measurement data collected using the Doppler radar testbed were examined. In this section, the STFT spectrograms of the same measurement data are considered over a 6s duration. In the first case, the human subject undergoes a regular walking motion. The spectrogram, $\chi_r(t,f)$, is shown in Fig.4.14a. wherein the microDopplers from the movements of the torso, arms and legs are visible. In the second case, the human subject walks while carrying a heavy metal box in his left hand. This results in the left arm and leg not swinging as freely as the right arm and leg. This situation is reflected in the Doppler spectrogram, $\chi_{a1}(t,f)$, shown in Fig.4.14b. Next, the human subject repeats the walking motion while carrying a long metallic pole in his left hand. The motion of the human subject carrying this long pole differs significantly from the computer animated motion of the human carrying a metal stick in the previous section. Here, the pole is used like a walking stick. The resulting spectrogram, $\chi_{a2}(t,f)$, is

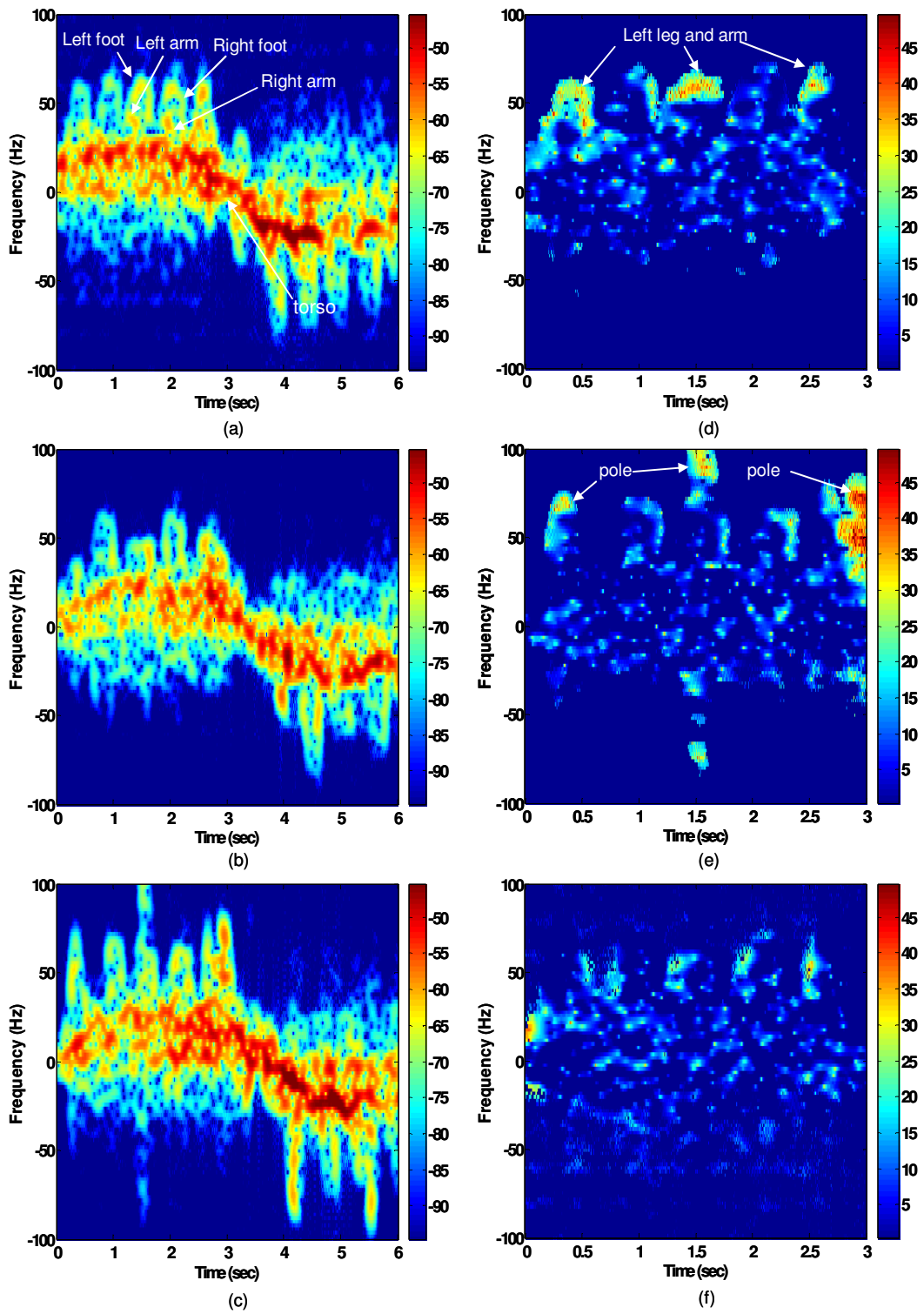


Fig. 4.14. Caption follows.

Fig.4.14. Measured spectrogram at 2.4GHz of (a) regular human walking gait, $\chi_r(t,f)$, (b) human walking while carrying a heavy tool box in the left hand, $\chi_{a1}(t,f)$, (c) human walking with a long metal pole in the left hand, $\chi_{a2}(t,f)$. (d) $\chi_r(t,f) - \chi_{a1}(t,f)$ shows the missing microDoppler features in **Fig.4.13(b)** due to motions of the left arm and leg. (e) $\chi_{a2}(t,f) - \chi_r(t,f)$ shows the additional microDoppler feature in **Fig.4.13(c)** from the metal pole. (f) $\chi_r(t,f) - \chi_{a2}(t,f)$ shows the missing microDoppler features in **Fig.4.13(c)** due possibly to shadowing by the metal pole.

shown in Fig.4.14c. A difference map is generated from $\chi_r(t,f) - \chi_{a1}(t,f)$ and shown in Fig.4.14d. The figure focuses on the first 3s of data where the spectrograms in Fig.4.14a and Fig.4.14b are well aligned along the time axis. Here, some microDoppler features are observed at time instants (0.2 – 0.6)s, (1.2 – 1.7)s and (2.4 – 2.7)s corresponding to the movements of the left arm and leg. The figure clearly indicates the missing microDoppler features from the limited motion of the left limbs in the second measurement case. Next, Fig.4.14e is generated from $\chi_{a2}(t,f) - \chi_r(t,f)$. Here, the microDoppler feature from the pole is clearly observed at time instants (0.2 – 0.5)s, (1.4 – 1.5)s and (2.7 – 3)s. The results from Fig.4.14d and Fig.4.14e are qualitatively similar to the findings from the simulation data. Additionally, a difference map is generated from $\chi_r(t,f) - \chi_{a2}(t,f)$. The non-negligible energy observed in Fig.4.14f indicates that there are also some missing features in the walking-with-pole data from the normal gait data. This could be due to the shadowing of human body parts by the metal pole. This phenomenon was not observed in the simulation data since the simulation ignored mutual shadowing between body parts.

The spectrograms generated from simulation and measurement data indicate that some anomalies in the human gait can be discerned from the Doppler spectrograms of

human gait. Features extracted from the data may be useful for identifying various anomalies.

4.6. CONCLUSION

A Doppler radar simulator of complex human motions is implemented using a primitive based electromagnetic predictor in conjunction with computer animation data. The primitive based modeling of humans is validated by simultaneously generating radar data and MOCAP data of complex human motions. Then spectrograms of different human motions such as walking, running, crawling and jumping are generated using virtual reality data and are compared against measured data obtained in the laboratory. Additional simulation data are generated to study the effect of frequency and viewing angle. In the subsequent chapter, the simulator will be combined with a model of through-wall wave propagation to provide us with the capability to study detailed the detailed phenomenology of human radar returns.

5. Simulation of Wall Effects on Human Signatures

5.1. INTRODUCTION

In the previous chapter, a technique for simulating the radar returns from humans moving in free space was presented. However, in reality, the propagation environment between the human and radar may be quite complex and may introduce significant distortions to the radar returns. Walls, in particular, are very complex media for wave propagation that introduce considerable distortions such as attenuation, delay and multipath to the radar returns [30]. The effect of walls on the dynamic human radar returns (in particular Doppler radar returns) have not been adequately studied by the radar community. The main reason is the lack of a simulation model that combined human motion scattering mechanisms with through-wall wave propagation physics.

In this chapter, a technique for simulating time-varying narrowband and wideband radar returns of human motions behind both homogeneous and inhomogeneous walls is devised. This technique combines primitive based modeling of humans described in the last chapter with wall simulation models generated using the finite-difference time-domain (FDTD) technique. Both the human microDoppler signatures and the high range-resolution profiles can be readily generated of a moving human behind a wall using this approach. The simulation results enable the investigation of the effects of complex walls on human microDopplers and range profiles. The narrowband results are validated with the measured data collected in line-of-sight and through-wall scenarios using the Doppler

radar testbed. The findings are further supplemented with an analytical study of the effect of wall refraction and multipath introduced by wall inhomogeneity on the Dopplers of a point target moving behind walls.

5.2. FDTD SIMULATIONS OF DIFFERENT WALLS

In [30],[44]-[47], simple homogeneous walls made of concrete, wood or adobe were characterized using ray optical techniques. However, their utility for modeling highly inhomogeneous walls such as reinforced concrete walls and cinderblock walls is suspect [47]. A full wave electromagnetic solver is required to accurately model the wave propagation through such complex walls. Hence, independent of the human simulation model described in the last chapter, the through-wall wave propagation phenomenology is simulated using a finite-difference time-domain technique (FDTD) [43]. FDTD is a computational electromagnetic technique where time-dependent Maxwell's equations are solved by replacing them with finite difference equations. Once the time domain data are simulated, the frequency transfer function can be obtained by the Fourier transform. The transfer functions are generated for free space and for three different walls. The three walls are:

- (1) a homogeneous concrete wall with a dielectric constant of 7 and conductivity 0.0498 S/m,
- (2) a reinforced concrete wall, with a dielectric constant of 7 and conductivity 0.0498 S/m, reinforced by square metal conductors that are 2.25cm thick and 19.75cm apart and

(3) an inhomogeneous cinderblock wall with air holes as shown in Fig.5.1.

The dimensions of each wall is $1m \times 19.5cm$ ($X: -0.5m$ to $0.5m$, $Y: 0.3m$ to $0.495m$). To reduce the computational cost of the problem, the simulation is limited to two-dimensions (i.e., assuming the problem is Z -invariant). The area of the simulation is a $1.0m \times 1.5m$ space ($X: -0.5m$ to $0.5m$, $Y: 0m$ to $1.5m$) bounded by a perfectly matched layer (PML). A pulse source of $0.23ns$ duration and vertically polarized in the Z -direction is placed at the position $(0m, 0.1m)$, $0.2m$ behind the wall which is $1m$ wide in X and $19.5cm$ thick along Y . The simulator is run long enough to allow the wave fronts from the multiple bounces within the wall to reach the end of the simulation space. The time-domain electric field at every point ρ in the FDTD grid space is then fast Fourier transformed to derive the wall transmission response, $H_{wall}(f_c, \rho)$, as a function of frequency and observation position.

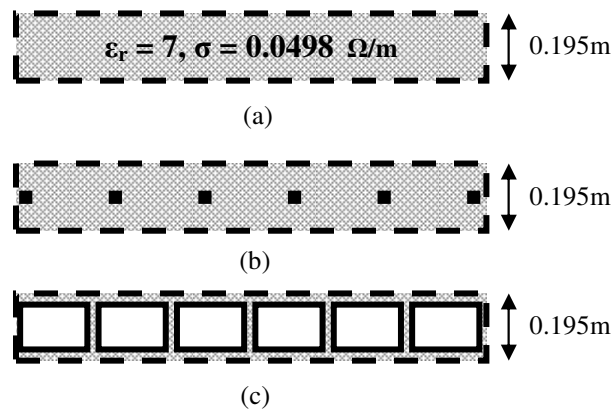


Fig.5.1. Models of 3 different types of walls for FDTD simulations: (a) homogeneous wall, (b) reinforced concrete wall and (c) cinderblock wall.

The magnitude responses for the three walls at $2.4GHz$ are shown in Fig.5.2a through Fig.5.2d. Fig.5.2a shows the magnitude response for free space (without the

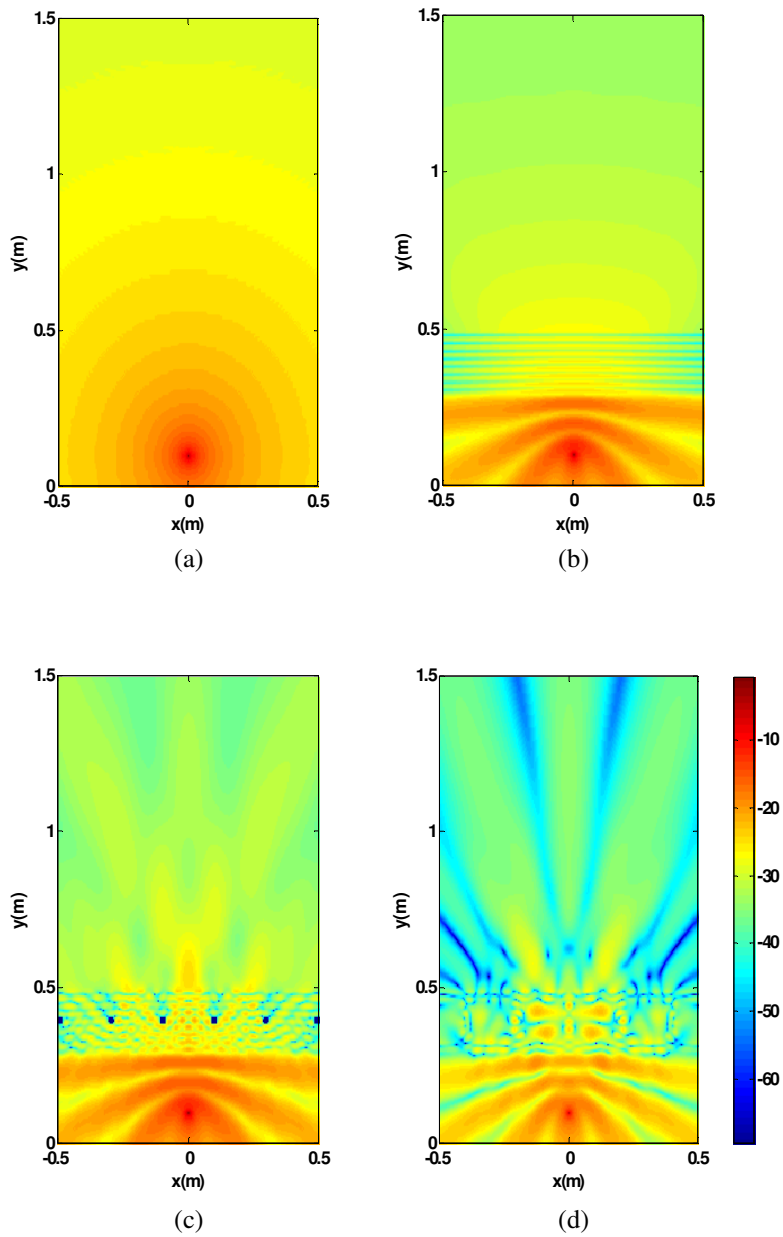


Fig.5.2. Results from FDTD simulations: Magnitude response at 2.4GHz for (a) free space, (b) homogeneous concrete wall, (c) reinforced concrete wall and (d) cinderblock wall.

wall) for a carrier frequency of 2.4GHz. The magnitude response shows the electric field strength decaying as the distance from the source increases. Fig.5.2b shows the magnitude response for the simulation space with the presence of a homogeneous

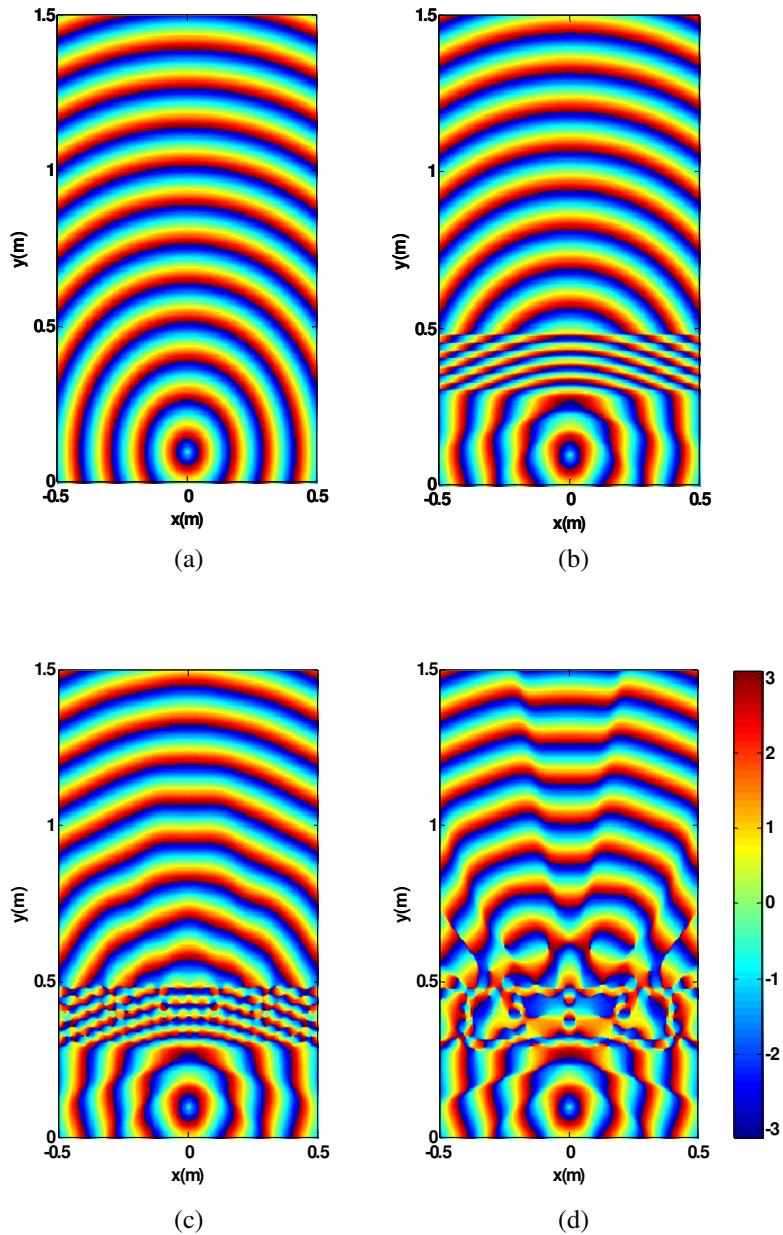


Fig.5.3. Results from FDTD simulations: Phase response at 2.4GHz for (a) free space, (b) homogeneous concrete wall, (c) reinforced concrete wall and (d) cinderblock wall.

concrete wall. The strength of the electric field again decays as the distance from the pulse source increases. The wall, however, introduces an attenuation of approximately 15dB when compared to free space. Also, the magnitude response shows some directionality due to the angle dependent transmission. In the magnitude response of the reinforced concrete wall case in Fig.5.2c, the wall introduces significant attenuation of the order of 2-10 dB. Also, the multiple scattering introduced by the metal reinforcements inside the wall interfere destructively in some regions. Fig.5.2d shows the magnitude response for the cinderblock wall. Again, the wall introduces significant attenuation on the transmitted signal. Moreover, the interior wall inhomogeneity introduces multipath components that interfere severely in certain regions (for instance, at azimuth angles of 55° and 83°).

Fig.5.3a through Fig.5.3d show the phase responses for free space and the three walls at 2.4GHz. In Fig.5.3a, for the free space case, the phase response shows a regular circular spread. In Fig.5.3b, it is observed that beyond the homogeneous wall ($Y: 0.5m$ to $1.5m$), the transmitted wave front remains a well behaved circular wave front throughout the simulation space. This is very similar to the phase response that appears for a wave propagating in free space. However, when the reinforced concrete wall and the cinderblock walls are considered in Fig.5.3c and Fig.5.3d respectively, the complex wave fronts from the multiple reverberations within the wall give rise to significant phase distortions. These are especially severe near the wall.

5.3. HYBRID MODEL OF HUMAN AND WALL SIMULATIONS

Next, the wall transfer function derived from FDTD is combined with the human scattering returns simulated from the animation models. If any higher order interactions between the human and the wall are ignored, this hybridization is quite simple. In principle, it is carried out by substituting the two-way free-space propagation factor between the radar and the phase center of each human body primitive, $(e^{-j\frac{2\pi f_c}{c}2r_b}/r_b^2)$, by the square of the complex wall transfer function, $\{H_{wall}[f_c, \mathbf{r}_b]\}^2$. Though the operation appears straightforward, the following steps are followed to effectively hybridize the human and wall simulation models.

First, since the animation data are available at a frame rate of 120 Hz, the data must be suitably interpolated in time to prevent aliasing in the Doppler domain, especially if a high carrier frequency is used since the Doppler frequency is directly proportional to the carrier. In this work, the data are interpolated using spherical linear interpolation techniques.

Next, the wall transfer functions from the two-dimensional FDTD simulation must be rescaled so as to correspond to the desired 3-D modeling. First, it is noted that the 2-D incident field due to a line source in free space is given by:

$$E_i(\rho) = \frac{A'}{\sqrt{\rho}} e^{-j\frac{2\pi f_c}{c}\rho} \quad (5.1)$$

where A' is a constant proportional to the current excitation used to drive the FDTD. Therefore, to translate the 2-D FDTD modeling into three dimensions, the wall transfer function, $H_{wall}[f_c, \boldsymbol{\rho}]$, from the FDTD is rescaled by the factor

$$C_{2D \rightarrow 3D} = \left(\frac{\sqrt{\rho}}{r} \right) \left(\frac{1}{A'} \right) e^{-j \frac{2\pi f_c}{c} (r - \rho)} \quad (5.2).$$

The rescaling is derived from free-space considerations, but is carried out for the wall transfer function at every point $\boldsymbol{\rho}$. Third, it is also noted that the FDTD simulation generates the wall transfer coefficients only at the FDTD grid positions. Hence, a bilinear interpolation is carried out to compute, $H_{wall}[f_c, \boldsymbol{\rho}_b]$ more accurately where $\boldsymbol{\rho}_b(t)$ is the time-varying position coordinate of the bone primitive, $\boldsymbol{r}_b(t)$, projected onto the two-dimensional FDTD simulation space.

Finally, the scattered returns of the human behind the wall are generated using,

$$E_s(t) = \frac{A}{\sqrt{4\pi}} \sum_{b=1}^N \sqrt{\sigma_b(t)} \{ C_{2D \rightarrow 3D} H_{wall}[f_c, \boldsymbol{\rho}_b(t)] \}^2 \quad (5.3)$$

To summarize, a hybrid methodology is presented to combine the dynamic human signature predicted from a primitive model with the wall propagation effects computed from FDTD simulations.

5.4. MICRODOPPLERS FROM A HUMAN WALKING BEHIND A WALL

Using the methodology describe in the previous section, both narrowband, $E_s(t, f_{co})$ and wideband, $E_s(t, f_c)$, scattered returns from a human moving behind a wall can be

generated. In this section, the effects of walls on human microDopplers generated from the narrowband returns are investigated.

5.4.1. Simulation Results

A human walking motion from the Sony Computer Entertainment America's animation database is used. The animation data provided at a fixed frame rate of 120Hz.

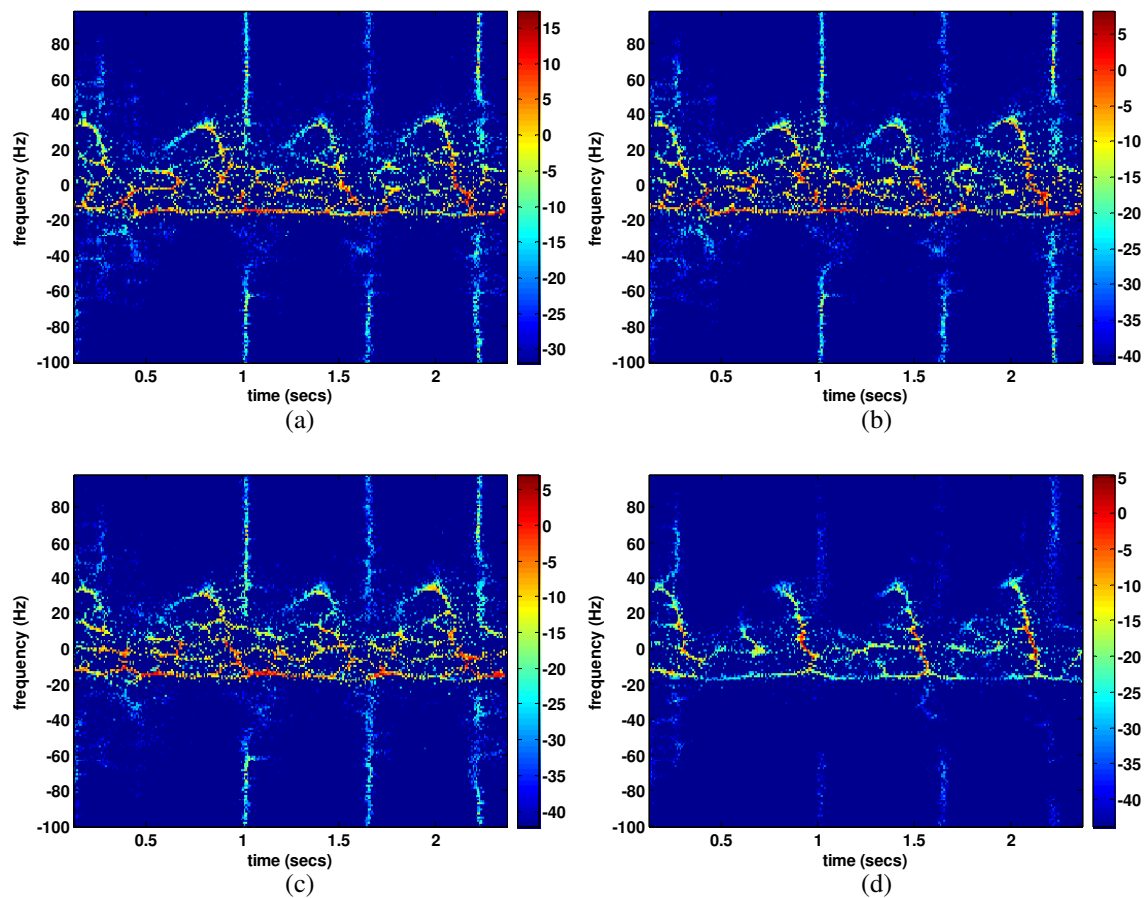


Fig.5.4. Results of simulations of human and wall: Reassigned Doppler spectrogram of walking human at 2.4GHz for (a) free space, (b) homogeneous wall, (c) reinforced concrete wall and (d) cinderblock wall.

are interpolated to 200Hz to provide sufficient Doppler bandwidth to avoid aliasing effects. In order to ensure that the human motion is confined to the FDTD simulation space, the translation movement of the human is removed from the model by fixing the human hip joint at the position $(0m, 1m, 1m)$. The time domain radar returns are simulated for a carrier frequency of 2.4GHz. Instead of generating the Doppler spectrogram by the application of the STFT on the time-domain radar returns, the reassigned transform described in Chapter 3 is used to obtain improved signal localization in the spectrogram.

Fig.5.4a through Fig.5.4d show the reassigned Doppler spectrograms that are generated when the human motion model is combined with the FDTD results for free space and the three wall cases. The free-space result in Fig.5.4a is first checked against a theoretical result obtained using equation (5.2) and the two spectrograms match very well. In Fig.5.4a, the Doppler of the torso is observed to be zero because of the zero translation motion of the human. The periodic features in the spectrogram arise due to the alternating motions of the left and right limbs. The feet returns have the highest Dopplers followed by the lower legs and lower arms. The vertical streaks observed in the spectrogram are caused by short, jerky movements in the computer animated human. Fig.5.4b shows the reassigned Doppler spectrogram that results when the human moves behind the homogeneous concrete wall. Except for a 15dB attenuation introduced by the wall at 2.4GHz, there appears very little distortion in the Doppler spectrogram when compared with that of free space. Next the reinforced concrete wall case is considered in Fig.5.4c. Besides attenuation caused by the wall, the metal reinforcements introduce considerable multipath in the propagation channel. The interference between these

multipath components results in fades and peaks in the area of simulation. This causes the strength of some of the microDopplers to change. However, the actual values of the microDoppler frequencies appear to remain unchanged. The inhomogeneous cinderblock wall case is considered in Fig.5.4d. Some of the microDoppler features are now faded due to the severe attenuation introduced in some regions of space by the interfering multipath components. However, the actual values of the microDoppler frequencies appear to remain unchanged.

5.4.2. Measurement Results

The simulation results showed that the magnitude response of a wall was responsible for the key differences observed between the Doppler spectrograms of the free-space and through-wall cases. The actual microDoppler frequencies did not significantly change even in the presence of a complex, inhomogeneous wall. To corroborate the simulation results, measurement data is collected using the 2.4 GHz Doppler radar. First, the measurement is carried out under an indoor, line-of-sight condition where the human subject walks towards the radar from 10m to 4m and then turns around and walks away from the radar. Due to measurement noise, the reassigned spectrogram is not as effective in dealing with measured data, and the standard STFT is again used to display the data. The Doppler spectrogram is shown in Fig.5.5a. The spectrogram shows the same features observed previously in the simulated reassigned spectrogram in Fig.5.4a, such as the periodic features that arise due to alternating motions

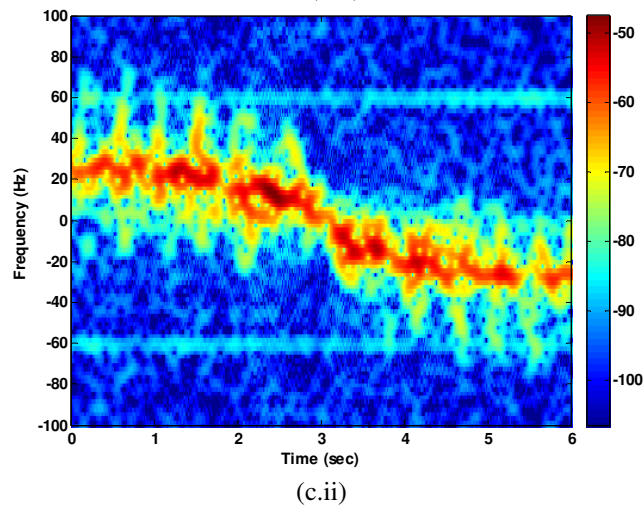
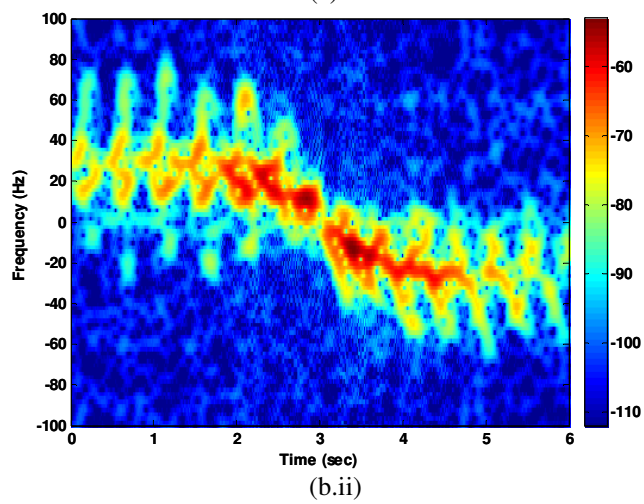
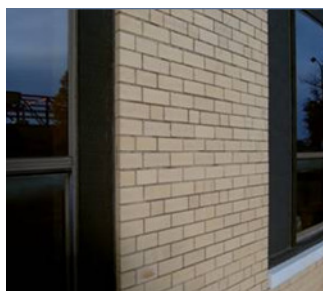
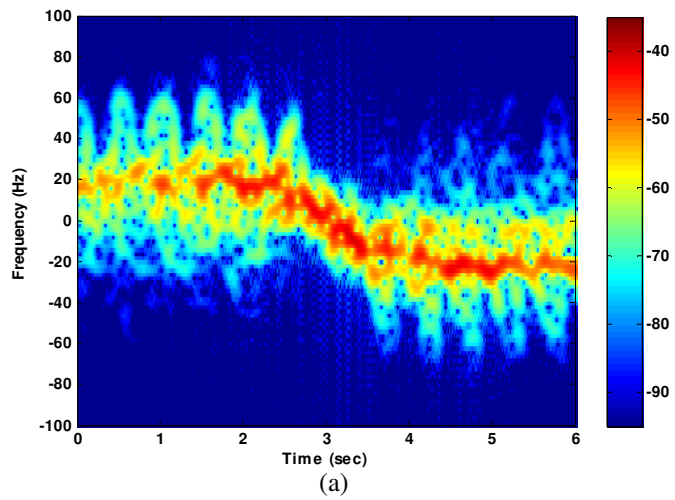


Fig. 5.5. Caption follows.

Fig.5.5. Doppler spectrogram generated from measurement data collected using the Doppler radar testbed at 2.4GHz for (a) indoor line of sight, (b) through exterior 15” brick wall and (c) 12” cinderblock wall.

of the limbs. In the measurement case though, the Doppler of the torso is not zero, unlike the simulation case where the translational motion was suppressed. Next, the measurement is repeated with the human subject behind an exterior brick wall (Fig.5.5b.i) of 15” thickness. From Fig.5.5b.ii, it is observed that the Doppler features are still preserved in this case, in spite of the lowered signal strength caused by the wall attenuation. In the third case, the measurement is conducted with the subject behind a cinderblock wall of 12” thickness (Fig.5.5c.i). The resulting Doppler spectrogram is shown in Fig.5.5c.ii. In both of the through-wall cases the subject walks from 6.8m to 1.8m behind the wall and the radar is placed 0.1m in front of the wall. From the observations of the measurement results, it seems safe to suggest that walls do not seem to significantly alter the microDoppler frequencies of humans. To quantitatively substantiate this observation, the effects of walls on the Doppler of a single point scatterer are examined in greater detail from an analysis viewpoint next.

5.5. QUANTITATIVE ANALYSIS OF WALL EFFECTS

A theoretical study of the effect of a wall on the Doppler return of a single point scatterer is carried out. First, the effect of wave refraction caused by the wall is examined. Next, the effect of multipaths introduced by more complex walls is investigated using FDTD simulation.

5.5.1. Refraction

A homogeneous wall of thickness d and a monostatic radar setup is assumed as shown in Fig.5.6a. The point scatterer, at a position (x, y) with respect to the radar, moves with a velocity v_r , along the radial direction towards the radar. In the absence of a wall, the Doppler frequency of the point scatterer is $2f_c(v_r / c)$. When a wall of high permittivity is present, the wave gets refracted as shown in the figure (where the angle of refraction approaches zero under the high permittivity assumption). If the multiple bounces of the wave within the wall are ignored, the Doppler of the point scatterer is $2f_c(v_r / c) \cos \theta$ where θ is the angle between the direct wave and the refracted wave. Thus the difference in Dopplers in the two cases is directly proportional to $(\cos \theta - 1)$ where

$$\cos \theta = \cos \left[\tan^{-1} \left(\frac{x}{y-d} \right) - \tan^{-1} \left(\frac{x}{y} \right) \right] \quad (5.4)$$

Assuming that the simulation space extends from $X: 0m$ to $3m$ and $Y: 0.5m$ to $3m$ and that the wall is 19.5cm thick, the resulting cosine plot is shown in Fig.5.6b. It is observed that for most of the space, $\cos \theta$ is very close to 1 except for the small region in blue where the change is still less than 5.5%. If the point scatterer moves tangentially with respect to the radar with a velocity v_t , the Doppler of the point scatterer behind the wall becomes $2f_c(v_t / c) \sin \theta$ instead of 0. Though the plot is not shown, $\sin \theta$ was found to be very close to 0 for most of the simulation space (less than 0.06). The results

of this study illustrates that the Doppler frequency does not change significantly due to wall refraction.

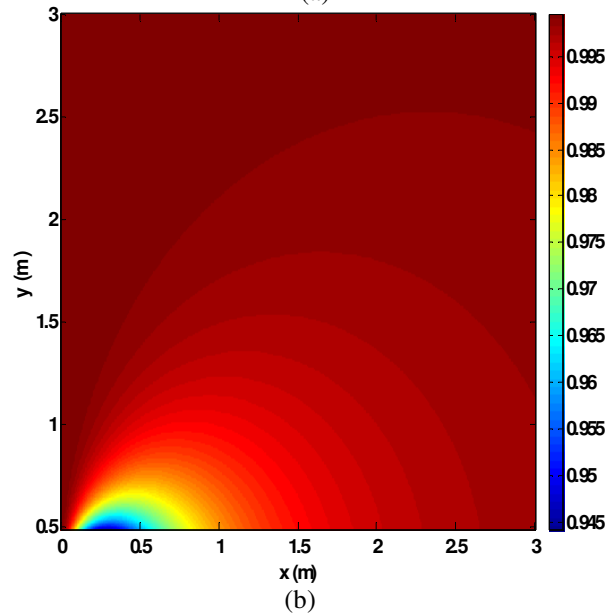
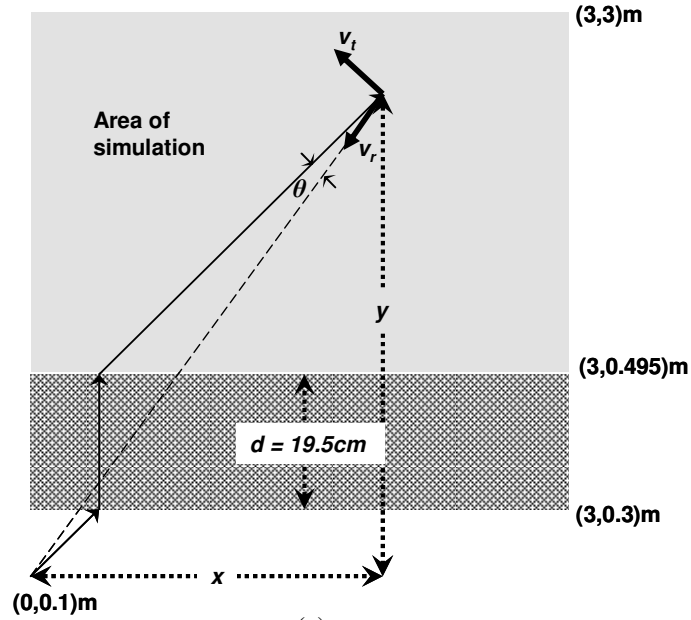


Fig.5.6. Derivation of effect of wall refraction on the Doppler of a point scatterer (a) Simulation set up (b) $\cos \theta$.

5.5.2. Multiple Bounces

Next, the effect of all the multiple bounces within a wall on the Doppler of a single point scatterer is considered. A point scatterer is assumed to be at a position (x, y) in the FDTD grid space moving with a radial velocity, v_r , towards the radar. Then the instantaneous Doppler at every point (i,j) in the grid can be derived from the rate of change of phase, φ , by the finite-difference formula

$$f_{i,j} = \frac{v_r}{\pi} \left[\frac{\varphi_{i+1,j} - \varphi_{i,j}}{2\Delta x} \cos \alpha_{i,j} + \frac{\varphi_{i,j+1} - \varphi_{i,j-1}}{2\Delta y} \sin \alpha_{i,j} \right] \quad (5.5)$$

where $\alpha_{i,j}$ is the angle between the velocity vector of the point scatterer and the X axis. A purely radial motion is assumed for the point scatterer where the magnitude of the velocity is 2m/s and the grid spacings are $\Delta x = \Delta y = 0.5cm$. The instantaneous Dopplers for the 4 FDTD simulation cases (free space and the 3 walls) are shown in Fig.5.7a through Fig.5.7d. Ideally for free space, the instantaneous Doppler at every point in the simulation space is 32Hz at the frequency of 2.4GHz. In Fig.5.7a through Fig.5.7d, it is observed that the Doppler in most of the space is equal to 32Hz. The small deviation (with an RMS value of 0.1Hz) that is detected in Fig.5.7a is due to the FDTD numerical noise and finite-differencing error associated with equation (5.5). Fig.5.7b shows the Doppler map for the homogeneous wall. A slightly higher deviation of 1Hz is observed in the region very close to the wall. As seen earlier in Fig.5.6b, this effect is mostly a result of the significant wall refraction in this region. In the case of the reinforced concrete wall in Fig.5.7c, higher deviation error of approximately 1.6Hz to 2Hz is observed due to the phase distortions introduced by the wall inhomogeneity. In the final case of the

cinderblock wall in Fig.5.7c, there are some regions where the wall reverberation interferes destructively, thus resulting in very faded amplitudes.

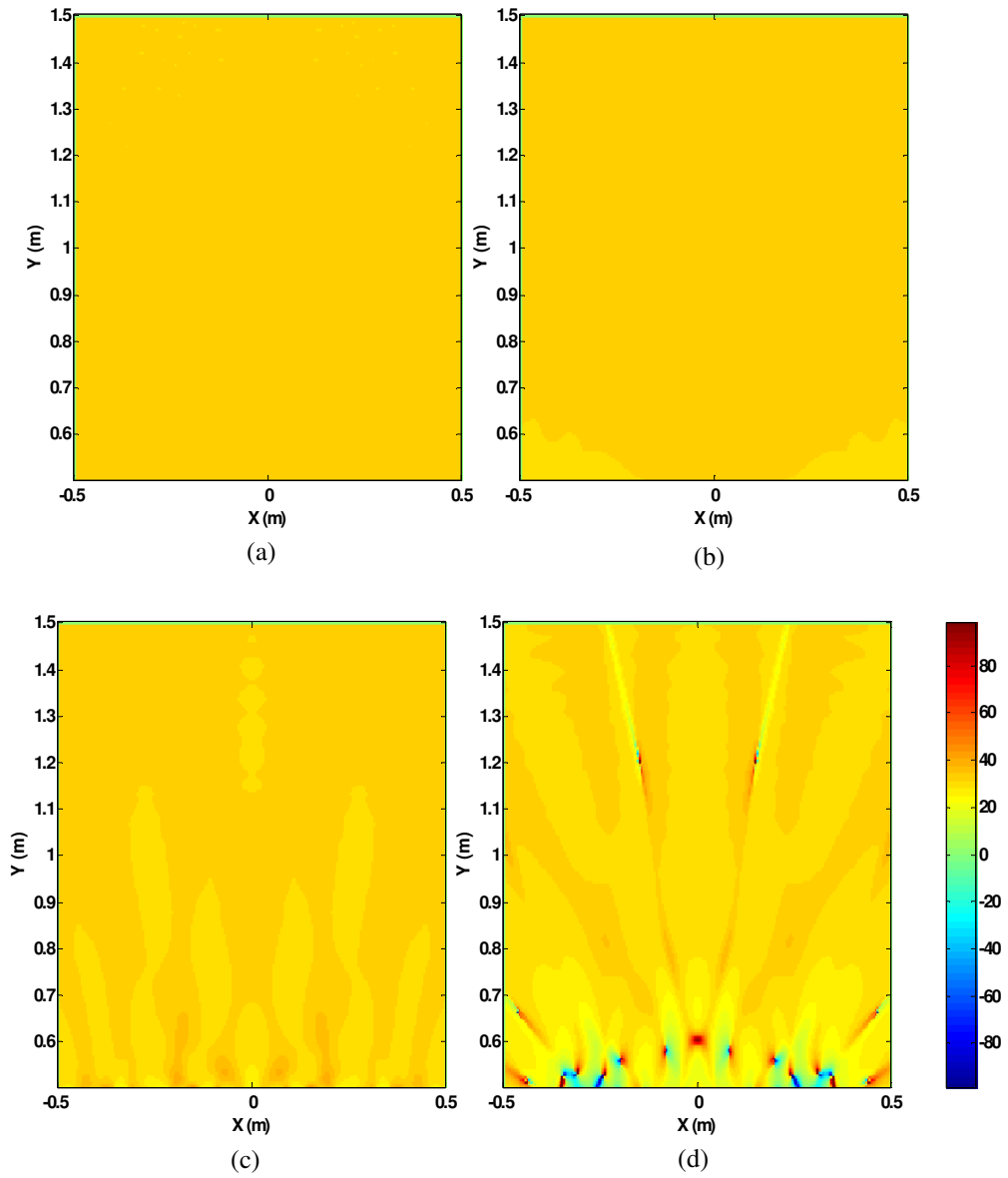


Fig.5.7. Doppler map for radial path motion of point scatterer at 2.4GHz for (a) free space, (b) homogeneous wall, (c) reinforced concrete wall and (d) cinderblock wall.

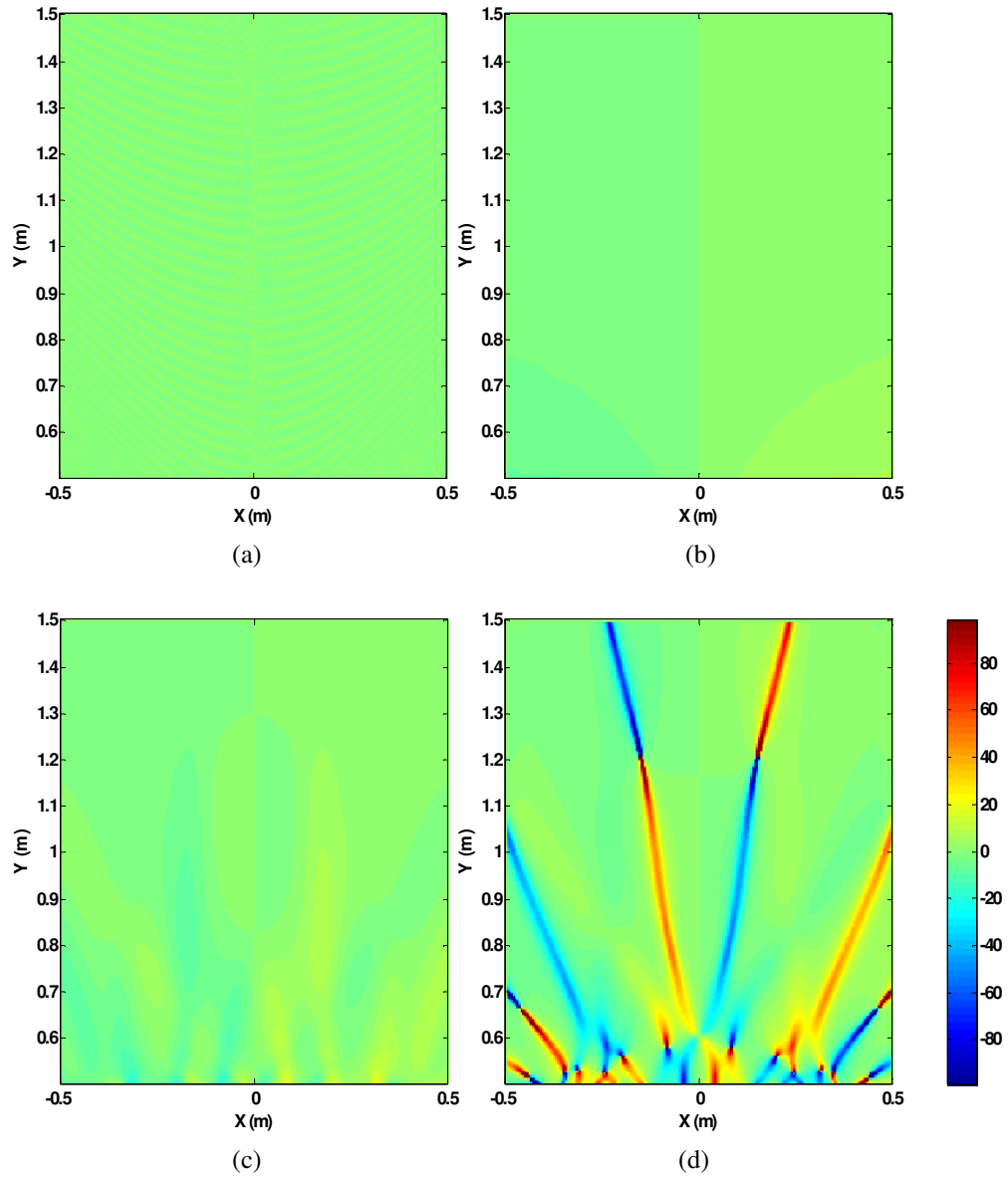


Fig.5.8. Doppler map for tangential path motion of point scatterer at 2.4GHz for (e) free space, (f) homogeneous wall, (g) reinforced concrete wall and (h) cinderblock wall.

Since the phase is not well defined in these regions, the Doppler deviation from that of free space can be quite high. However, these regions manifest themselves in the spectrogram as amplitude fades. For most of the other spaces, the Doppler does not deviate from 32Hz by more than 2Hz.

Next, the point scatterer is assumed to be at position (x, y) and move in a tangential path with respect to the radar. The Doppler is computed for every point in the grid space for each of the four cases using equation (5.5). This time α is the angle between the tangential velocity vector, v_t , and the X axis. The results are presented in Fig.5.8a through Fig.5.8d. The instantaneous Doppler for every point in the simulation space for free space is zero as observed in Fig.5.8a (numerical noise results in an RMS deviation of 0.1Hz). However, higher Doppler deviations are observed in the through-wall cases. Wall refraction and multipath gives rise to non-zero Dopplers in the homogeneous wall, reinforced concrete wall and cinderblock wall cases as seen in Fig.5.8b through Fig.5.8d. The RMS Doppler deviation for the homogeneous wall case is 1.3Hz and the reinforced concrete wall case is 2Hz. In the cinderblock wall case, some regions in Fig.5.8d show very high Doppler deviation due to the ill-defined phase caused by amplitude fades. The RMS Doppler error for the rest of the region is approximately 2Hz. From this analysis, it is seen that the effect of walls on the Doppler frequencies of a point scatterer is quite minor. This finding is consistent with the conclusions drawn from both the simulation and measurement results reported earlier in Section 5.4.

5.6. FURTHER INVESTIGATIONS

Some additional complex through-wall cases are investigated next. First, the effect of walls on human Dopplers when the human is oblique to the radar is analyzed. Next, a case where the human is between two walls is considered. This situation results in considerable interference between the waves bouncing off the two walls.

5.5.1. Effect of Obliquely Incident Wave

In Section 5.5.1, the effect of wall refraction on the Doppler of a moving point scatterer was analyzed. The maximum Doppler deviation was observed when the point scatterer was oblique with respect to the radar. This deviation was caused by the

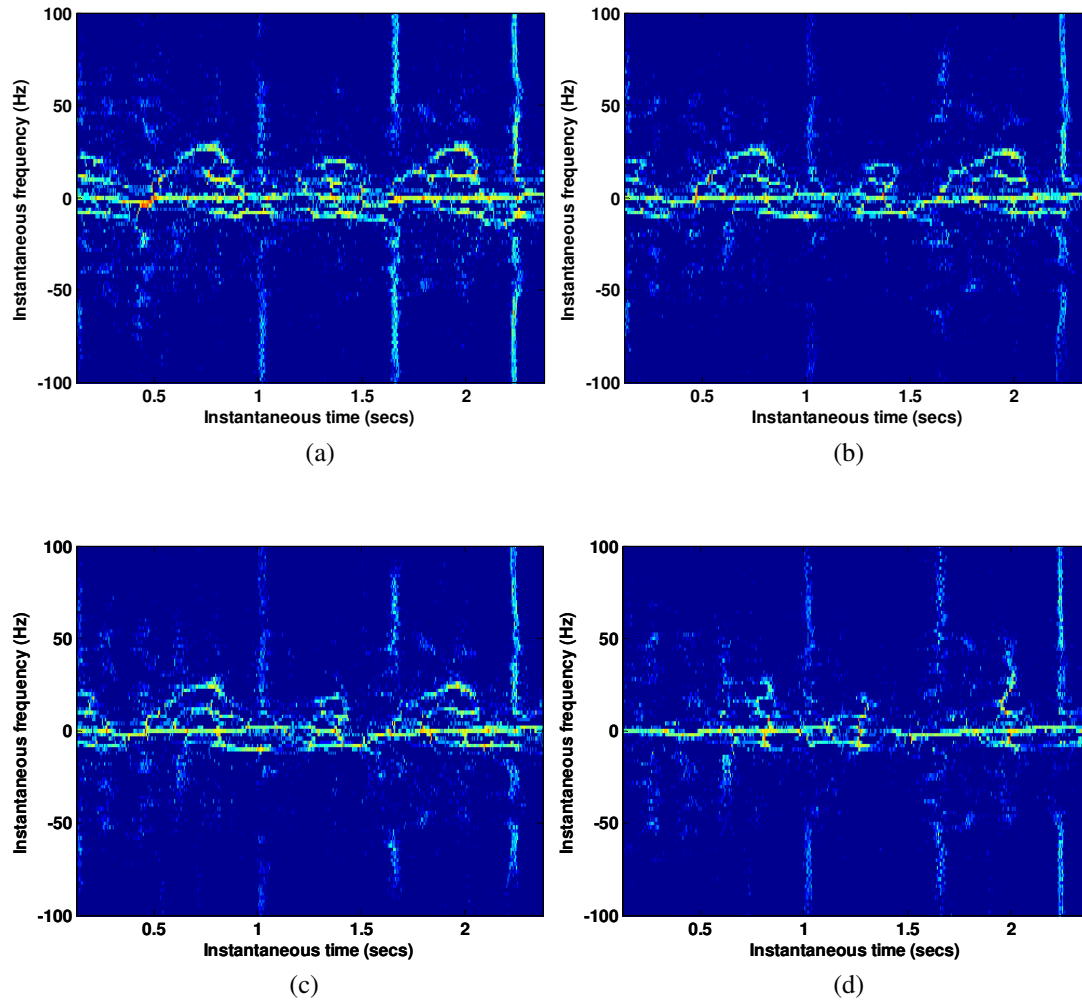


Fig.5.9. Results of simulations of human and wall: Doppler spectrogram of walking human (*human is oblique wrt radar*) at 2.4GHz for (a) free space and (b) homogeneous concrete wall, (c) reinforced concrete wall and (d) cinderblock wall.

significant wall refraction that is introduced at oblique angles. Therefore, the hybrid simulator described in Section 5.3 is used to generate the Doppler spectrograms of a human walking at an oblique angle with respect to the wall. The transmission response is generated for the through-wall case for a simulation space that spans 1.5m x 1.5m ($X: 0$ to $1.5m$, $Y: 0$ to $1.5m$) assuming that the pulse source is located at $(0m, 0.1m)$. The wall spans ($X: 0$ to $1.5m$, $Y: 0.3m$ to $0.495m$). The translation motion of the human is suppressed again by fixing the human hip joint at $(1m, 1m, 1m)$. Fig.5.9a through Fig.5.9d show the resulting Doppler spectrograms for the free space and three wall cases. The reassigned transform is used on the time-domain radar returns. The human motion is no longer radial with respect to the radar and hence the spectrogram shows lower Dopplers than Fig.5.4a. Also, the Dopplers from the left and right limbs are no longer equal since their positions are asymmetric with respect to the radar. When a wall is placed between the human and the radar, both wall refraction and multiple bounces are introduced. However, the Dopplers do not change significantly compared to the free space case as observed in Fig.5.9b through Fig.5.9d.

5.5.2. Effect of multiple walls

Next, the case when the human is situated between two walls is considered. The FDTD simulation space spans 1.0m x 2.0m ($X: -0.5m$ to $0.5m$, $Y: 0m$ to $2m$). Two identical walls, 19.5 cm thick, span the X axis and are located 0.2m and 1.67m from the source, $(0m, 0.1m)$, along the Y axis. The human animation model is constrained within the two walls by fixing the position of the hip joint at $(0m, 1.2m, 1m)$. Fig.5.10a and

Fig.5.10b show the magnitude and phase of the transmitted field at 2.4GHz within the area where the human motion is constrained to occur between two cinderblock walls. Due to reverberations between the two opposite walls, a standing wave pattern is observed in the magnitude response. The phase response of the two-wall case in Fig.5.10b is not considerably different from the single-wall case shown in Fig.5.3d. The resulting spectrograms for the three wall cases are shown in Fig.5.10c through Fig.5.10d. Compared to the results shown in Fig.5.4a, it is observed that the values of microDopplers of the body parts have not significantly changed from the free space case even under the two-wall scenario despite the phase distortion. However, in the cinderblock wall case in Fig.5.10e, the microDopplers from some of the body parts are not visible at all due to the poor magnitude response.

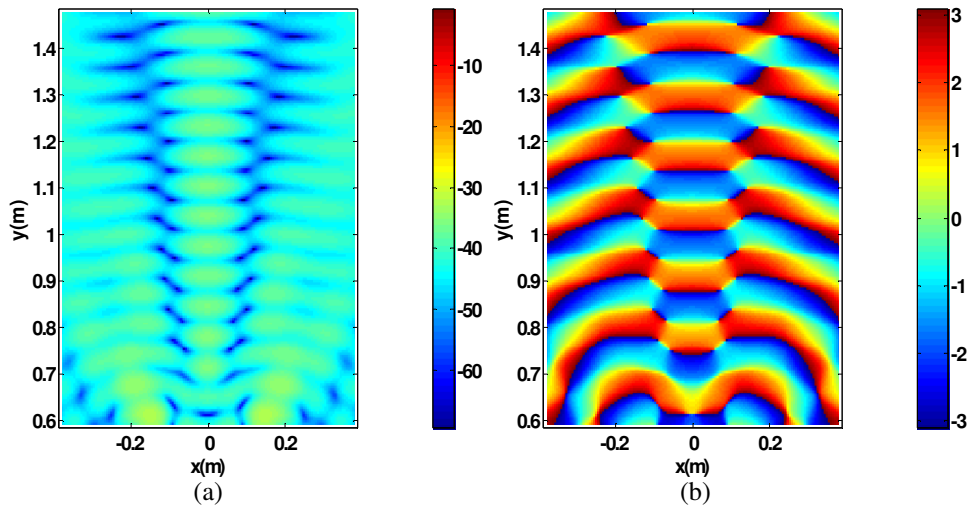


Fig. 5.10.

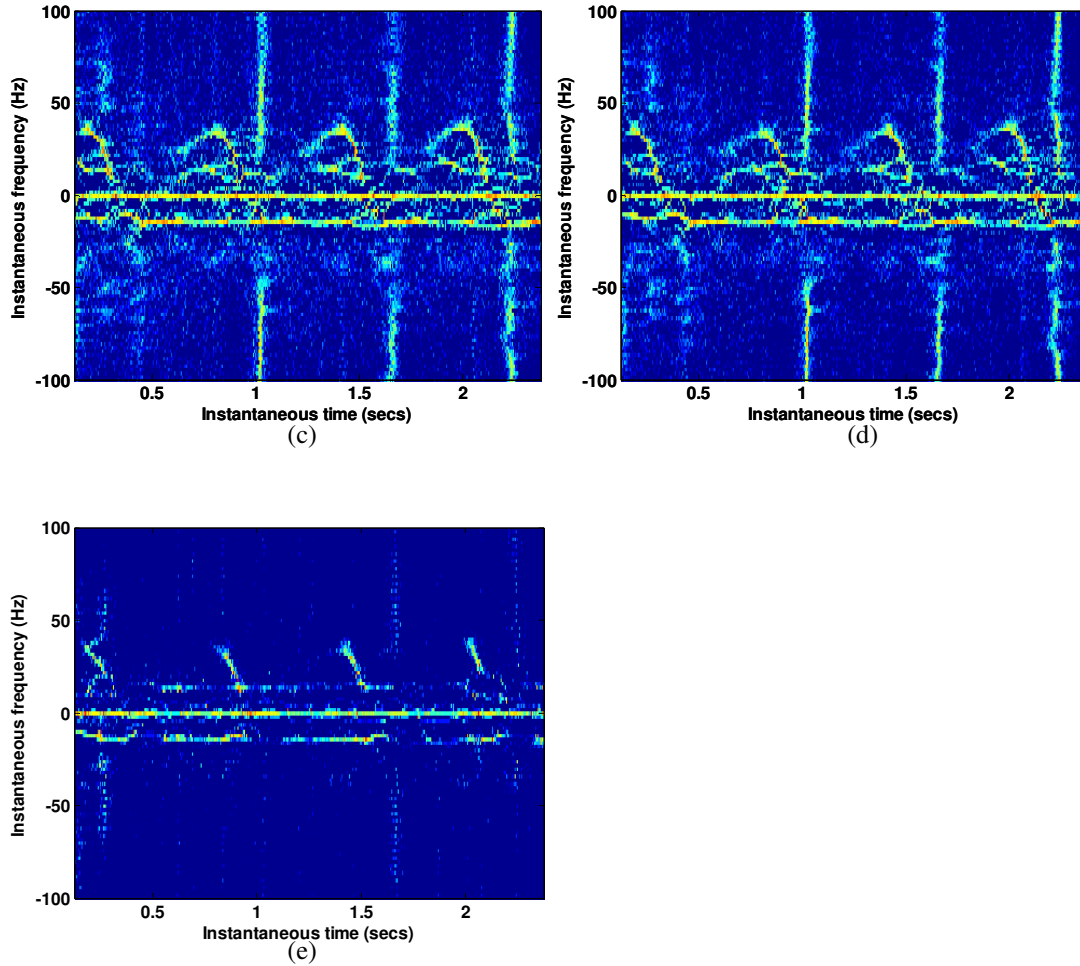


Fig.5.10. Results of simulations of human between 2 cinderblock walls at 2.4GHz: (a) magnitude response and (b) phase response. Doppler spectrogram of human between two (c) homogeneous walls, (d) reinforced concrete walls and (e) cinderblock walls.

5.7. HIGH RANGE-RESOLUTION PROFILE OF A HUMAN WALKING BEHIND A WALL

In the previous sections, the effect of walls on human microDopplers was studied. However, the hybrid human and wall simulator can also be utilized to generate wideband radar returns from a human moving behind a wall. In this section, the effect of walls on

the high range-resolution profile of a walking human generated from wideband radar data is studied.

The SONY human walking animation data are considered again with the position of the human hip joint fixed at joint at $(X: 0m, Y: 1m)$. A radar of 2GHz ($1.4GHz$ to $3.4 GHz$) bandwidth is assumed to be located at $(X: 0m, Y: 0.1m)$.

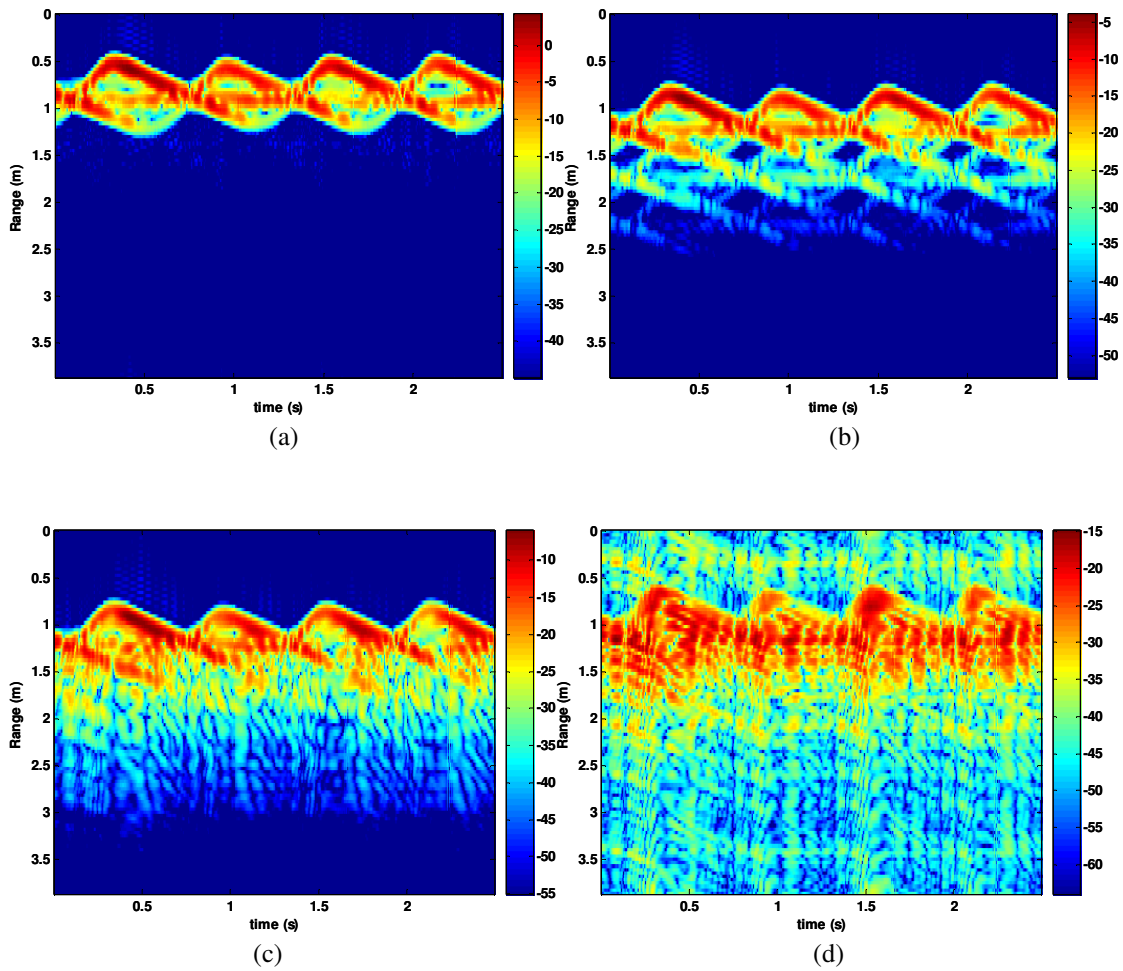


Fig.5.11. Results of simulations of human and wall: Range profile of walking human obtained from UWB waveform of 2GHz ($1.4 - 3.4 GHz$) for (a) free space, (b) homogeneous wall, (c) reinforced concrete wall and (d) cinderblock wall.

The RCS of the human in free space is calculated for each frequency, f_c , within the radar bandwidth using the primitive based prediction technique described in Chapter 2. Using the FDTD simulation described in Section 5.2, the wall transfer function is computed for every point in the simulation space for every f_c . Then the wall and human simulation results are hybridized at every f_c using the technique described in Section 5.3 to calculate the wideband radar returns, $y(t, f_c)$, from the human. The time-varying radar range profile, $Y(t, R)$ is generated by inverse Fourier transforming $y(t, f_c)$ along the f_c dimension:

$$Y(t, R) = \int y(t, f_c) e^{+j \frac{2\pi f_c}{c} 2R} df_c \quad (5.6)$$

Fig.5.11a through Fig.5.11d show the time-varying range profiles of a walking human, at bore sight with respect to the radar, for both the free space case and when the human is behind the three different types of walls. Since the radar bandwidth, β , is 2GHz, the range resolution is $c/2\beta$ which is 7.5cm. Since the translation motion is suppressed, the range of the human torso remains fixed at 0.9m for free space as seen in Fig.5.11a. Due to the periodic motion of the limbs, the ranges of the limbs fluctuate between 0.4m to 1.2m. The feet undergo the maximum displacement. In Fig.5.11b, the homogeneous wall case, the signal strength is attenuated by about 10dB. Also, the wall introduces a delay in the transmission response. Hence the range of the torso appears to shift to 1.2m. Similarly, the ranges of all the other body parts are also shifted by approximately 0.3m. The multiple bounces of the wave within the wall, give rise to late-time ringing in the range profiles. The effects of attenuation, transmission delay and late-time ringing are also observed in the range profiles of a human walking behind a reinforced concrete wall or a

cinderblock wall cases as seen in Fig.5.11c and Fig.5.11d respectively. In fact, the effect of late-time ringing due to the wall reverberation is so severe in the cinderblock wall case, that some of the late-time returns have aliased over into the early-time region of the range profile. Thus the presence of interior multipaths within the wall appears to introduce considerable distortion on the range profiles of the human motion.

5.8. CONCLUSION

A simulation methodology has been developed for generating the microDoppler radar signatures of humans moving behind walls. The human modeling was combined with independent wall-transmission data generated using the FDTD technique. The hybrid was carried out by substituting the free-space propagation delay of each human part by the corresponding through-wall transfer function generated from FDTD. The resulting simulator was used to analyze the effects of different types of walls on human microDopplers. It was found that while through-wall propagation affected the magnitude response of the Doppler spectrogram in the form of attenuation and fading, it only introduced very minor distortions on the actual Doppler frequencies from the body parts. This conclusion was supported by measurement data collected using a Doppler radar testbed and theoretical analyses of wall refraction and multipaths.

In this work, only a two-dimensional FDTD simulation was used. A full three-dimensional FDTD analysis would provide a more accurate result at the expense of much higher computational resources. However, it is believed that the conclusions reached here will not be significantly altered in the case of the full three-dimensional simulation.

The same methodology introduced here was also used to simulate the high range-resolution profiles of humans behind walls from wideband radar. It is interesting to note that the degradation in the range returns caused by the wall was quite severe. Therefore, significant processing will be needed to properly deconvolve the wall effects. In contrast, the Doppler information is little affected by through-wall propagation.

6. Simulation of Floor Effects on Human Signatures

6.1. INTRODUCTION

The non-rigid motions of the different human body parts are manifested either as time-varying range profiles for wideband radars or time-varying microDoppler returns for Doppler radars. It is of interest to study if the propagation environment between the human and radar can significantly distort the human radar signatures. In the previous chapter, the effects of transmission through walls on the microDoppler signatures and high range-resolution profiles of humans were studied. Another problem that is of interest is the effect of ground on human signatures. It is well known that target-ground interactions can significantly alter the radar signatures of ground vehicles as seen from aerial sensors. In particular the corner reflector created by the base of a ground vehicle and the ground tends to create a strong feature seen in the synthetic aperture radar (SAR) imagery. However, the effect of ground on human signatures has not been addressed to date. In this chapter, the effect of a flat ground on the radar signatures of human motions is simulated. This is carried out by modeling the interaction between the human and the ground using the method of images and a ground reflection coefficient. The simulated signatures of human motions are presented as functions of ground reflectivity, radar elevation and type of motion.

6.2. METHODOLOGY

Fig.6.1 illustrates the methodology used to compute the radar returns of the humans in the presence of the ground. A vertically polarized, monostatic radar is assumed to be located at a height, h_1 , from a flat ground of dielectric constant ϵ_2 . The dielectric constant of the medium of the incident wave is ϵ_1 which is assumed to be 1 (air). The RCS of the human is computed using the primitive based method described in Chapter 4, with computer animation data of the human as the input. Each bone of the human body is modeled as a simple primitive ellipsoid, whose RCS, is σ . Multiple interactions between the different body parts and shadowing are ignored in this construct. Next, the human interaction with the ground is incorporated by the method of images [58]. The propagation from the radar to each body part is described by two mechanisms: the direct path and the ground-reflected path from the radar to the phase center of the body part. To simplify the analysis, the phase center of the body part is assumed to be the same for both the direct path and ground-reflected path. At time instant t , the phase center of a body part is assumed to be at a height h_2 , from the ground. The direct path length and the ground-reflected path length are r and r_1+r_2 respectively and θ is the angle of incidence at the specular reflection point on the ground. Assuming a vertically polarized wave of frequency f_c , the radar returns from the body part at time instant t is given by

$$\begin{aligned}
y_b(t, f_c) &= \sqrt{\sigma} \left[\frac{1}{r} e^{-j\frac{2\pi f_c}{c} r} + \frac{\Gamma_V(\theta)}{r_1 + r_2} e^{-j\frac{2\pi f_c}{c} (r_1 + r_2)} \right]^2 \\
&= \sqrt{\sigma} \left[\frac{1}{r^2} e^{-j\frac{2\pi f_c}{c} 2r} + \frac{2\Gamma_V(\theta)}{r(r_1 + r_2)} e^{-j\frac{2\pi f_c}{c} (r + r_1 + r_2)} + \frac{\Gamma_V^2(\theta)}{(r_1 + r_2)^2} e^{-j\frac{2\pi f_c}{c} 2(r_1 + r_2)} \right]
\end{aligned} \tag{6.1}$$

where Γ_V is the Fresnel reflection coefficient for the vertical polarization given by [58]:

$$\Gamma_V(\theta) = \frac{\varepsilon_1 \sqrt{\frac{\varepsilon_2}{\varepsilon_1} - \sin^2 \theta} - \varepsilon_2 \cos \theta}{\varepsilon_1 \sqrt{\frac{\varepsilon_2}{\varepsilon_1} - \sin^2 \theta} + \varepsilon_2 \cos \theta} \tag{6.2}$$

Note that in the two-way path between the radar and each body part on the human, 3 distinct mechanisms are generated:

- (1) the direct-direct path,
- (2) the reflected-reflected path,
- (3) and the direct-reflected path (or the reflected-direct path).

The radar returns of the human are computed from the complex sum of the radar returns from all the body parts.

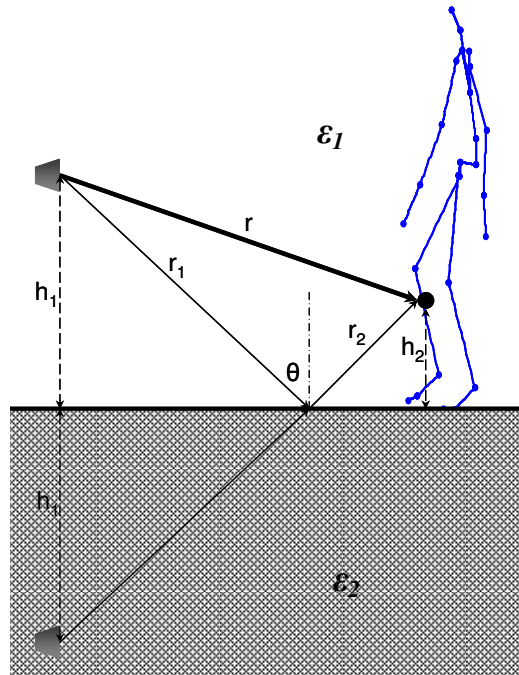


Fig.6.1. Simulation methodology

6.3. RESULTS

A 3-second duration human walking motion obtained from the ACCAD Motion Capture Lab of Ohio State University is considered. The radar is assumed to be located at a height of 1m above the ground. First, the radar returns are computed for each time instant over a 2GHz bandwidth (1.4 GHz to 3.4 GHz) using equation (6.1), assuming that the ground is absent. The wideband data is inverse Fourier transformed along the frequency dimension to obtain the time-varying range profiles of the human walking motion, which is shown in Fig.6.2a. The range of the human torso decreases from 6m to 2m as the human approaches the radar. The swinging movements of the arms and legs give rise to fluctuating features in the range profile. The inset in the figure shows the range of the right foot over a 0.5s duration. Next the radar range profile of the same

motion is generated while assuming first, that the ground is smooth with a dielectric constant of 5 (Fig.6.2b) and second, that the ground is perfectly conducting, PEC (Fig.6.2c).

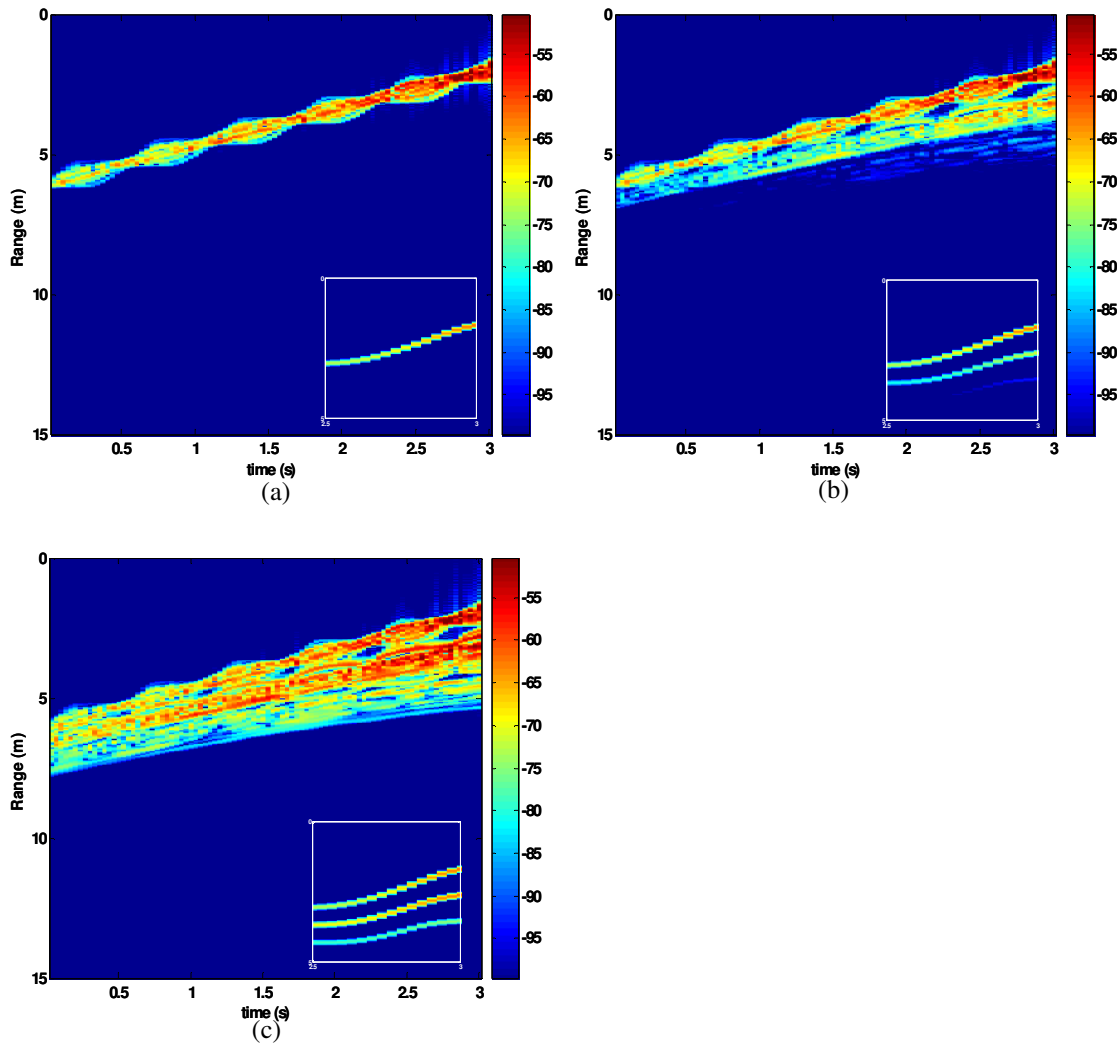


Fig.6.2. High range-resolution signature of human walking towards a radar 1m high, (Inset figures are of the right foot), (a) without floor, (b) smooth floor with $\epsilon_r=5$ and (c) PEC floor.

The range profile in Fig.6.2b clearly shows the additional range features arising from ground reflection. In fact, three components are clearly visible in the range profile

of the right foot in the inset of the figure, corresponding to the direct-direct path, direct-reflected path and reflected-reflected path. In the case of the PEC floor, again the additional range features are observed in the range profile. However, the strength of these features are higher due to the high reflection coefficient from the PEC floor ($\Gamma_V = -1$) for all angles of incidence.

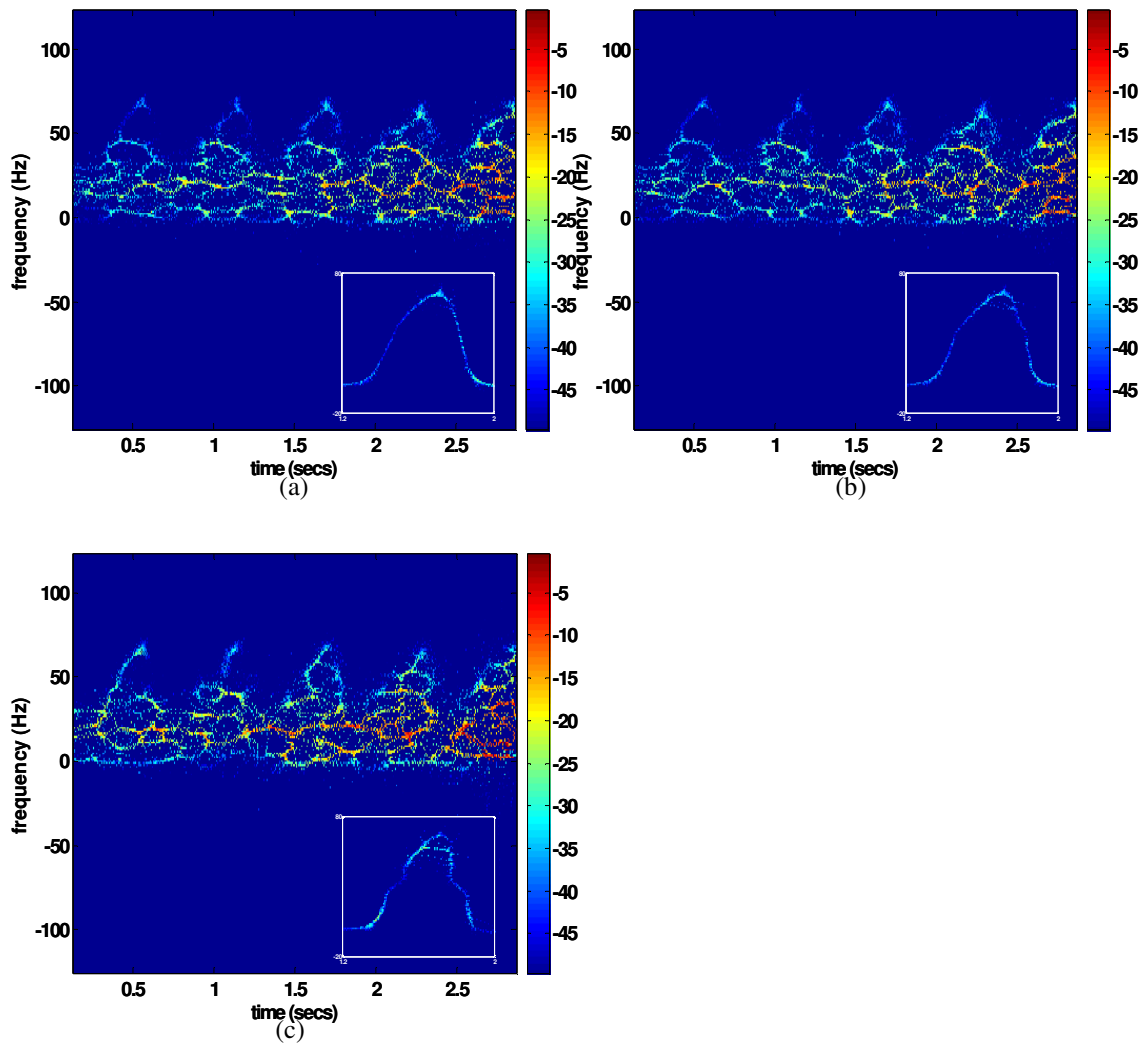


Fig.6.3. Doppler spectrogram of human walking towards a radar 1m high at 2.4 GHz, (Inset figures are of the right foot), (a) without floor, (b) smooth floor with $\epsilon_r=5$ and (c) PEC floor.

Next, the microDoppler signature of the human walking motion is generated by applying the reassigned joint time-frequency transform on the time-varying radar returns of the human computed for a carrier frequency of 2.4GHz. The spectrogram in Fig.6.3a, is generated while assuming that the ground is absent. The figure shows the time-varying microDoppler features due to the movement of the human torso, arms and legs. The inset in the figure examines more closely the highest Doppler arising from the motion of the right foot over a 0.8s duration. The spectrograms in Fig.6.3b and Fig.6.3c, are generated under the assumption that the ground is dielectric and PEC respectively. The microDopplers of the body parts do not show significant changes from those in Fig.6.3a. The effect of both types of ground on the human microDopplers for low radar elevation of 1m appears minimal.

Next, the radar is raised to an elevation of 20m. The radar range profiles are generated for the right foot for three cases: no ground, dielectric ground and PEC ground as shown in Fig.6.4a through Fig.6.4c. Again, three distinct range features are observed in Fig.6.4b and Fig.6.4c arising from respectively the direct-direct, direct-reflected and reflected-reflected paths. Fig.6.5a through Fig.6.5c are the microDoppler signatures of the right foot when the radar is at 20m elevation. In comparison with the no-ground case (Fig.6.5a), the microDoppler tracks in Fig.6.5b and Fig.6.5c shows noticeable blurring. This is caused by the different incident and observation angles of the three propagation paths between the radar and the foot. It is particularly severe for the PEC floor case.

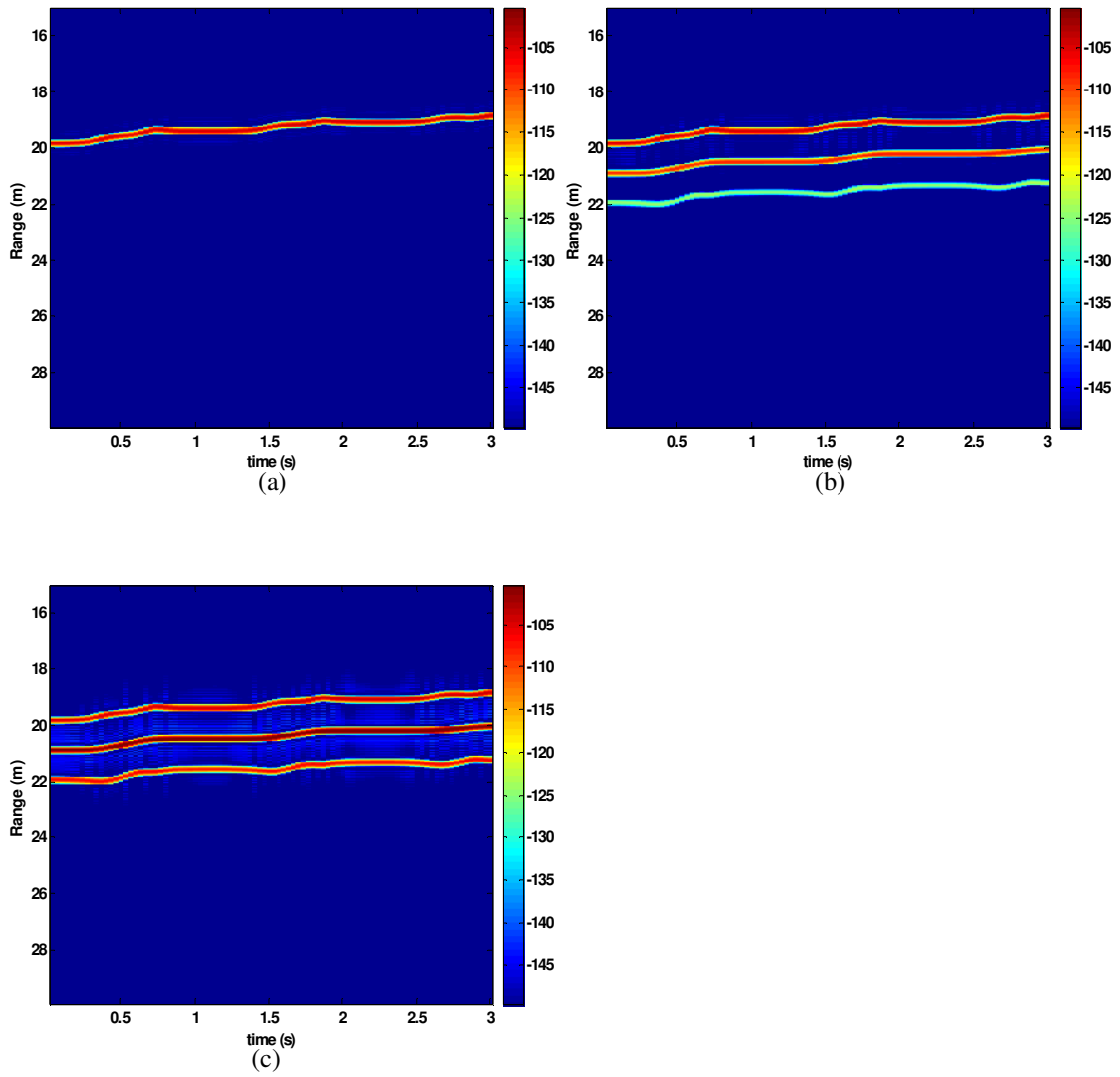


Fig.6.4. High range-resolution signature of right human foot when human is walking towards a radar 20m high, (a) without floor, (b) smooth floor with $\epsilon_r=5$ and (c) PEC floor.

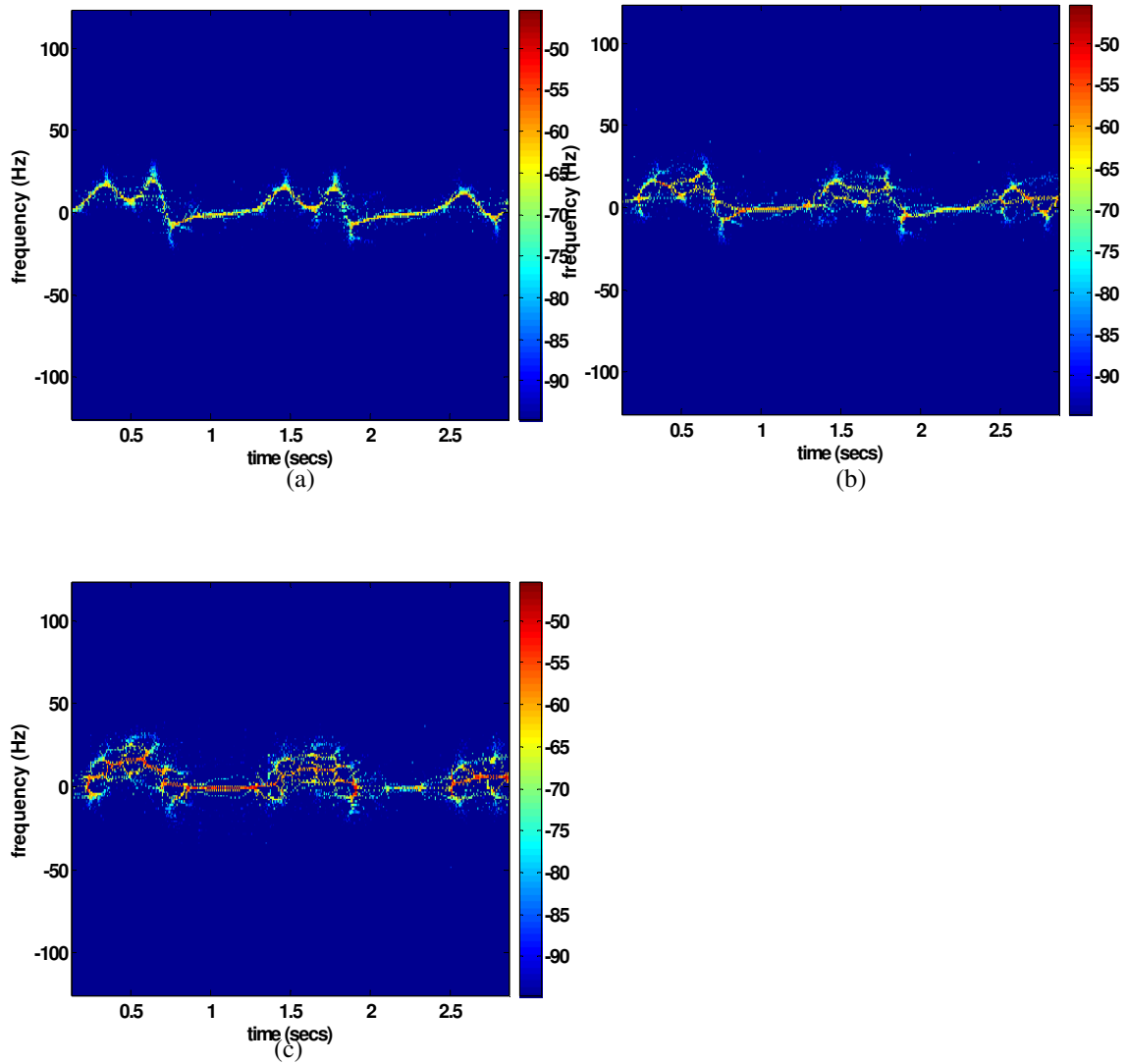


Fig.6.5. Doppler spectrogram of right human foot when radar is 20m at 2.4GHz, (a) without floor, (b) smooth floor with $\epsilon_r=5$ and (c) PEC floor.

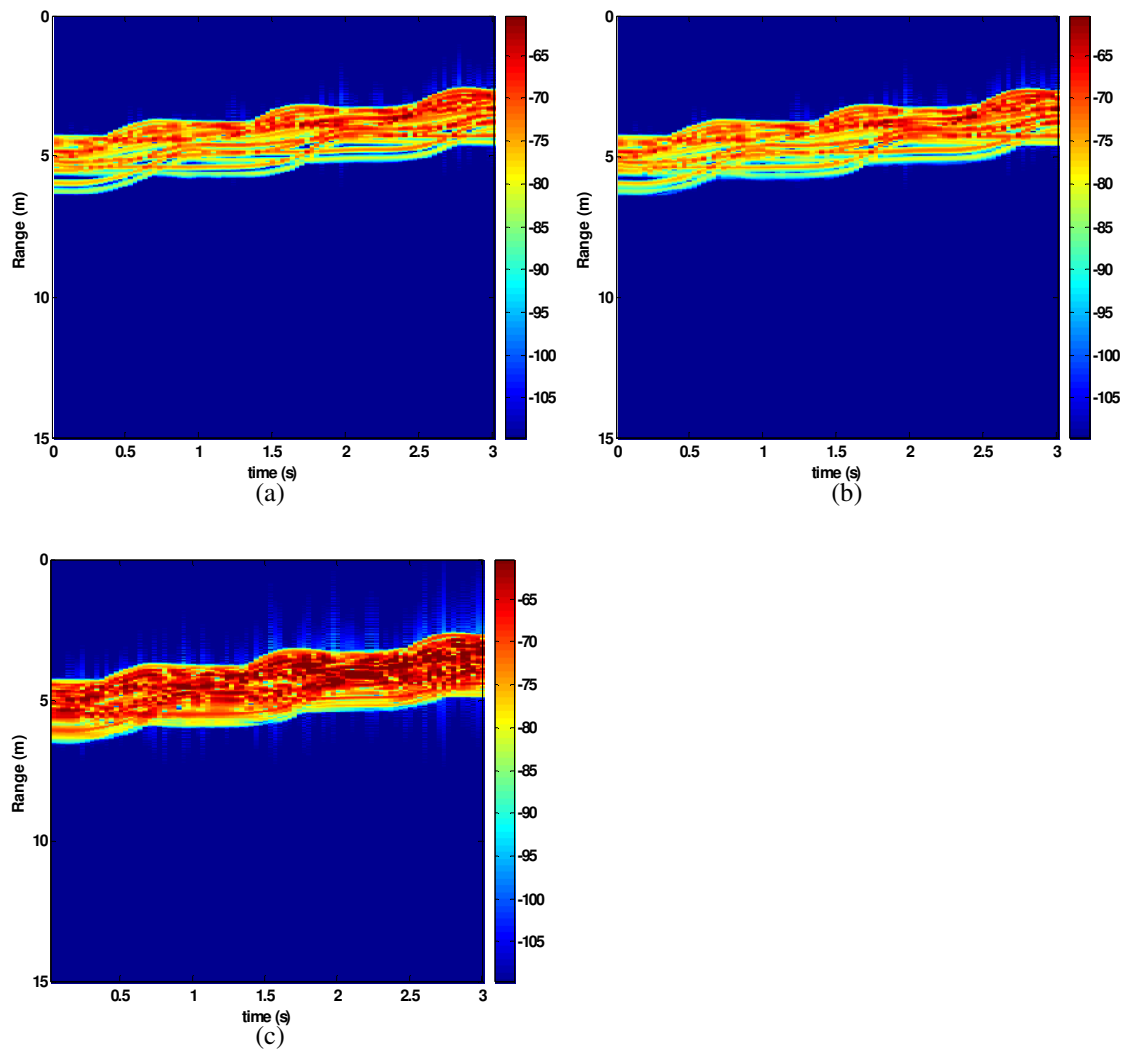


Fig.6.6. High range-resolution signature of human crawling towards a radar 1m high, (a) without floor, (b) smooth floor with $\epsilon_r=5$ and (c) PEC floor.

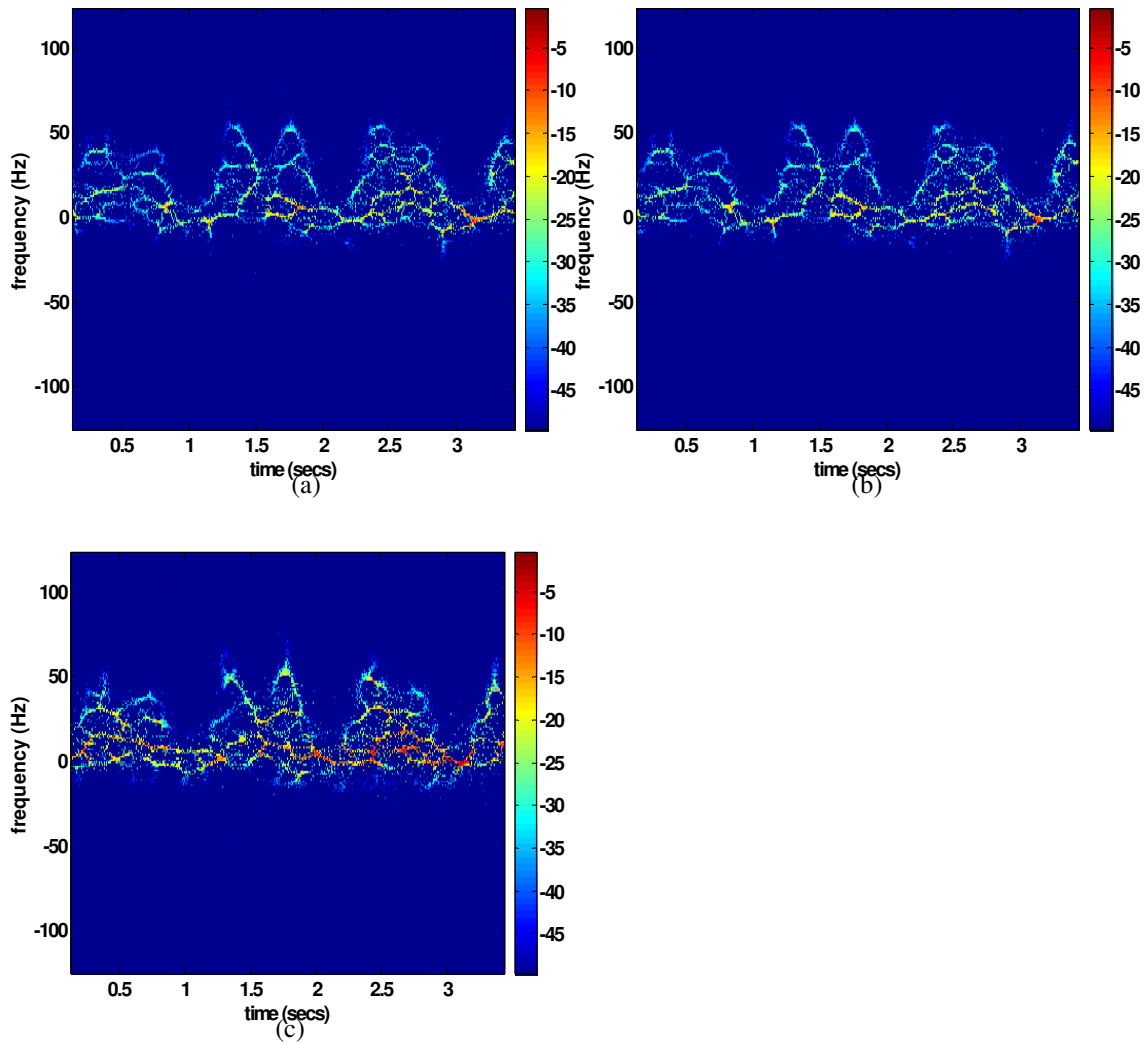


Fig.6.7. Doppler spectrogram of human crawling towards a radar 1m high, (a) without floor, (b) smooth floor with $\epsilon_r=5$ and (c) PEC floor.

Finally the human crawling motion data from ACCAD Motion Capture Lab are considered. First, radar range profiles are generated for the motion. The radar elevation is 1m above the ground. The results are shown in Fig.6.6a through Fig.6.6c. The figures show very little difference from the no-ground case. Since the human is very close to the ground, the length difference between the direct path and the reflected path falls within

the radar range resolution of 7.5cm. Hence the distinct tracks caused by ground reflection cannot be identified in the viewgraph. Also, in the case of the dielectric floor, the reflection coefficient for the vertical polarization is low due to Brewster's phenomenon [58]. This makes the ground reflected returns quite weak in Fig. 6.6(b). The radar returns that reflect off the PEC floor are however higher as seen in Fig.6.6(c). Next, the Doppler spectrograms are generated for the same motion and same radar position. The results are shown in Fig.6.7a through Fig.6.7c. Since the angles of the direct and reflected paths are very close to each other due to the low elevation of the body parts and the radar the microDopplers from the body parts in the ground cases do not significantly differ from the no ground case.

6.4. CONCLUSION

A technique for simulating the high range-resolution and microDoppler signatures of a human moving on the ground has been presented. The direct path and the ground reflected path from the radar to the human give rise to three distinct two-way propagation paths between the radar and the human. The effect of ground on human microDopplers is only noticeable at high elevation angles from the radar to the human.

EXPLOITATION OF THE RADAR SIMULATION MODEL

7: Distributed Doppler Sensors

Radar offers some distinct advantages over other types of sensors for monitoring and tracking humans. They are capable of operating 24/7, under all weather conditions and in non-line-of-sight environments. However, one of the limitations of radar sensors when compared to optical sensors is that human movements cannot be directly visualized from the radar signatures. Hence, there is interest in developing techniques that will convert radar data to a visual animation of the human undergoing activities. This is one of the most challenging goals in through-wall radar imaging. In the following two chapters, the radar simulation model of human signatures developed in the previous chapters is exploited to investigate and evaluate two sensor concepts that set out to generate such a radar image of a moving human..

7.1. INTRODUCTION

From the discussions in Chapter 3, it is clear that the microDoppler phenomenon provides a wealth of information on human movements. However, to translate the measured microDoppler data into a geometrical image of a human is a very challenging task. In [33],[62] human walking motion parameters were extracted from the microDoppler data from a single Doppler radar. The resulting parameters were then used to animate the Thalmann model for human gait [40]. In this chapter, we explore an alternate approach to visualize the human motion by collecting microDoppler data from a spatially distributed set of Doppler radars. We are motivated by several previous works

that have shown it is possible to estimate the location and velocity of a single point scatterer (such as a baseball or the human torso) from the Doppler-only data collected from multiple sensors [52],[53]. As an extension of these works, we try to estimate the time-varying position and velocity coordinates of the different point scatterers on the human body (torso, two arms and two feet), and as a result, generate an articulated “image” of a human. The major challenge in this process is the accuracy needed to resolve the very close-by scattering points on the human. To test this concept, we utilize the radar simulation model to generate the human microDoppler spectrograms. Feature extraction of the microDoppler spectrogram is first performed to isolate the Dopplers from different body parts. Estimation of the velocity and position is then performed using a local search. Finally, Kalman filtering [63] is performed to denoise the resulting data.

7.2. METHODOLOGY

The following radar geometry is considered: 16 monostatic Doppler radars ($i = 1:16$) operating at 2.4GHz symmetrically span the perimeter of a 8m x 8m space (X, Y) with 4 sensors on each side of the square. The sensors are spaced 0.13m apart along the height dimension Z to span a 2m elevation as shown in Fig.7.1. Computer animation data are used to describe a 3-second duration walking motion of a human within this space. The human radar returns are simulated and the Doppler spectrogram at each radar is generated by applying the STFT with a dwell time of 0.25s.

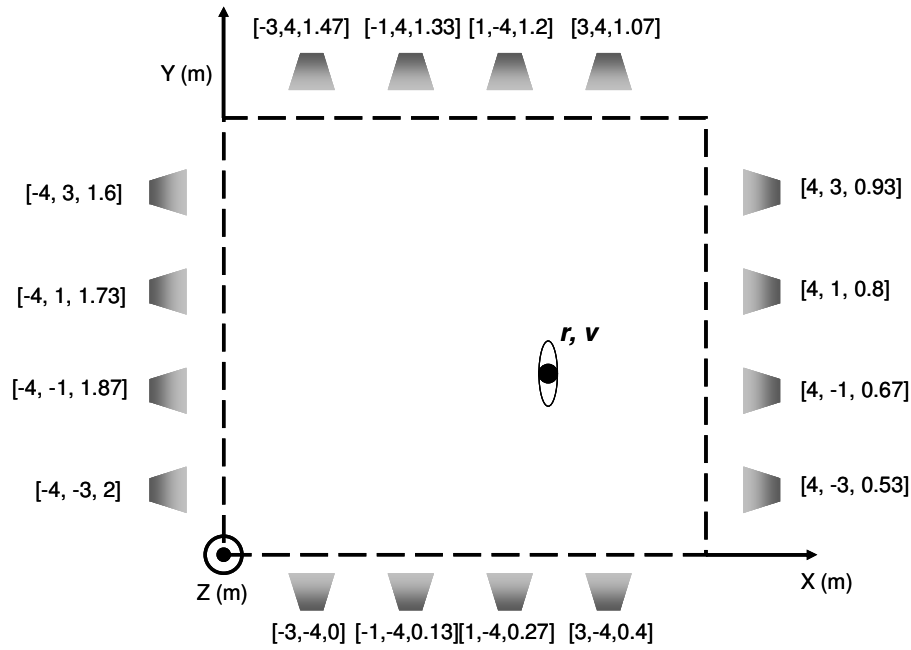


Fig.7.1. Distributed Doppler sensors

7.2.1. Feature extraction from the Doppler data and correspondence across sensors

Fig.7.2 shows the Doppler spectrogram generated at a radar sensor located at $(-4, -3, 2)$ m. The following features are extracted from each of the 16 spectrograms. At any time instant t , the Doppler corresponding to the strongest returns is extracted. Usually, this Doppler f_i^{torso} , arises from the motion of the human torso. Next, the highest, second highest, lowest and second lowest Doppler features are also extracted. These features arise from the motion of the human limbs. Fig.7.3 shows the 5 features extracted from the Doppler spectrogram shown in Fig.7.2. The key challenge is to correctly correspond each Doppler feature across multiple sensors. The following model based reasoning is used to address this correspondence problem. For the human walking motion, at any time instant

one foot always moves with the highest speed of all the body parts, while the other foot remains almost still.

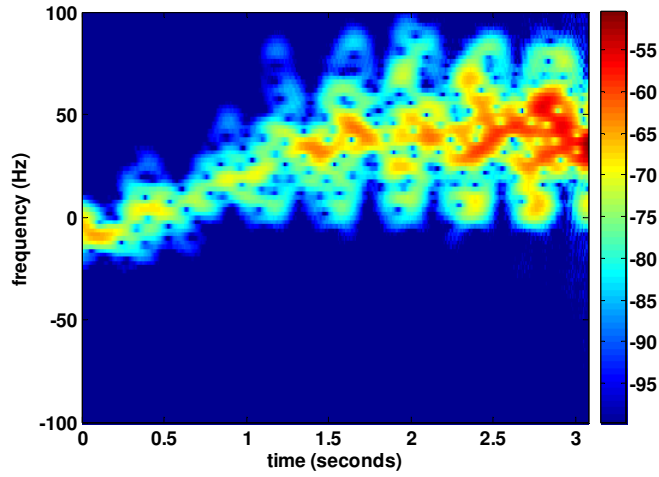


Fig.7.2. Doppler spectrogram of walking human generated for 7.2GHz from sensor located at (-4,-3,2)m.

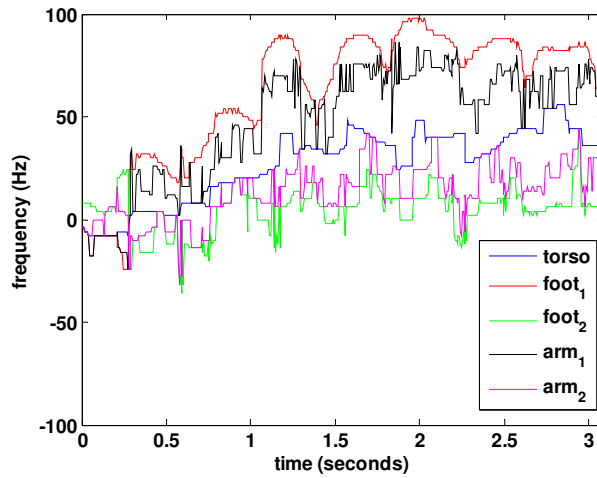


Fig.7.3. Extracted features from the Doppler spectrogram in Fig.7.2.

Hence, the highest absolute Dopplers $|f_i^{foot1}|$ extracted from all the spectrograms correspond to one foot while the lowest absolute Dopplers $|f_i^{foot2}|$, to the other foot. It is

important to note that if the torso is moving away from the radar, that is if $f_i^{torso} < 0$, then $f_i^{foot} < 0$. Next, the second highest and second lowest absolute Dopplers, $|f_i^{arm1}|$ and $|f_i^{arm2}|$, are identified to arise from the motion of the arms.

7.2.2. Inversion of Doppler data to obtain position and velocity

The Doppler of any of the 5 body parts, $f_i^b(t)$, extracted from the spectrogram of radar i , is a function of the time-varying position $\mathbf{r}^b(t)$ and velocity $\mathbf{v}^b(t)$ of the body part, and the position of the radar \mathbf{r}_i , as shown in:

$$f_i^b = g(\mathbf{r}^b, \mathbf{v}^b, \mathbf{r}_i) = \frac{2f_c}{c} \mathbf{v}^b \cdot \frac{\mathbf{r}_i - \mathbf{r}^b}{|\mathbf{r}_i - \mathbf{r}^b|} \quad (7.1)$$

In [53], the position \mathbf{r}_e^b , and velocity \mathbf{v}_e^b , of the torso were estimated by using an artificial neural network. Here, the *fminsearch* routine in MATLAB is used to minimize the mean square error between the extracted and estimated Dopplers from all the sensors:

$$error = \min_{\mathbf{r}_e^b, \mathbf{v}_e^b} \left\{ \frac{1}{16} \sum_{i=1}^{16} [f_i^b - g(\mathbf{r}_e^b, \mathbf{v}_e^b, \mathbf{r}_i)]^2 \right\} \quad (7.2)$$

A large enough number of sensors is chosen to ensure that there is a unique solution to inversion of the non-linear equation. To avoid being trapped in a local minimum, multiple initial guesses with random position and velocity vectors are used in the nonlinear solver at $t=0$. Subsequently, $\mathbf{r}_e^b(t-1)$ and $\mathbf{v}_e^b(t-1)$ are used as the initial guess for estimating $\mathbf{r}_e^b(t)$ and $\mathbf{v}_e^b(t)$. With no errors in the input Dopplers, the algorithm was found to be quite robust in estimating the correct position and velocity of the different body

parts. However if there are input errors from feature extraction, the estimation error in this step is affected by the input errors. This inversion procedure is carried out for all the five body parts: torso, two feet and two arms.

7.2.3. Post processing of the position and velocity estimates of the body parts

Next, some model-based post processing is carried out to distinguish the right and left limbs. The human walking motion is characterized by periodic swinging motion of the arms and legs. If T is the time interval of one human stride, then the highest Doppler extracted, f_i^{foot1} , corresponds to the Doppler of the right foot over $(t : t+T/2)$ and to the left foot over $(t+T/2 : t+T)$. Similarly, the other extracted Dopplers (f_i^{foot2} , f_i^{arm1} and f_i^{arm2}) also alternate between the right and left limbs. Hence the positions and velocity estimates of the two limbs are switched every $T/2$ to correctly account for the trajectory of the right or left limb. Finally, a second-order linear Kalman filter [63], is implemented on the time-domain position and velocity results of each body part. The Kalman filter models the state of the motion of the body part accurately by incorporating both the position and velocity data of each body part to reduce the error in the position estimates.

7.3. RESULTS

Based on the methodology described in the previous section, the time-varying position and velocity of the 5 body parts (torso, two feet and two arms) are estimated. The error of the position and velocity along the Z coordinate v_z was found to be high. This is likely due to the limited elevation extent of the sensors along the Z dimension, which is only 2m. Any increase in the aperture extent along the Z dimension would,

however, result in a more challenging correspondence problem across sensors since at higher elevations, the Dopplers of the arms are higher than the Dopplers of the feet. Also, the velocity of the body parts along the X and Y dimensions v_x and v_y , are much higher than v_z . Hence, the extracted Dopplers in equation (7.1) are dominated by v_x and v_y .

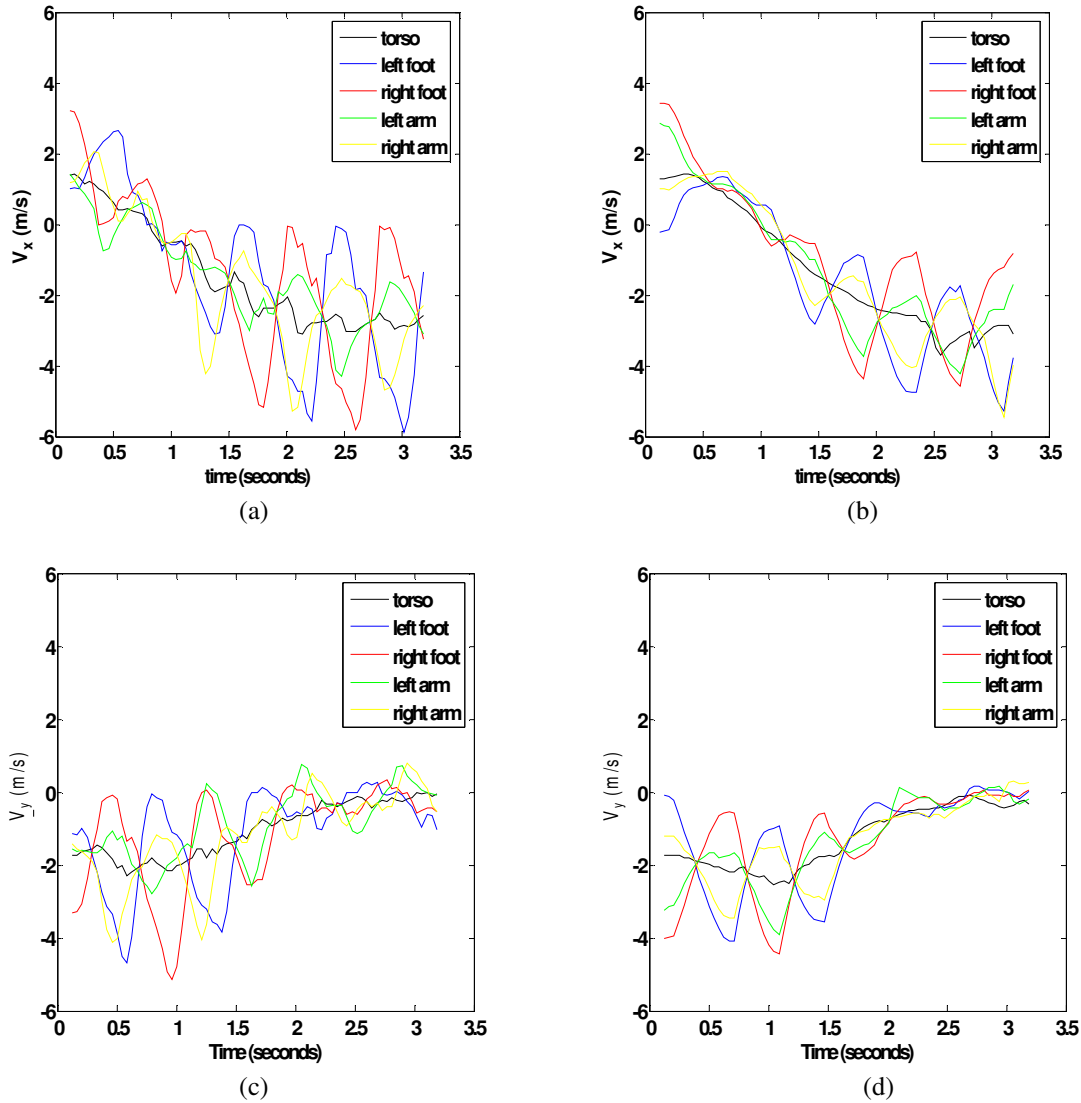


Fig.7.4. (a) Truth values of v_x (m/s) of 5 human body parts, (b) estimated values of v_x (m/s). (c) Truth values of v_y (m/s) and (d) estimated values of v_y (m/s).

The true and estimated values of v_x and v_y for all 5 body parts are shown in Fig.7.4a through Fig.7.4d. From the figures, it is observed that the error is lowest in the estimation of the velocity of the torso. The error in the estimation of the velocities of the arms is highest because of the high feature extraction error. Fig.7.5a shows the true and estimated position of the human torso corresponding to the top view of the human motion. Fig.7.5b and Fig.7.5c show the true and estimated positions of the left and right feet respectively. It is observed that the error is slightly higher in this case when compared to the torso results. This is because while walking, each human foot remains still for approximately half the time period of the motion. Hence, the foot Doppler is near zero, which makes it impossible to accurately estimate its position. Fig.7.5d and Fig.7.5e show the true and estimated positions of the left and right arms respectively. Here, the error is even higher than that of the feet. This error is mostly caused by the poor feature extraction as the Dopplers from the arms coincide closely with the Dopplers of the lower legs.

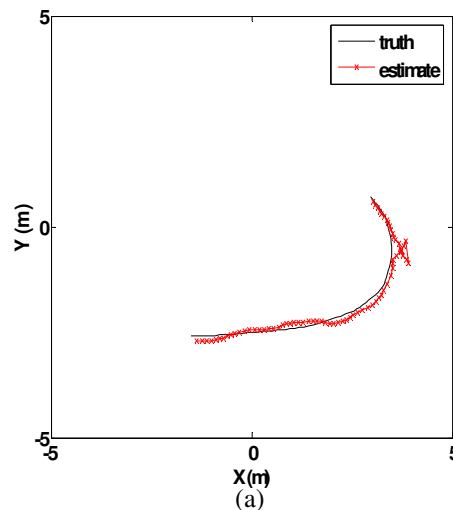


Fig. 7.5. Caption follows.

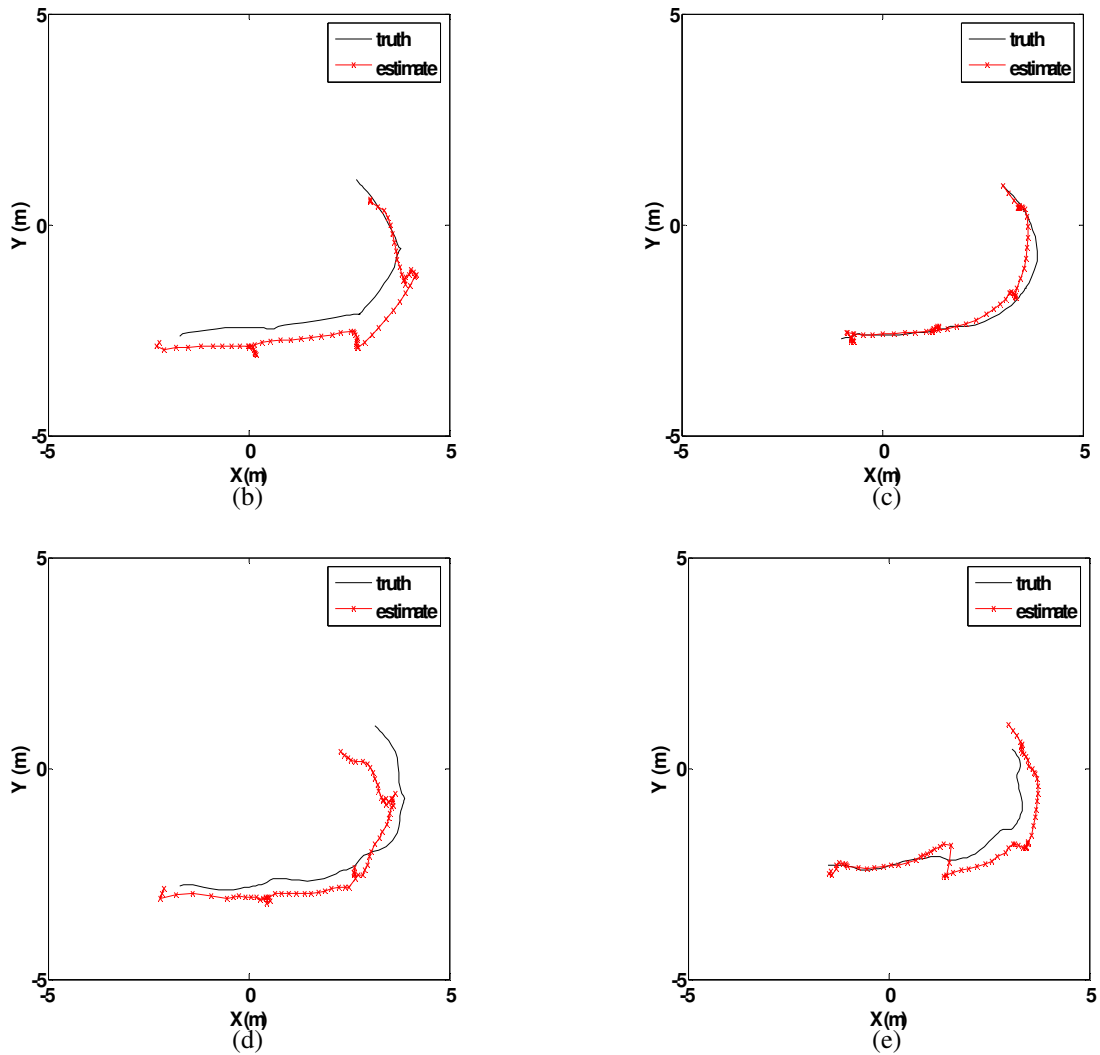


Fig.7.5. True and estimated positions of (a) torso, (b) left arm, (c) right arm, (d) left leg and (e) right leg.

7.4. CONCLUSION

A technique for imaging five prominent point scatterers on the human (torso, two legs and two feet) using the microDoppler data collected from multiple Doppler sensors is presented along with some preliminary results. The accuracy of the estimation of the position of the body parts is mainly limited by errors in the feature extraction. The

method is potentially applicable for visualizing more complex human motions, provided the correspondence issue of extracted Doppler features across multiple sensors could be properly addressed.

Overall, the distributed sensor approach could be logistically difficult to deploy, as it would require proper relaying of data to a central location before they can be processed. Also, the locations of all the sensors must be accurately known. Finally, the issue of mutual jamming among monostatic sensors must be addressed. Therefore, such a setup would only be possible in a well-controlled environment, such as those found in perimeter monitoring applications. In the next chapter, we consider the case where all the sensors are co-located and operate together as an array.

8: Doppler Sensor Array

8.1. INTRODUCTION

In the previous chapter, the concept of using distributed Doppler sensors for imaging the point scatterers on the human body (torso, two arms and two legs) was investigated. In this chapter, we investigate the possibility of using Doppler sensors collocated in an array configuration to address the challenging problem of generating the frontal images of a human undergoing activities. Conventionally, the frontal image of a radar target must be generated using a two-dimensional (2-D) physical array or 2-D synthetic aperture radar (SAR). However both techniques have limitations when humans are considered. For example, if 2-D array processing using Fourier principles is considered at 2.4GHz (12.5cm wavelength), an angular resolution of better than 5 degrees is needed to resolve the head from the feet of a human at a distance of 10m from the radar. This translates into an aperture size of more than 1.5m in both width and height, which is extremely bulky. In the azimuth dimension, the requirement could be even more stringent in order to resolve the left hand from the right hand. Alternately, if the synthetic aperture concept is used to generate large aperture data, the entire collection must be completed before any significant movements from the human. However the human is rarely still and human motions could introduce significant distortions in the image generated from SAR data. A more innovative approach is needed to make frontal imaging practical.

In [64], Lin investigated a third technique, a low complexity radar concept to generate a frontal image of a moving human. He implemented a three-element Doppler and DOA radar wherein different body parts of the human were first resolved based on their microDopplers. He then used the three receivers to simultaneously generate the azimuth DOA and elevation DOA locations of the different body parts. This radar is successful in generating the frontal image of a human provided the different body microDopplers are well resolved. However, this assumption is rarely satisfied in practice even for very high carrier frequencies. Hence to make the system more robust, the concept of using three-dimensional (3-D) beamforming is investigated in this chapter.

This technique uses a real array aperture in conjunction with Doppler processing to image a human. The additional Doppler dimension allows the use of a smaller aperture array (number of array elements) than that used in conventional array processing. The methodology for carrying out 3-D beamforming is first presented. Then the concept is tested on a theoretical data model as well as on simulated human signatures. Finally, the smallest aperture size and the lowest carrier frequency required to satisfactorily image a human at a specific stand off distance is investigated and the results are presented.

8.2. METHODOLOGY

8.2.1. Three-Dimensional Beamforming Using Doppler and Array Processing

Consider a 2-D $M \times N$ array (in the Y - Z plane) of Doppler radar transceivers used to image a moving human as shown in Fig.8.1. The array elements are uniformly spaced apart by length d . The different parts of the human body are located at $(r_b, \theta_b, \varphi_b)$ where

r_b is the distance of the body part and θ_b and φ_b are the DOA elevation and azimuth positions respectively with respect to the radar. If each body part moves with a radial velocity v_b with respect to the radar, then the time domain returns at each element (m, n) of the array at time instant t is given by:

$$e(m, n, t) = \sum_b a_b e^{-j \frac{2\pi f}{c} 2[r_b - (m-1)d \sin \theta_b - (n-1)d \cos \theta_b \sin \varphi_b - v_b t]} \quad \begin{array}{l} m = 1 : M \\ n = 1 : N \end{array} \quad (8.1)$$

where a_b is the scattering strength of the body part at time t .

The first step towards generating a frontal image of the human is to implement 3-D Fourier beamforming to resolve the human body parts along Doppler, azimuth and elevation dimensions. First, STFT is carried out on the time-domain array data to retrieve the instantaneous Dopplers of the different body parts.

$$e(m, n, f) = \int e(m, n, t) h_1(t - \tau) e^{-j2\pi f \tau} d\tau \quad (8.2)$$

Here, h_1 is a sliding Hamming window function. Therefore, the resulting function is a function of time t also. This is followed by 2-D spatial beamforming as shown by:

$$\begin{aligned} & E(\sin \theta, \cos \theta \sin \varphi, f) \\ &= \sum_{m=1}^M \sum_{n=1}^N \{e(m, n, f) \times h_2(m, n)\} e^{-j \frac{2\pi f}{c} 2[(m-1)d \sin \theta + (n-1)d \cos \theta \sin \varphi]} = \quad (8.3) \\ &= \sum_b a_b H[\sin \theta - \sin \theta_b, \sin \varphi - \sin \varphi_b, f - f_b] \end{aligned}$$

Here $h_2(m, n)$ is a 2-D Hamming window function which is used to reduce the sidelobes in the resulting image. H , which is the Fourier transform of the product $h_1 h_2$, is the point spread response of each scatterer in the 3-D space provided the data model in equation

(8.1) is satisfied. The width of H is inversely proportional to the window size used in the STFT operation along the Doppler dimension and the array size along the azimuth and elevation dimensions.

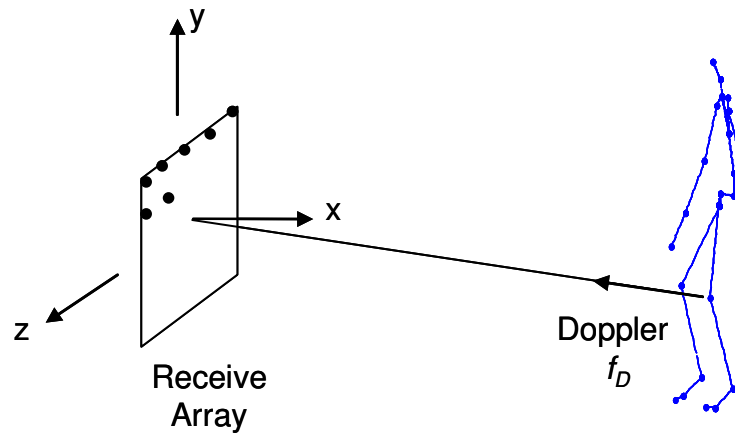


Fig.8.1. Methodology

The actual radar data from humans, however, may not satisfy the data model in equation (8.1). The following deviations may arise:

- (1) The azimuth and elevation of each human body part may not remain constant during the dwell time duration.
- (2) The velocity of the body part may not be constant during the dwell time duration due to presence of acceleration and other higher order motions.
- (3) If the human is close to the radar, near-field effects may result in non-linear phase relationships between the array elements.

These deviations result in a more diffused point spread response, H , for each scatterer.

8.2.2. Projection of Three-Dimensional Results into a Two-Dimensional Frontal

Image

Next, the 3-D image is properly processed so as to project the view onto a 2-D frontal image (in the azimuth-elevation space) of the human, which is the view that most closely resembles what the human eyes see optically. The following methods of projection are investigated.

a. One Dimensional Peak Detection

In this technique, the azimuth φ_p , and elevation θ_p , positions corresponding to the peak strength a_p , of $E(\theta, \varphi, f)$ at every Doppler are computed:

$$a_p(f) = \max_{\theta_p, \varphi_p} |E(\theta, \varphi, f)| \quad (8.4)$$

For display purposes, the extracted parameters $\{a_p(f), \theta_p(f), \varphi_p(f)\}$ for every Doppler are convolved with a point spread response, $H_{small}(\theta, \varphi)$, in the 2-D array space to generate an image of the human. Note that $H_{small}(\theta, \varphi)$ is a theoretical point spread function which is chosen to be of much smaller width in the 2-D space compared to $H(\theta, \varphi)$.

b. Three Dimensional Peak Detection

Alternately, a 3-D peak detection algorithm can be implemented. Here, the local peaks a_p in the 3-D $E(\theta, \varphi, f)$ space are computed along with the corresponding azimuth φ_p , elevation θ_p , and Doppler f_p , positions:

$$a_p = \text{local } \max_{\theta_p, \varphi_p, f_p} |E(\theta, \varphi, f)| \quad (8.5)$$

Then, similar to the previous technique, the extracted parameters $\{a_p, \theta_p, \varphi_p\}$ are convolved with $H_{small}(\theta, \varphi)$ and displayed in the 2-D (azimuth-elevation) space.

It is worthwhile to point out here that algorithms such as CLEAN and RELAX are not useful for estimating the parameters $\{a_b, \theta_b, \varphi_b\}$ corresponding to the different point scatterers on the human body. These techniques require the point spread function H to be well defined. However, as mentioned before, the human radar data significantly deviates from the data model in equation (8.1). These deviations introduce distortions in H and subsequently the CLEAN and RELAX algorithm results.

8.3. RESULTS

8.3.1. Ideal Data Model of 5 Moving Point Scatterers

First, an ideal data model consisting of 5 moving point scatterers based on equation (8.1) is considered. The strength, radial velocity, azimuth and elevation parameters of the 5 scatterers are given in Table 8.1.

#	STRENGTH (v)	VELOCITY (M/S)	AZIMUTH ($^\circ$)	ELEVATION ($^\circ$)
1	100	2	0	5
2	50	4	2.5	0
3	20	1	-2.5	0
4	50	6	1	-5
5	20	0	-1	-5

Table 8.1. Parameters of 5 ideal point scatterers.

A 4 x 4 array of 2.4GHz Doppler radar sensors spaced half-wavelength (6.25cm) apart is considered for imaging these 5 point scatterers. Fig.8.2a shows the true frontal image of the 5 point scatterers. Note that the image is actually a function of $\sin \theta$ and $\cos \theta \sin \varphi$ based on equation (8.3). Since the point scatterers are assumed to be close to bore sight, $\cos \theta$ is close to 1. Also, since the radar sensors are assumed to be transceivers (transmitters cum receivers), there is an additional factor of 2 in the phase terms in equation (8.1). Hence the beam of the radar scans only from -30° to $+30^\circ$ along both the azimuth and elevation dimensions. First, conventional 2-D array processing using Fourier principles is carried out on the data and the resulting image is shown in Fig.8.2b. Due to the limited sized array, the beamwidth of the radar is approximately 20° along both the azimuth and elevation dimensions. Hence, it is not possible to infer the presence of 5 point scatterers from Fig.8.2b.

Next, Doppler processing is implemented in conjunction with array processing based on the methodology discussed in the previous section. It is assumed that the parameters of the scatterers remain constant during the dwell time duration of 0.25s. One dimensional (1-D) peak detection technique is implemented to project the 3-D Doppler-azimuth-elevation space onto the 2-D azimuth-elevation space. The resulting image is shown in Fig.8.2c. The 5 point scatterers are clearly observed in the 2-D image. However, some additional false scatterers are also observed. These arise due to the interference between the Doppler sidelobes of the multiple scatterers.

The exact procedure is next repeated assuming a 4 x 4 array of 7.5 GHz Doppler radar sensors. Again, the array elements are assumed to be spaced half-wavelength (2cm) apart. 3-D Fourier transform is carried out to resolve the scatterers along the Doppler-azimuth-elevation space which is subsequently projected onto the 2-D space. The dwell time is assumed to be 0.18s. The resulting image is shown in Fig.8.2d. Here, the 5 point scatterers are again observed at the correct azimuth and elevation positions. Also since the Dopplers of the different scatterers are now well resolved due to the higher carrier frequency, the mutual interference between them has greatly reduced. This has resulted in fewer false alarms in the image. The study with the ideal data model of 5 point scatterers clearly indicates the advantages of using Doppler processing in conjunction with conventional array processing. However, the human radar data significantly deviates from the ideal data model and is next investigated.

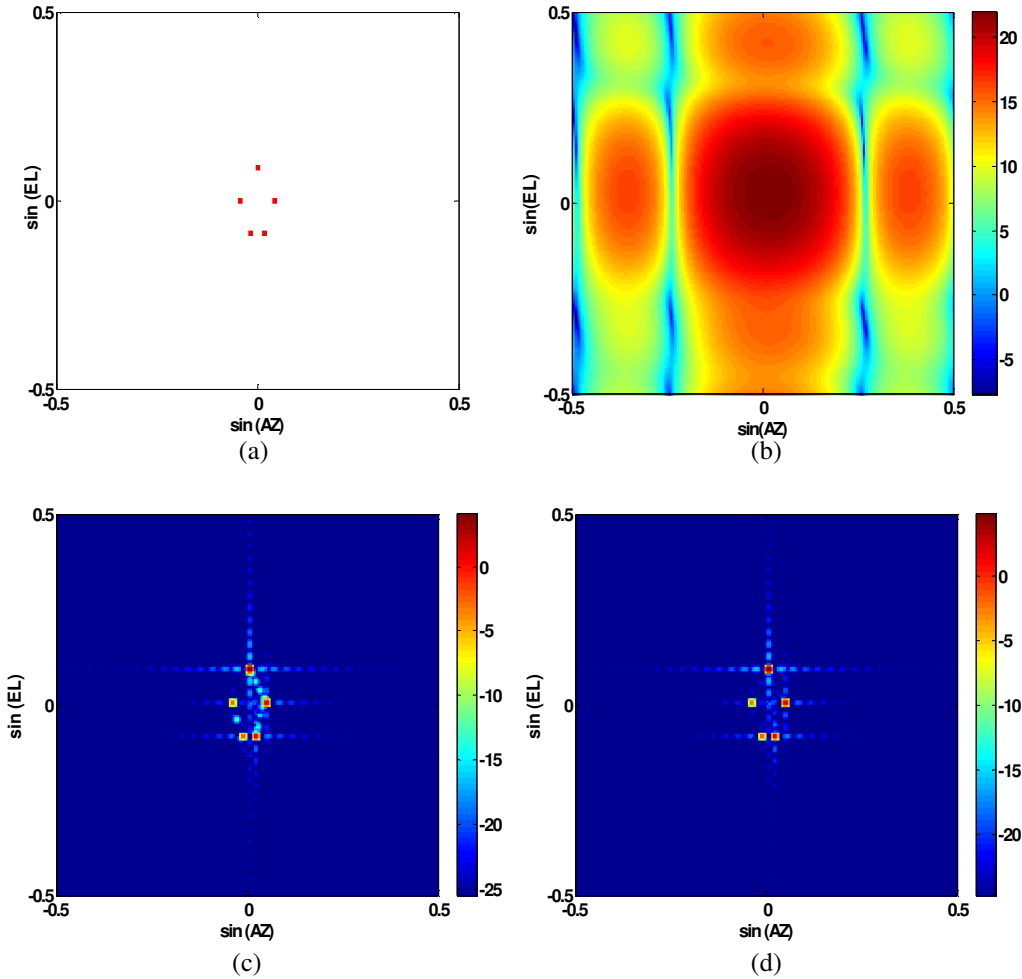


Fig.8.2. 5 ideal point scatterers, (a) True frontal image, Images generated from (b) 4 X 4 array processing, (c) 4 x 4 array processing and Doppler processing at $f_c = 2.4$ GHz, (d) 4 x 4 array processing and Doppler processing at $f_c = 7.5$ GHz.

8.3.2. Human Data Model Using Animation Data

Human walking animation data from Sony Computer Entertainment America are next considered. The human is assumed to walk towards the radar array at bore sight. The returns from the human at each of the radar sensors are simulated, processed using joint Doppler and array processing and projected onto the 2-D space. As the human comes closer to the radar array, the image of the human becomes larger. First, a 5 point scatterer

model of the human consisting of the torso, two hands and two feet is considered. The two different projection algorithms described in Section are tested on the data. Next, the complete human walking model (with 28 point scatterers) is considered. The effect of aperture array size and carrier frequency on satisfactorily imaging the human is investigated.

a. 5 Point Scatterers

In Section 8.3.1, it was observed that the 7.5GHz 4 x 4 array was successful in imaging 5 point scatterers using joint Doppler and array processing. Now, a human walking model with 5 point scatterers is considered. The true frontal image of the human at a standoff distance of 8m is shown in Fig.8.3a. The image of the human is first generated using conventional 2-D array processing and shown in Fig.8.3b. It is observed that the array size is much too small to successfully resolve the multiple point scatterers in the 2-D space. Next, 3-D Fourier beamforming is carried out and the results are projected onto the 2-D space using the 1-D peak detection technique (Fig.8.3c) and the 3-D peak detection technique (Fig.8.3d). Fig.8.3c shows that the 5 point scatterers are

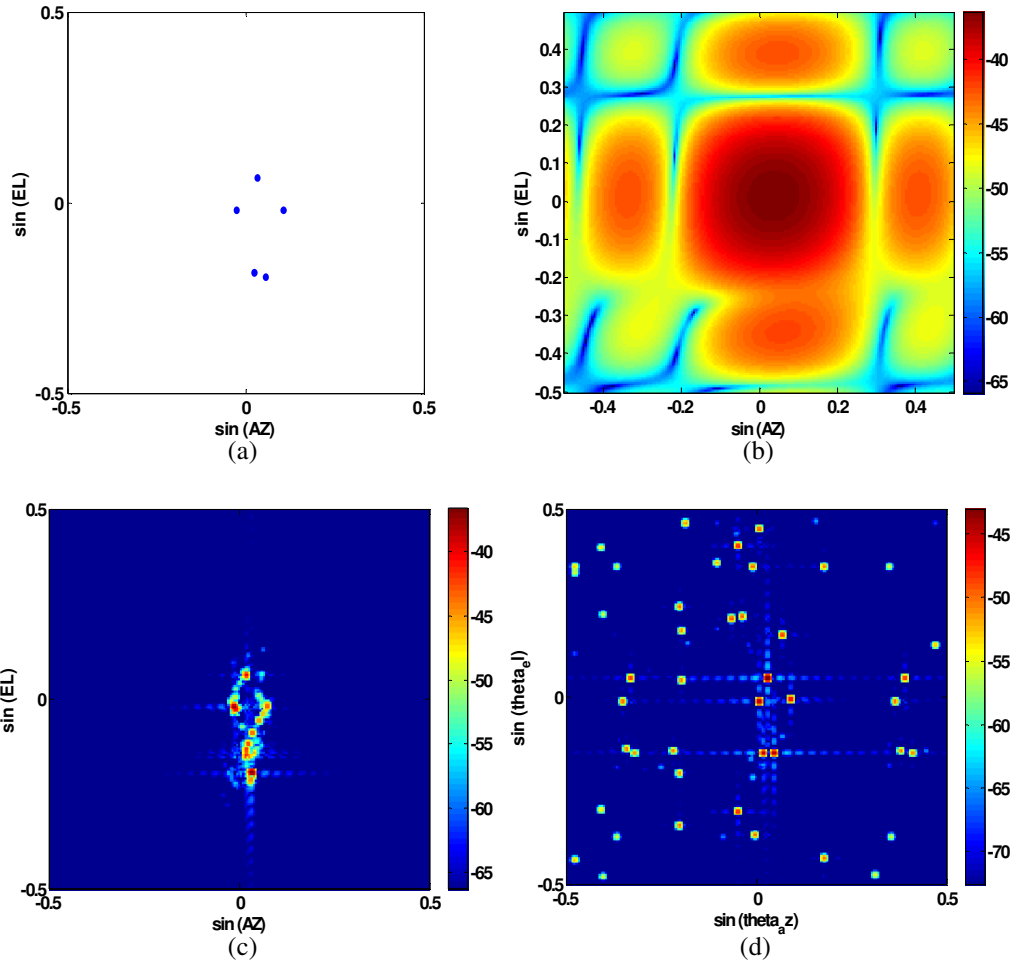


Fig.8.3. 5 point scatterers on human body (torso, two hands and two feet), (a) True frontal image. Images generated from (b) 4 x 4 array processing, (c) 4 x 4 array processing and Doppler processing at $f_c = 7.5$ GHz, (1-D peak detection projection) (d) 4 x 4 array processing and Doppler processing at $f_c = 7.5$ GHz (3-D peak detection projection).

not perfectly resolved in the image unlike the ideal point scatterers data considered in Fig.8.2d. This is because of the deviation of the human radar data from the ideal radar data in equation (8.1). The radial velocity, azimuth and elevation of the point scatterers do not remain constant during the 0.18s dwell time duration. This causes the point spread function of each scatterer to enlarge in the 3-D space which results in increased overlap

between the multiple scatterers. Interference between the overlapping response functions distorts the image.

In Fig.8.3d, the 5 point scatterers of the human body are imaged using the 3-D peak detection technique. This technique succeeds in estimating the approximate center of the point spread response function of each scatterer. Hence, the 5 point scatterers on the human are nicely captured in the image. However, the sidelobes in the 3-D space (along the Doppler and DOA dimensions) are also projected onto the 2-D space. This problem becomes extremely severe when a large aperture array is used. Hence, in the subsequent simulations, 1-D peak detection is used instead of 3-D peak detection.

b. Full Body

Next the complete human walking model with 28 point scatterers is considered. The true frontal image of the human at a stand off distance of 8m is shown in Fig.8.4a. The radar returns from the human are simulated for a 2.4 GHz 4 x 4 array, 10 x 10 array and 20 x 20 array where the array elements are half-wavelength apart. The returns are processed first using array processing and the results are shown in Fig.8.4b through Fig.8.4d. As the array size becomes larger, the beam width of the array narrows which improves the resolution of the image. However, even with a 20 x 20 array, the human image cannot be discerned in Fig.8.4d.

Fig.8.5a, Fig.8.5b and Fig.8.5c use Doppler processing with a 4 x 4 array, 10 x 10 array and 20 x 20 array processing respectively. The additional Doppler dimension enables some point scatterers on the human body to be successfully imaged. The

increased aperture size also results in slight improvement in the images from Fig.8.5a through Fig.8.5c. However, the human microDopplers are still not well resolved at such a low carrier frequency. Hence, even with the 20 x 20 array, a clear image of the human is not obtained.

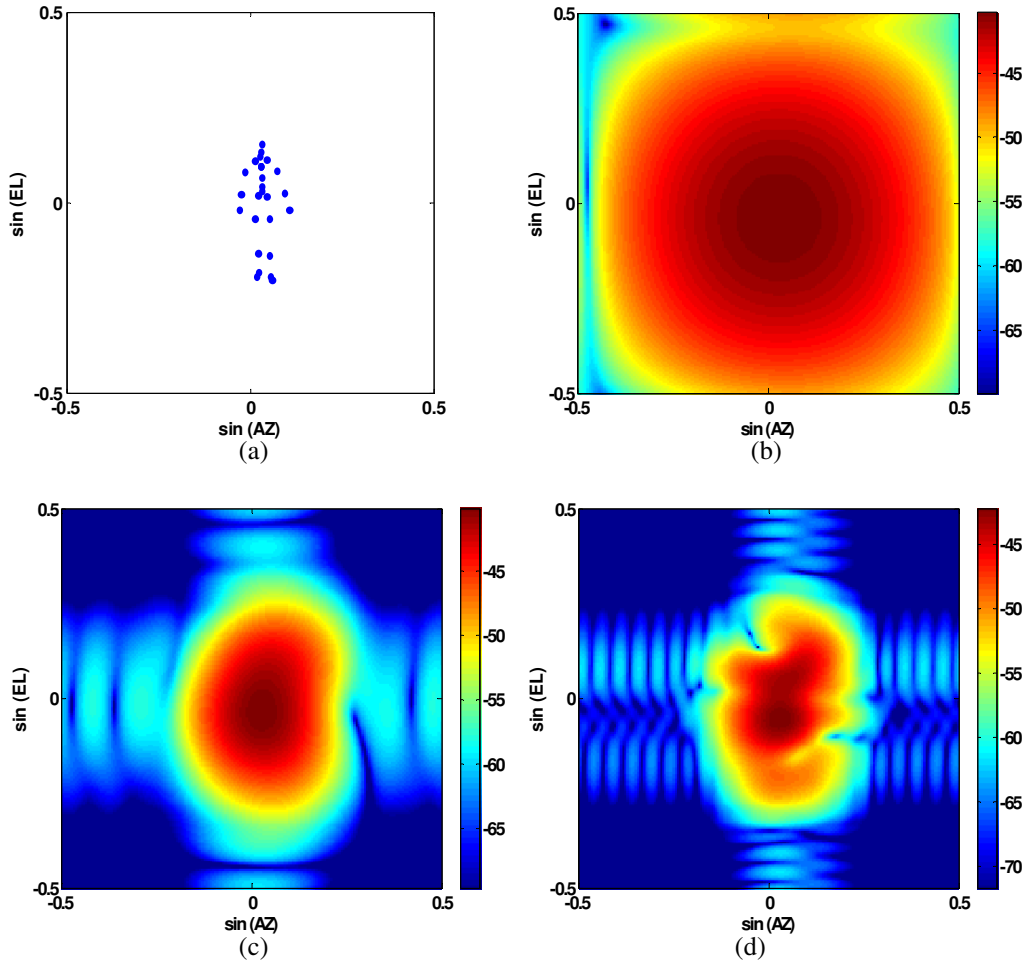


Fig.8.4. Complete human body (28 point scatters), (a) True frontal image. Images generated from (b) 4 X 4 array processing, (c) 10 x 10 array processing and (d) 20 x 20 array processing.

Next, the procedure is repeated with a 7.5GHz array of 4 x 4 elements, 10 x 10 elements and 20 x 20 elements. The results are presented in Fig.8.6a through Fig.8.6c. The resolution of the human microDopplers is improved at the higher carrier frequency. When the array size is small (Fig.8.6a), the poor resolutions in the DOA dimensions

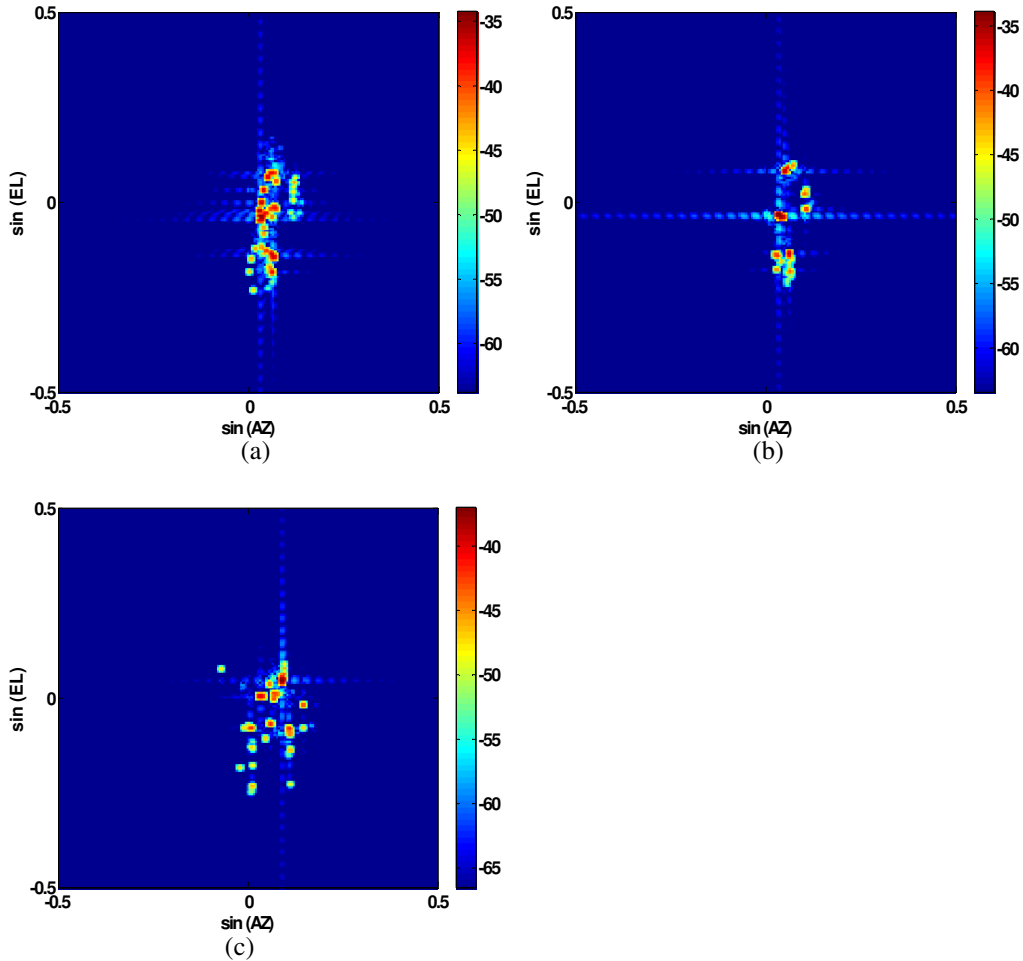


Fig.8.5. Complete human body (28 point scatters): Images generated from Doppler processing with $f_c = 2.4$ GHz and (a) 4 x 4 array processing, (b) 10 x 10 array processing and (c) 20 x 20 array processing.

result in poor imaging. However for the larger array size (Fig.8.6b and Fig.8.6c), the improvement in the human imaging is quite significant. In fact, the human is imaged quite satisfactorily in Fig.8.6c where the head, two arms and two legs are clearly discerned. Thus a combination of Doppler and array processing is successful in generating a frontal image of a walking human.

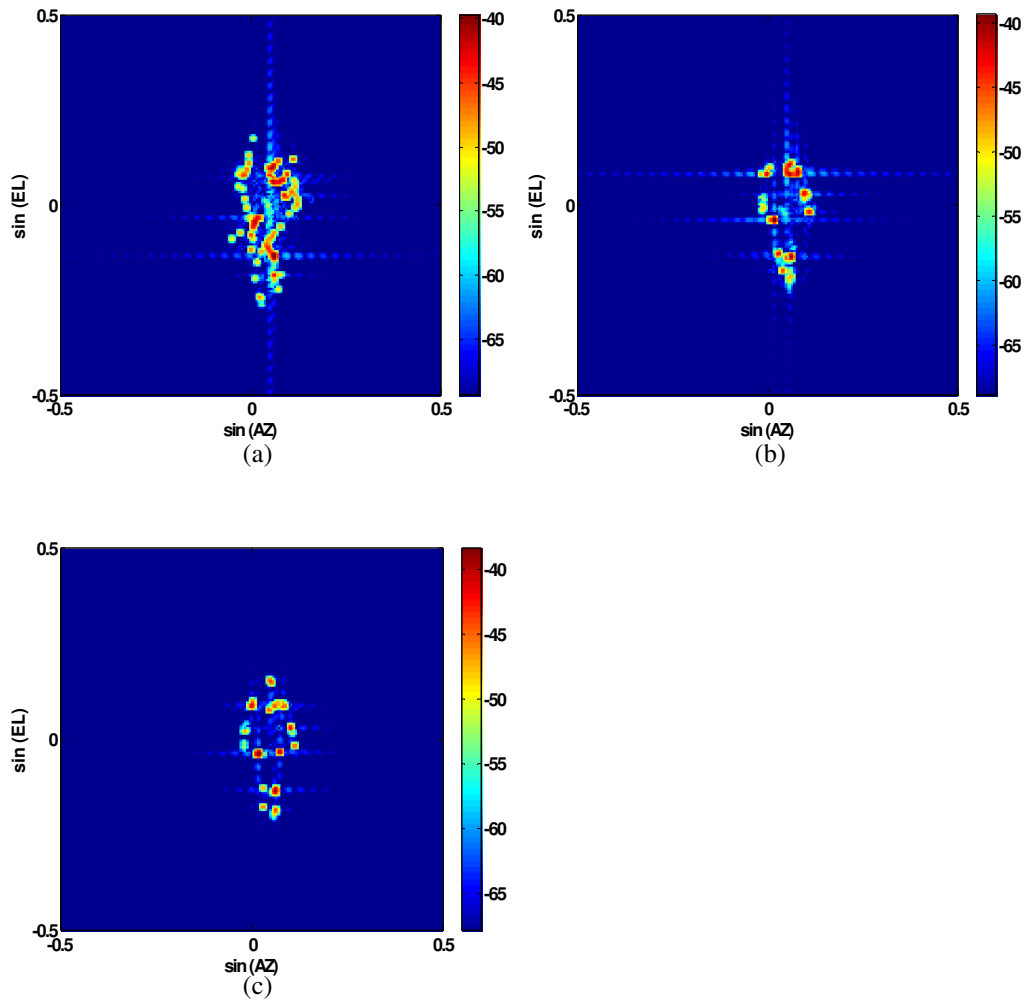


Fig.8.6. Complete human body (28 point scatters): Images generated from Doppler processing with $f_c = 7.5$ GHz and (a) 4 x 4 array processing, (b) 10 x 10 array processing and (c) 20 x 20 array processing.

8.4. CONCLUSION

The concept of generating frontal images of moving humans using joint Doppler and array processing was investigated. Multiple point scatterers of the human body are resolved along the Doppler and DOA dimensions. Then the 3-D Doppler-Azimuth-Elevation space results are projected onto the 2-D space. The aperture size and carrier frequency required for satisfactorily imaging a human at a specific standoff distance from the radar was determined. This preliminary study demonstrates the utility of the simulation capability in easily generating different scenarios (frequency, sensor number, types of motion) for sensor optimization. Additional studies are needed to assess propagation and noise effects, and to explore methods to reduce the required number of sensor elements.

9. Conclusions

The scientific objectives of this dissertation are recapitulated below:

- (1) To develop a physics-based simulator of the scattering mechanisms associated with different human motions as a function of radar sensor parameters such as frequency, bandwidth, dwell time etc.
- (2) To incorporate commonly occurring propagation channels such as building walls and grounds into the radar simulation model of humans.
- (3) To validate the results from the simulator with measurement data collection using a Doppler radar developed in the laboratory.
- (4) To exploit the radar simulator to investigate some new radar sensor paradigms for imaging humans.

The contributions of my dissertation towards realizing these objectives are listed below. Also, potential areas of future research are discussed.

9.1. CONTRIBUTIONS

- (1) The most notable contribution of this dissertation is the demonstration of a new approach that can be used for simulating scatterings from a human undergoing almost any type of complex movement. This approach involves combining animation models describing human motions with electromagnetic models of the human body. The approach allowed us to readily evaluate the effect of sensor parameters such as frequency, viewing angle, bandwidth and dwell time on the resulting human signatures..

- (2) The next important contribution was a methodology that can be used for studying the impact of propagation channels on human radar signatures. This method involved integrating models of propagation channels such as building walls and grounds with the radar simulator of humans. The hybrid allowed us to make detailed investigations of the effects of different types of homogeneous and inhomogeneous walls on human microDopplers. One important observation that was made is that human microDoppler signatures are not distorted by the considerable phase distortion introduced by complex walls. Some distortions in the microDopplers were however observed due to ground effects especially at high radar elevations.
- (3) Next, it was demonstrated that it is possible to detect and track multiple humans indoors through walls using joint Doppler processing and spatial beamforming. The radar used a limited sized Doppler sensor array to resolve multiple movers in the joint Doppler and bearing space thus improving upon the performance of the two-element Doppler and direction-of-arrival radar developed earlier by Lin. Additional signal processing algorithms such as CLEAN and RELAX can be implemented along with beamforming to overcome the problems of high sidelobe levels associated with a limited size array. This radar testbed was useful for simulation validation.
- (4) Next, it was shown that the readability of human microDoppler features can be improved by the application of the reassigned transform on time-domain human radar returns. The reassigned transform improves the signal localization properties

along both the time and frequency domains when compared to the short-time Fourier transform. However, the resolution of the transform is still limited by Fourier uncertainty bounds. Reassigned joint time-frequency distributions enables us to make detailed studies of human microDopplers.

- (5) The concept of using microDopplers extracted from spectrograms generated at multiple spatially distributed Doppler sensors for imaging humans was investigated. It was found that the most challenging problem is to correctly correspond the microDopplers of each body part across the multiple sensors. Errors from feature extraction limit the accuracy of the estimation of the positions of different point scatterers on the human body.
- (6) The concept of using multiple Doppler sensors configured as a 2-D array for generating frontal images of humans was investigated. Conventional 2-D spatial beamforming was found to be inadequate for imaging humans even when large antenna apertures with many Doppler sensors are used. Adding Doppler processing to the array processing helps to resolve the point scatterers in the human body and thus improves the accuracy in the bearing position estimates.

9.2. FUTURE WORK

The following potential areas of future research are identified. In this dissertation, human radar returns and wall phenomenology were independently simulated and later combined to generate the radar returns of humans behind building walls. A further extension of this research would be to study the impact of even more complex

propagation environments on human radar returns. Some examples of such an environment would be a complete 3-D room (walls, ceiling and floor) with furniture or a forest with dielectric trees. If detailed CAD models of these environments are available, computational electromagnetic techniques can be used to generate their propagation function. This function can then be hybridized with the radar simulation model of the human to obtain the human radar returns. The results from these simulations can then form the basis for designing radar sensors that have maximum information gathering capabilities in these environments.

Another topic of future work could be to develop target recognition and classification algorithms using training databases of simulated microDoppler signatures of different types of human and even animal motions. Then these classifiers can be tested with actual measurement data collected from different Doppler radar systems. If their operations are found to be successful, then automatic target recognition algorithms trained by the simulation data can be incorporated into actual radar systems to track and monitor human activities.

Another important research question that follows this work is whether it is possible to develop signal processing techniques that have the ability to resolve the microDoppler tracks of individual body parts in the Doppler spectrogram. The individual tracks will be useful for pinpointing the exact cause of anomalies in the human motion. An example of this anomaly would be if a human were carrying a large heavy object in one arm, then the microDoppler of that arm would be significantly altered. In Chapter 7, we used microDopplers measured at multiple spatially distributed Doppler sensors to

image a human. The performance of this algorithm was limited by error involved in correctly corresponding the microDoppler track of each body part across multiple sensors. Hence, an algorithm that resolves the microDoppler tracks would reduce the feature extraction error to a great extent and improve the accuracy of the estimates of the positions of the different body parts.

Chapter 8 demonstrated the possibility of using joint Doppler and 2-D array processing to image moving humans. However, further research is required to determine the effects of the propagation environment and noise on the performance of the algorithm. Also, efforts should be undertaken to reduce the number of array elements using principles such as random array theory or interferometry to ensure that such a concept is practically viable. After detailed simulation studies, it would be exciting to design, build, and demonstrate such a radar system for through-wall imaging applications.

References

- [1] D. D. Ferris, Jr and N.C. Currie, "A survey of current technologies for through-the-wall surveillance (TWS)," *SPIE Conference on Sensors, C3I Information and Training Technologies for Law Enforcement*, vol. 3577, pp. 62 – 72, Nov. 1998.
- [2] O. Sisma, A. Gaugue, C. Liebe and J-M Ogier, "UWB radar: vision through a wall," in *Personal Wireless Communications*, vol 245, Springer Boston, pp. 241 – 251, Nov. 2007.
- [3] E. J. Baranoski, "Through-wall imaging: Historical perspective and future directions," *Journal of Franklin Institute, Special Issue on Indoor Imaging*, vol. 345, no. 6, pp. 556 – 569, September 2008.
- [4] M. Farwell, J. Ross, R. Luttrell, D. Cohen, W. Chin and T. Dogaru, "Sense through the wall system development and design considerations," *Journal of Franklin Institute, Special Issue on Indoor Imaging*, vol. 345, no. 6, pp. 570 – 591, September 2008.
- [5] L.M. Frazier, "Surveillance through walls and other opaque materials," *Proc. IEEE Natl. Radar Conf. Electron. Syst.*, pp. 27–31, May 1996.
- [6] L. M. Frazier, "Radar surveillance through solid materials," *SPIE Proc. Command, Control, Communications, and Intelligence Systems*, vol. 2938, pp. 139 – 146, Feb. 1997.
- [7] T. B. Gibson and J. C. Jenn, "Prediction and measurement of wall insertion loss," *IEEE Trans. Antennas Propagat.*, vol. 47, pp. 55 – 57, Jan. 1999.
- [8] Nag, S. Fluhler, H. Barnes, M. "Preliminary interferometric images of moving targets obtained using a time-modulated ultra-wide band through-wall penetration radar," *IEEE Radar Conf.*, pp. 64-69, May 2001
- [9] M. A. Barnes, S. Nag, and T. Payment "Covert situational awareness with handheld ultrawideband short-pulse radar" *Proc. of SPIE, Radar Sensor Technology VI*, vol. 4374, pp. 66-77, August 2001
- [10] S. Nag, M. A. Barnes, T. Payment and G. Holladay, "Ultrawideband through-wall radar for detecting the motion of people in real time," *SPIE Proc. Radar Sensor Technology and Data Visualization*, vol. 4744, pp.48-57, July 2002.

- [11] A. R. Hunt and R. D. Hogg, "Stepped-frequency CW radar for concealed weapon detection and through-the-wall surveillance," *Proc. of SPIE, Sensors, and Command, Control, Communications, and Intelligence (C3I) Technologies for Homeland Defense and Law Enforcement*, vol. 4708, pp. 99-105, August 2002.
- [12] A. R. Hunt, "A wideband imaging radar for through-the-wall surveillance," *SPIE Proc., Sensors, and Command, Control, Communications, and Intelligence (C3I) Technologies*, vol. 5403, pp. 590 – 596, Sept. 2004.
- [13] A. R. Hunt, "Image formation through walls using a distributed radar sensor network," *SPIE Proc. Sensors and C3I Technologies for Homeland Securities and Homeland Defense IV*, vol. 5778, pp.169-174, May 2005.
- [14] S. E Borek, "An overview of through the wall surveillance for homeland security," *Proc. 34th Applied Imagery and Pattern Recognition Workshop*, pp. Oct. 2005
- [15] G. Franceschetti, J. Tatoiian, D. Giri and G. Gibbs, "Timed arrays and their application to impulse SAR for through-the-wall imaging," *IEEE Antennas Propagat. Soc. Int. Symp. Digest*, vol. 3, pp. 3067 – 3070, June 2004.
- [16] J. Z. Tatoiian, G. Franceschetti, H. Lackner and G. G. Gibbs, "Through-the-wall impulse SAR experiments," *IEEE Antennas Propagat. Soc. Int. Symp. Digest*, July 2005.
- [17] Cambridge Consultants, "Covert Intelligence at the touch of a button," www.CambridgeConsultants.com, 5th March. 2009, http://www.camcon.co.uk/Downloads/Brochures/prism_200.pdf
- [18] Camero "Xaver 800 Through wall vision," www.camero-tech.com, 5th March 2009, http://www.camero-tech.com/pdf/Camero_Xaver800.pdf.
- [19] E. F. Greneker, "Radar flashlight for through the wall detection of humans," *SPIE Proc., Targets and Backgrounds: Characterization and Representation IV*, vol. 3375, pp. 280 – 285, Apr. 1998.
- [20] E. F. Greneker, J. L. Geisheimer, D. S. Andreasen, O. D. Asbel, B. L. Stevens, B. S, "Radar flashlight three years later: An update on developmental progress," *IEEE Annual International Carnahan Conference on Security Technology, Proceedings*, pp. 257 – 259, Oct. 2000.
- [21] A. Lin and H. Ling, "Three-dimensional tracking of humans using a very low-complexity radar," *Elect. Lett.*, vol. 42, pp. 1062 – 1064, Aug. 2006.

- [22] A. Lin and H. Ling, "A Doppler and direction-of-arrival (DDOA) radar for multiple-mover sensing based on a two-element array," *IEEE Trans. Aerosp. Elect. Syst.*, vol. 43, no. 4, pp. 1496 – 1509, Oct 2007.
- [23] D. G. Falconer, K. N. Steadman, and D. G. Watters, "Through-the-wall differential radar," *Proc. SPIE Sensors and Surveillance Technology*, vol. 2938, pp.147 – 151, 1997.
- [24] D.G. Falconer, R.W. Ficklin and K.G. Konolige, Robot-mounted through-wall radar for detecting, locating, and identifying building occupants, *Proc. IEEE Int. Conf. Robot. Automat.* no.2, pp. 1868–1875, 2000.
- [25] F. Ahmad, G. J. Frazer, S. A. Kassam and M. G. Amin, "Design and implementation of near field wideband synthetic aperture beamformer," *IEEE Trans. Aerosp. Elect. Syst.*, vol. 40, pp. 206 – 220, Jan. 2004.
- [26] A.M Attiya, A. M. Bayram, A. Safaai-Jazi and S. M. Raid, "UWB applications for through wall detection," *IEEE Antennas Propagat. Soc. Int. Symp. Digest*, vol. 3, pp. 3079 – 3082, June 2004.
- [27] Y. Yang and A. E. Fathy, "See-through-wall imaging using ultra-wideband short-pulse radar system," *IEEE Antennas Propagat. Soc. Int. Symp. Digest*, vol. 3B, pp. 334 – 337, July 2005.
- [28] F. Ahmad and M. G. Amin, "A noncoherent radar system approach for through-the-wall imaging," *IEEE Trans. Aerosp. Elect. Syst.*, vol. 42, pp. 1405 – 1419, Oct. 2006.
- [29] R. M. Narayanan, "Through-wall radar imaging using UWB noise waveforms," *Journal of Franklin Institute, Special Issue on Indoor Imaging*, vol. 345, no. 6, pp. 659 – 678, September 2008.
- [30] M. Dehmollaian and K. Sarabandi, "Refocusing through building walls using synthetic aperture radar," *IEEE Trans. Geoscience and Remote Sensing*, vol. 46, no.6, pp. 1589 – 1599, June 2008.
- [31] J. L. Geisheimer, E. F. Greneker and W. S. Marshall, "High-resolution Doppler model of the human gait," *SPIE Proc. Radar Sensor Tech. Data Vis.*, vol. 4744, pp. 8 – 18, July 2002.
- [32] V. C. Chen and H. Ling, *Time Frequency Transforms for Radar Imaging and Signal Analysis*, Artech House, Boston, MA, 2002.

- [33] P. van Dorp and F. C. A. Groen, "Human walking estimation with radar," *IEE Proc. Radar Sonar Navigation*, vol. 150, pp. 356 – 365, Oct. 2003.
- [34] V. C. Chen, F. Li, S. S. Ho and H. Wechsler, "Analysis of micro-Doppler signatures," *IEE Proc. Radar, Sonar, Navigat.*, vol. 150, no. 6, pp. 271-276, Aug. 2003.
- [35] T. Thayaparan, S. Abrol, E. Riseborough, L. Stankovic, D. Lamothe, and G. Duff, "Analysis of radar micro-Doppler signatures from experimental helicopter and human data," *IET Radar, Sonar & Navigation*, vol. 1, no. 4, pp. 289 – 299, Aug. 2007.
- [36] M. Otero, "Application of continuous wave radar for human gait recognition," *SPIE Proc., Signal Processing, Sensor Fusion, and Target Recognition XIV*, vol. 5809, pp. 538 – 548, May 2005.
- [37] I. Bilik, J. Tabrikian and A. Cohen, "GMM-based target classification for ground surveillance Doppler radar," *IEEE Trans. Aerosp Elect. Syst.*, vol. 42, no. 1, pp. 267 – 278, Jan 2006.
- [38] M. D. Anderson and R. L. Rogers, "Micro-Doppler analysis of multiple frequency continuous wave radar signatures," *SPIE Proc., Radar Sensor Technology XI*, Volume 6547, pp. 65470A, May 2007.
- [39] Y. Kim and H. Ling, "Human activity classification based on micro-Doppler signatures using support vector machine," accepted for publication in *IEEE Trans. Geosci. Remote Sensing.*, special issue on Indoor Imaging.
- [40] R. Boulic, M. N. Thalmann and D. Thalmann, "A global human walking model with real-time kinematic personification," *Vis. Comput.*, vol. 6, pp. 344 – 358, 1990.
- [41] T. Dogaru and L. Nguyen, "FDTD models of electromagnetic scattering by the human body," *IEEE Antennas Propagat. Soc. Int. Symp. Digest*, pp. 1995 – 1998, July 2006.
- [42] T. Dogaru and C. Le, "Validation of Xpatch computer models for human body radar signature," ARL-TR-4403, March 2008.
- [43] C. Christianson, "Through-wall radar propagation study using finite difference time domain method" MS thesis, University of Texas at Austin, May 2008.

- [44] R. J. Burkholder, P. C. Chang, R. J. Marhefka and J. L. Volakis, "UTD ray tracing for building imaging studies," *IEEE Antennas Propagat. Soc. Int. Symp. Digest*, July 2008.
- [45] R. J. Burkholder, R. J. Marhefka and J. L. Volakis, "Radar imaging through cinder block walls and other periodic structures," *IEEE Antennas Propagat. Soc. Int. Symp. Digest*, July 2008.
- [46] P. B. Weichman, "Ultra-fast forward modeling of microwave propagation through multipathing media for efficient solution of tomographic inverse problems," *URSI National Radio Science Meeting Digest*, July 2007.
- [47] M. Dehmollaian and K. Sarabandi, "Hybrid FDTD and ray optics approximation for simulation of through-wall microwave imaging," *IEEE Antennas Propagat. Soc. Int. Symp.*, pp. 249 – 252, July 2006.
- [48] K. Kodera, C. de Villedary and R. Gendrin, "Analysis of time varying signals with small BT values," *IEEE Trans. Acoust. Speech Signal Proc.*, vol. 26, pp. 64-76, February 1978.
- [49] F. Auger and P. Flandrin, "Improving the readability of time frequency and time scale representations by the reassignment method," *IEEE Trans. Signal Proc.*, vol. 43, pp. 1068-1089, May 1995.
- [50] S. A. Fulop and K. Fitz, "Algorithms for computing the time-corrected instantaneous frequency (reassigned) spectrogram, with applications," *J. Acoust. Soc. Am.*, vol. 119, no. 1, pp. 360-371, January 2006.
- [51] T. J. Gardner and M. O. Magnasco, "Sparse time-frequency representations," *Proc. Natl. Acad. Sci.*, vol. 103, no. 16, pp. 6094-6099, April 2006.
- [52] B. Armstrong and B.S. Holeman, "Target tracking with a network of Doppler radars," *IEEE Trans. Aeros. Electronic Sys.*, vol. 34, pp.33 – 48, Jan 1998.
- [53] Y. Kim and H. Ling, "Through-wall human tracking with multiple Doppler sensors using an artificial neural network" accepted for publication in *IEEE Transactions on Antennas and Propagation*, June 2008.
- [54] J. Tsao and B. D. Steinberg, "Reduction of sidelobe and speckle artifacts in microwave engineering: the CLEAN technique," *IEEE Trans. Antennas Propagat.*, vol. 36, pp 543 – 556, Apr. 1988.

- [55] J. Li and P. Stoica, "Efficient mixed-spectrum estimation with applications to target feature extraction," *IEEE Trans. Signal Processing*, vol. 44, pp 281-295, February 1996.
- [56] James Avro, *Graphic Gems II*, Academic Press Inc, Ithaca, New York, 1991.
- [57] J. W. Crispin, Jr. and A. L. Maffett, "Radar cross-section estimation for simple shapes," *Proc. of the IEEE*, pp. 833 – 848, Aug 1965.
- [58] C.A.Balanis, *Advanced Engineering Electromagnetics*, John Wiley & Sons Inc, NJ, 1989.
- [59] C. Gabriel, S. Gabriel and E. Corthout, "The dielectric properties of biological tissues. I. Literature Survey," *Phys. Med. Biol.*, vol. 41, pp. 2231 – 2249, 1996.
- [60] K. Shoemake, "Animating rotations with quaternion curves," *Int. Conf. Comp. Graphics and Interactive Techniques*, vol. 19, pp. 245-254, Nov. 1995.
- [61] E. F. Knott, J. F. Shaeffer and M. T. Tuley, *Radar Cross Section*, 2nd ed., Scitech Publishing Inc, NC, 2004.
- [62] P. van Dorp and F. C. A. Groen, "Feature-based human motion parameter estimation with radar," *IET Radar, Sonar & Navigation*, vol. 2, no. 2, pp. 135 – 145, April 2008.
- [63] G. Welch and G. Bishop, "An introduction to the Kalman filter," UNC Chapel Hill, TR 95-041, April 2004.
- [64] A. Lin and H. Ling, "Frontal imaging of humans using three element Doppler and direction of arrival radar," *Elect. Lett.*, vol. 42, no. 11, pp. 660 – 661, May 2006.

Vita

Shobha Sundar Ram was born in Chennai, India in December 1982. In April 2004, she was awarded Bachelor of Engineering, in electrical and communication engineering from the University of Madras, Tamil Nadu, India. She enrolled in graduate school in the University of Texas at Austin in August 2004 and received her Master of Science in electrical and computer engineering in May 2006. She served as a teaching assistant in the Dept of Electrical and Computer Engineering and the Dept. of General Engineering from September 2004 to May 2007. During summers 2005 and 2006 and from May 2007 onwards she has served as a research assistant under Professor Hao Ling in the Dept. of Electrical and Computer Engineering. She is a recipient of the University Continuing Fellowship for the academic year Fall 2008 to Spring 2009.

Permanent address: Old. no. 16, New. no. 10, Prithivi Avenue, Abhiramapuram,
Chennai 600 018, Tamil Nadu, India.

This dissertation was typed by the author.